Doctorate Dissertation
博士論文

Angle-resolved photoemission spectroscopy studies of electronic structure and its relationship to transport properties of iron-based superconductors
(角度分解光電子分光による鉄系超伝導体の電子状態と輸送特性の関連の研究)

A Dissertation Submitted for Degree of Doctor of Philosophy
December 2018
平成 30 年 12 月博士（理学）申請

Department of Physics, Graduate School of Science,
The University of Tokyo
東京大学大学院理学系研究科物理学専攻

Keisuke Koshiishi
輿石　佳佑

Abstract

Since superconductivity in Fe-based compounds was discovered in 2008, many efforts have been made to understand the mechanism of the unconventional superconductivity. Iron-based superconductors (FeSCs) are mainly classified into six categories according to their structures. One of them is the “122”-type FeSCs, which have been studied most extensively. In addition, ”11”-type FeSCs are also one of the most extensively studied FeSCs because of their simple crystal structures and the absence of antiferromagnetic order. So far, in these compounds, these phenomena have been found and to investigate their origins and the relationship between the non-trivial phenomena and superconductivity is one of the main issues in order to understand the mechanism of the unconventional superconductivity in FeSCs. In the present thesis, we have studied the electronic structures of both classes of FeSCs, the ”122”- and ”11”-type FeSCs, by photoemission spectroscopy in order to clarify their electronic states and relationship to the non-trivial transport properties.

Photoemission spectroscopy is the most powerful technique, which allows us to directly investigate the electron states in the strongly correlated materials. In this thesis, we have investigated the electronic structures of FeSCs by angle-resolved photoemission spectroscopy (ARPES), resonant photoemission spectroscopy (RPES), and X-ray photoemission spectroscopy (XPS).

It is known that Cr substitution in the 122-type $BaFe_2As_2$ does not induce superconductivity in spite of the fact that, according to the rigid-band model, the Cr substitution corresponds to hole doping as in the case of Mn doping, in contrast to K doping. Its electronic structure has not been studied and the origin of the absence of the superconductivity is still unclear. Furthermore, the Cr-doped Ba122 shows sign change of the in-plane resistivity anisotropy with Cr content. The mechanism of the non-trivial sign change of the in-plane resistivity anisotropy is also uncertain.

In Chapter 3, $Ba(Fe_{0.81}Cr_{0.19})_2As_2$ has been studied by RPES in order to investigate the electronic structure of Cr 3*d* electrons. Since RPES is as element-specific measurement, RPES is very useful to investigate the doped Cr 3*d* states. The Fermi edge has been observed in the Cr 3*d* PDOS and the Cr 3*d* electrons has itinerant features. Therefore, $Ba(Fe_{0.81}Cr_{0.19})_2As_2$ is considered to be an effectively hole-doped system. However, the Cr 3*d* PDOS is mainly located at $\sim$1 eV below E_F, indicating the localization of the Cr 3*d* electrons. Then the high-spin state at the Cr site is realized by the on-site Coulomb interaction and Hund’s coupling. In Chapter 4, we have studied the electronic structure of $Ba(Fe_{1-x}Cr_x)_2As_2$ with varied Cr concentration (x= 0.06, 0.09, and x=0.19) by ARPES in order to investigate the Fe 3*d* band affected by the Cr substitution and its relationship to the sign change of the

in-plane resistivity anisotropy. Upon Cr substitution, Fermi level moves downward exhibiting upward band dispersion shift without significant changes of dispersion, indicating sufficient hole doping with the Cr substitution. Moreover, the Fermi surface topology changes from that of the parent compound. We concluded that the changes of the Fermi surface topology play an important role in the sign reversal of the in-plane resistivity anisotropy.

For "11"-type FeSCs, $FeTe_{1-x}Se_x$ have been studied. It is well established that as-grown $FeTe_{1-x}Se_x$ does not exhibit superconductivity due to interstitial Fe atoms. After annealing, the excess Fe atoms are removed and the superconductivity recovers. Interestingly, depending on the Se content, annealed samples show dramatically different temperature dependence of the Hall coefficient. Especially, in this study, the samples were annealed in Te vaper in order to remove the excess Fe atoms completely.

In chapter 5, we have studied the doping-evolution of the electronic structure in Te-annealed $FeTe_{1-x}Se_x$ (x=0.15, 0.2, 0.3, and 0.4) at low temperature by ARPES in order to clarify the electronic states of $FeTe_{1-x}Se_x$, in which the excess Fe atoms are completely removed. Upon increasing Se content, the γ band shifts downward and induces disappearance of the outer large hole pockets around the Γ point. We concluded that the changes of the Fermi topology and mass renormalization play an important role in the sign reversal of the Hall coefficient. In chapter 6, the temperature dependence of the electronic states of Te-annealed $FeTe_{1-x}Se_x$ (x=0.2 and 0.4) has been studied by ARPES in order to investigate the relationship between the electronic structure and the non-trivial magneto-transport properties. Upon increasing temperature, the coherent peak of the electron band around the zone corner weakens and disappears above 100 K in the optimally-doped compound in contrast to the temperature independent behavior of it for Se-underdoped compound, indicating the disappearance of the electron pockets. Moreover, the possible changes of the Fermi surface topology predicted from present results can explain the temperature dependence of the Hall coefficient.

Contents

Chapter 1

Introduction

1.1 general aspect of iron-based superconductors

Since superconductivity in fluorine-doped LaFeAsO with a high superconducting transition temperature (T_c) of 26 K was discovered by Hosono's group in 2008 [1], many studies have been performed in order to investigate iron-based superconductors (FeSCs) accounted unconventional superconductors as with the cuprate high-temperature superconductors. On the heels of the discovery of the superconductor LaFeAs($O_{1-x}F_x$), T_c reached 55 K in SmFeAs($O_{1-x}F_x$) [2], the highest T_c in FeSCs even now.

1.1.1 Crystal structure of the iron-based superconductors

Typical crystal structure of FeSCs is shown in Fig. 1.1. FeSCs all have layered structure where common layers composed of a square lattice of Fe atoms tetrahedrally coordinated by pnictogen (Pn = P, As) or chalcogen (Ch = S, Se, Te) atoms are separated by alkali, alkaline-earth, or rare-earth plus oxygen/fluorine 'block layers'. The Fe-pnictides or chalcogenides layer is widely believed to be the stage of the superconductivity as well as the Cu-O layer in the high T_c cuprates. Although the family of Fe-based superconductors is quite large, it can be classified into a total of six categories according to the block layer [8]. The first type of Fe-based superconductors is the "1111" compounds such as LaFeAsO, which is made up of the assortment of elements: rare-earth (La, Sm, Gd, etc.), transition metal (Fe, Co, Ni, etc.), pnictogen (As, P), and oxygen. The second type, the "122" compounds, is the most studied and the largest number of superconductors may belong to this category. These materials are made up of the combination of alkaline earth (Ba, K, Ca, Sr, etc.), transition metal (Fe, Co, Ni, etc.), and pnictogen (As, P), namely, AFe_2As_2 (A = Ba, K, Sr, Ca). They have the same structure as that of $CeCu_2Si_2$, which was discovered as the first heavy fermion superconductor [9]. The "111"-

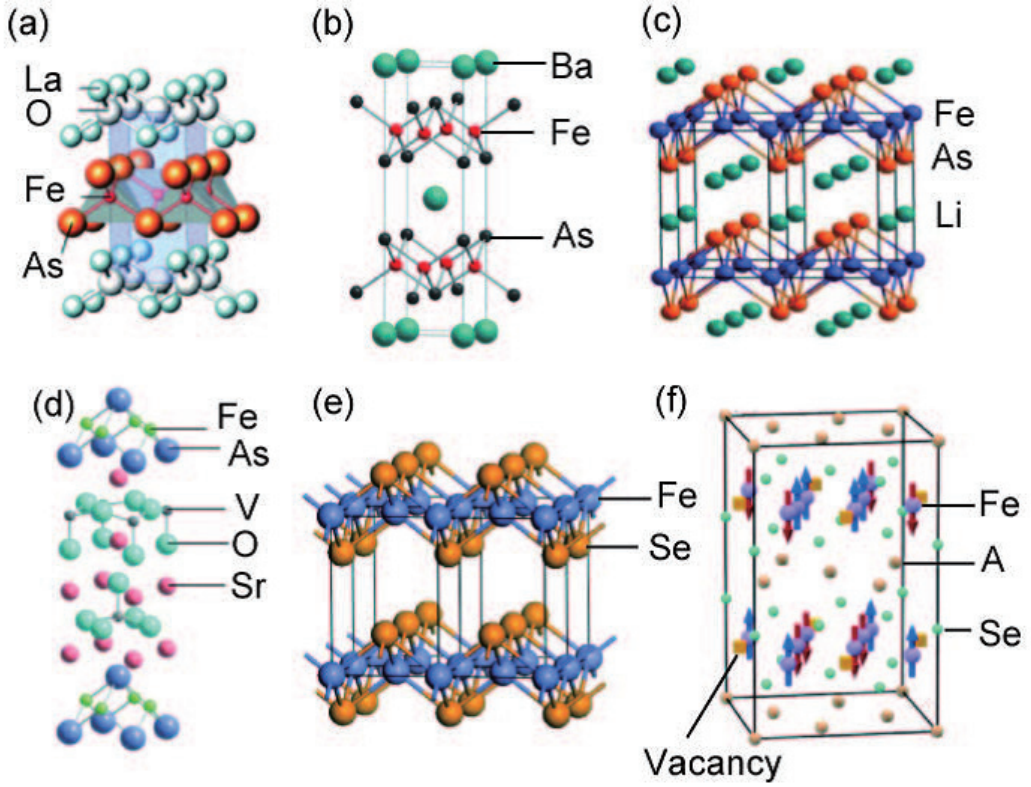

Figure 1.1: Crystal structures of six typical classes in iron-based superconductors know to support superconductivity. (a) LaOFeAs ("1111" family). (b) $BaFe_2As_2$ ("122" family). (c) LiFeAs ("111" family). (d) $Sr_4V_2O_6Fe_2As_2$. (e) FeSe ("11" family). (f) $A_2Fe_4As_5$ ("245" family). Reprinted from Ref. [1, 3–7]

type iron-based superconductors have a Cu_2Sb-type structure and a Li or Na layer and iron pnictide are stacked alternately. Sr_2MO_3FePn (M = Sc, V, Cr) are called the "21311" or "42622" compounds in which $Sr_3Fe_2Pn_2$ layers alternate with a layers of perovskite $Sr_3M_2O_6$. One of the family of the Fe-chalcogenide is the "11" compounds such as FeSe. They consist of just FeSe layers. Intercalating FeSe with K, Rb, Cs, Tl or combinations of them, the "245" family written as $A_{0.8}Fe_{1.6}Se_2$ or $A_xFe_{2-y}Se_2$ are obtained. They contain the ordered Fe vacancies and the arrangement of the vacancies below structural transition temperature may have significant effects on the physical properties [7]. The relationship between the crystal structure and T_c of FeSCs has been studied in order to understand the superconductivity of FeSCs, particularly the relationship between the As−Fe−As bond angle and to the T_c. Figure 1.2 shows the relation between the As-Fe-As angle and T_c. When the angle is close to that of regular tetrahedron $\sim 109.47^\circ$, T_c approaches the maximum.

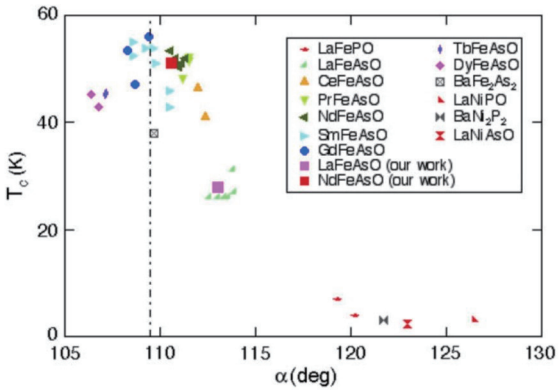

Figure 1.2: Relationship between the As-Fe-As bond angle α and T_c. T_c reaches at the bond angle of $\sim$ 110 degree Reprinted from Ref. [10]

In this study, superconductors which have the 122-type and 11-type crystal structures are studied. As mentioned above, the 122-type parent compounds $BaFe_2As_2$ and $BaCr_2As_2$ have the $ThCr_2Si_2$ type crystal structure with space group $I4/mmm$ [11, 12], and the 11-type FeSe and FeTe have the α-PbO type crystal structure with space group $P4/nmm$ [13, 14]. Especially, $BaFe_2As_2$ and FeSe undergo tetragonal-to-orthorhombic structural transition (from space group $I4/mmm$, $P4/nmm$ to $Fmmm$, $Cmma$ respectively) [11, 13]. Generally, in the orthorhombic state, materials form structural twins. So far, it has been reported that applying uniaxial stress (either compressive or tensile) along the principal axis prevents samples from forming twins.

It is well established that as-grown 11-type compounds can contain excess Fe atoms at interstitial site. Moreover, it has been reported that the structural properties of $Fe_{1+y}Te$ are affected by stoichiometric variations. Compounds with y=0.141 and 0.076 crystalize at low temperature with the orthorhombic (space group $Pmmn$) and monoclinic ($P2/_1m$) crystal structures while they are always the orthorhombic ($P4/nmm$) at high temperature [14,15]. Generally, the structural transition observed in the parent compounds are suppressed with atomic substitution, as explained in section 1.1.3.

1.1.2 Magnetic property of the iron-based superconductors

Another feature shared by all the FeSCs families is long-range magnetic order in the parent compounds. The parent compounds of FeSCs undergo a stripe-type antiferromagnitic (AFM) ordering, the so-called spin-density wave (SDW) in the temperature range from 130 to 160 K, accompanied by a structural transition from

the tetragonal to the orthorhombic/monoclinic ones. Especially, the structural transition temperature T_S of the parent compounds of the "122" [16] and "11" [17] family is identical or close to the magnetic transition temperature T_N of them. However, different compounds exhibit different AFM spin ordering.

The 122-type $BaFe_2As_2$ shows a collinear stripe-type AFM ordering [11] which has a wave vector directed along (π, π) defined in the tetragonal unit cell (the *a*- and *b*- axes are along the Fe-As direction): The spin of the Fe atom is directed to the nearest-neighbor Fe atom and shows AFM ordering along that direction while it has ferromagnetically aligned perpendicular to the spin direction. In addition, the distance between Fe atoms along the spin direction is longer than that along the perpendicular direction, leading to the orthorhombic distortion as shown in Fig. 1.3.

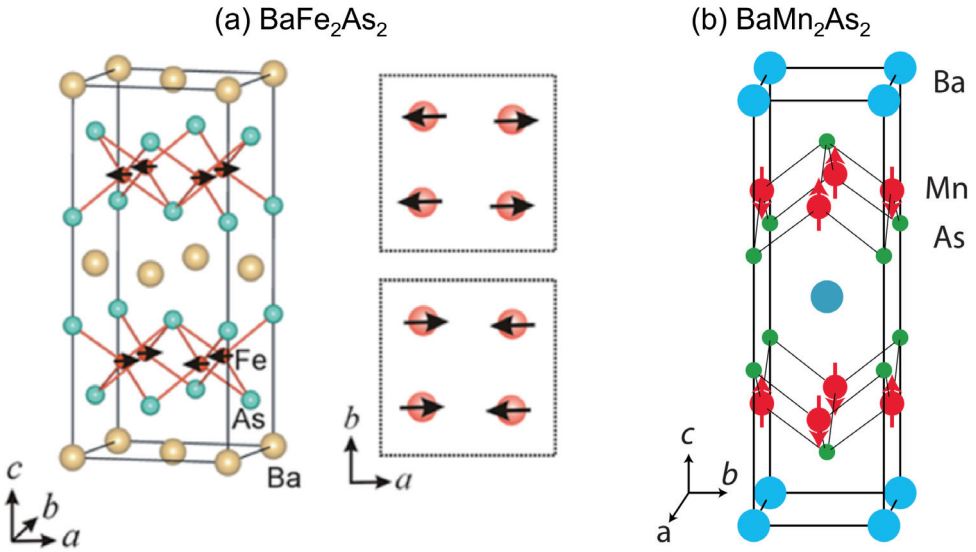

Figure 1.3: Magnetic structure of the 122-type family. (a) Stripe-type AFM order of $BaFe_2As_2$. (b) G-type AFM order of $BaMn_2As_2$. Reprinted from Ref. [11, 18]

In the hole-doped $Ba(Fe_{1-x}M_x)_2As_2$ (M=Mn or Cr), they have the checkerboard-type (G-type) AFM ordering at low temperature instead of the stripe-type AFM. The spin at the Fe site lies in the a-b plane and the nearest-neighbor spins are aligned antiparallel. Similar AFM ordering has been discovered in $EuCr_2As_2$.

In the case of the 11-type FeTe, it exhibits a bi-collinear double-stripe AFM order with the wave vector Q=(π , 0) as shown in Fig. 1.4 (b) [15]. The spin is aligned ferromagnetically along the diagonal direction of the Fe square lattice while it has ferromagnetically aligned perpendicular to the spin direction, which is distinct from the stripe-type AFM of the "122" system shown in Fig. 1.4 (c). In addition, Bao *et al* found an incommensurate AF order for $Fe_{1.141}Te$ at low temperature with

orthorhombic lattice distortion by neutron diffraction as shown in Fig. 1.4 (d) [14]. The incommensurability decreases with decreasing excess Fe and a commensurate AFM was observed for $Fe_{1.076}Te$.

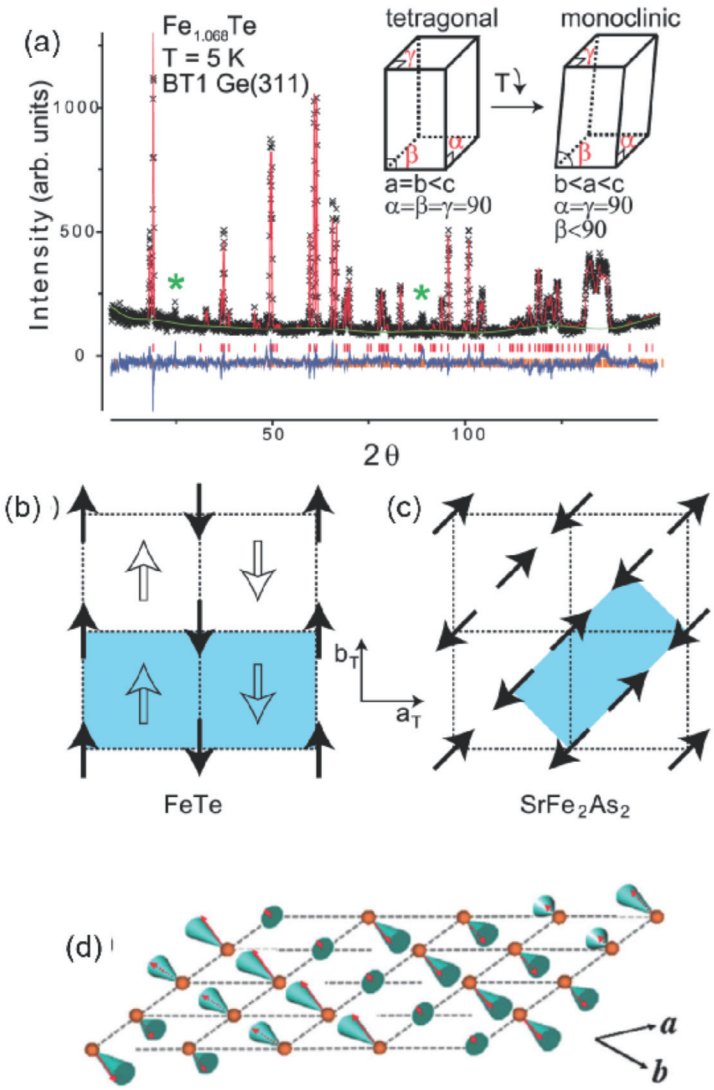

Figure 1.4: Structural and magnetic properties of the 11-type FeTe. (a) Neutron powder-diffraction data of $Fe_{1.068}Te$ and schematic picture of structural transition. (b) In-plane magnetic structure of FeTe. (c) In-plane magnetic structure of the 122-type $SrFe_2As_2$ (d) Magnetic structure of incommensurate AFM in FeTe. Reprinted from Ref. [14, 15]

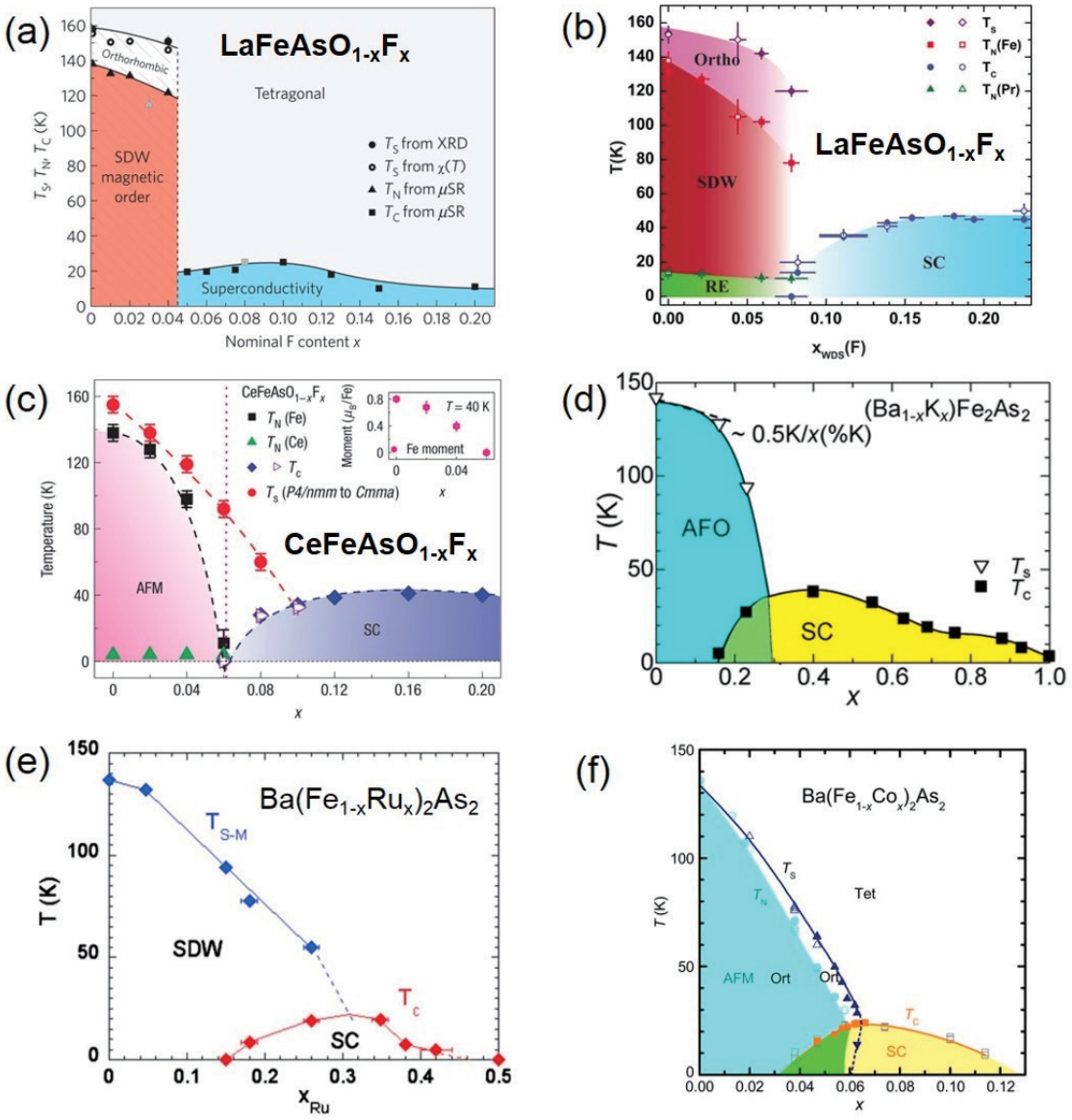

Figure 1.5: The phase diagrams of the iron-based superconductors. (1) F substitution for O in $LaFeAsO_{1-x}F_x$. (2) F substitution for O in $PrFeAsO_{1-x}F_x$. (3) F substitution for O in $CeFeAsO_{1-x}F_x$. (4) K substitution for Ba in $(Ba_{1-x}K_x)Fe_2As_2$. (5) Ru substitution for Fe in $Ba(F_{1-x}Ru_x)_2As_2$. (6) Co substitution for Fe in $Ba(F_{1-x}Co_x)_2As_2$. Reprinted from Ref. [19–24]

1.1.3 Phase diagram

To understand the overall tendency of the physical properties of the superconductors, the phase diagram, of which the abscissa and the ordinate indicate the amount of doped holes or electrons and the temperature, respectively, is often used. The phase diagrams of the "122" and "1111" families of FeSCs are presented in Fig. 1.5, which are similar to those of other unconventional superconductors, namely, the cuprates and heavy-fermion superconductors. As the phase diagrams suggest, doping holes or electrons into the parent compounds by chemical substitution or applying pressure by isovalent replacement of pnictogen element can induce superconductivity. As doping level increases, the antiferromagnetism is suppressed as the quantity of the doped element increases and the superconducting dome appears in close proximity to the SDW phase. Note that T_S becomes separated from T_N upon doping with the structural transition preceding the magnetic transition except for some compounds such as K-doped $BaFe_2As_2$. The phase transition from the anitiferromagnetic phase to the superconducting phase upon doping is a general property of most of FeSCs.

On the other hand, the phase diagram of the 11 system differs from that of the 122-type FeSCs. Figure 1.6 shows the phase diagram of $Fe_{1+y}Te_{1-x}Se_x$. As mentioned above, the parent compound FeTe exhibit AFM order. In the region near FeTe, its phase diagram is similar to that of other FeSCs. Namely, with increasing doping level, the AFM order is suppressed and superconductivity emerges. However, the parent compound on the other side FeSe also shows superconductivity in contrast to the 122-type family.

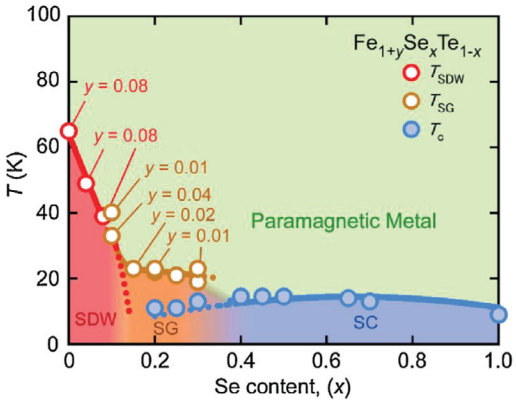

Figure 1.6: The phase diagrams of $Fe_{1+y}Te_{1-x}Se_x$. Reprinted from Ref. [25]

1.1.4 Transport properties

The iron-based superconductors are similar to the cuprate hight-T_c superconductors in terms of the crystal structure and the phase diagram. However, the parent compounds of the cuprate high-T_c superconductors are Mott insulators with charge-transfer gaps while the parent compounds of FeSCs such as LaFeAsO are antiferromagnetic metals. As for the superconducting samples, the magnitude of the resistivity at room temperature is several hundred $\mu\Omega$ cm in the Fe-based superconductors while it is several dozens $\mu\Omega$ cm in the cuprates. Figure 1.7 shows the temperature dependence of the in-plane resistivity of the superconductors. In FeSCs, anomaly due to the AFM transition appears in the resistivity around T_N, below which the resistivity drops.

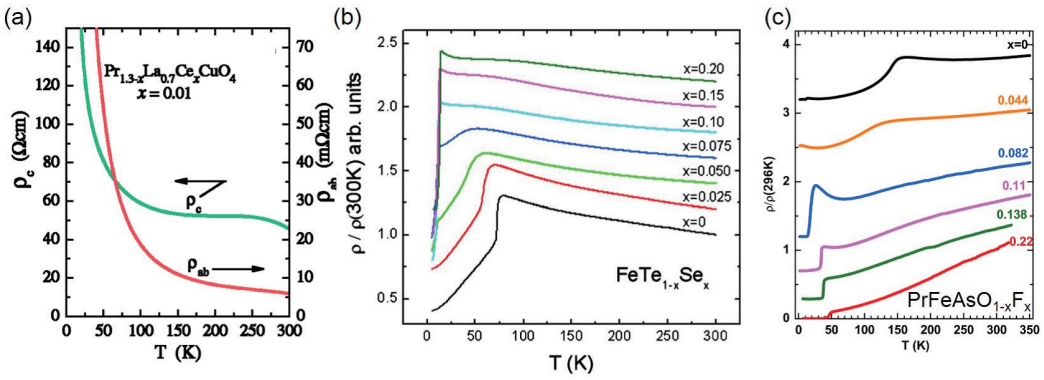

Figure 1.7: Temperature dependence of the resistivity in several parent and underdoped compounds of superconductors. (a) $Pr_{1.3-x}La_{0.7}Ce_xCuO_4$ ($x = 0.01$). (b) $FeTe_{1-x}Se_x$ ($x = 0, 0.025, 0.05, 0.075, 0.1, 0.15, 0.2$). (c) $PrFeAsO_{1-x}F_x$ ($x = 0, 0.044, 0.082, 0.11, 0.138, 0.22$). Reprinted from Ref. [17, 20, 26], respectively.

1.1.5 Electronic states of the iron-based superconductors

Generally, in the iron-base superconductors, the valence bands consist of Fe 3*d* electrons. Especially, for a transition metal coordinated by pnictogen or chalcogen tetrahedrally, it is expected that the five 3*d* orbitals split into low energy states of two e_g orbitals and high energy states of three t_{2g} orbitals. However, the band formed from these five 3*d* orbitals overlap near the Fermi level and the splitting is not clear. In addition,the pnictogen or chalcogen *p* orbitals do not contribute much. Namely, direct hopping of electrons from Fe site to Fe site contribute to metallic conduction dominantly. Since the iron-based superconductors are basically two-dimensional compounds, they exhibit cylindrical Fermi surfaces.

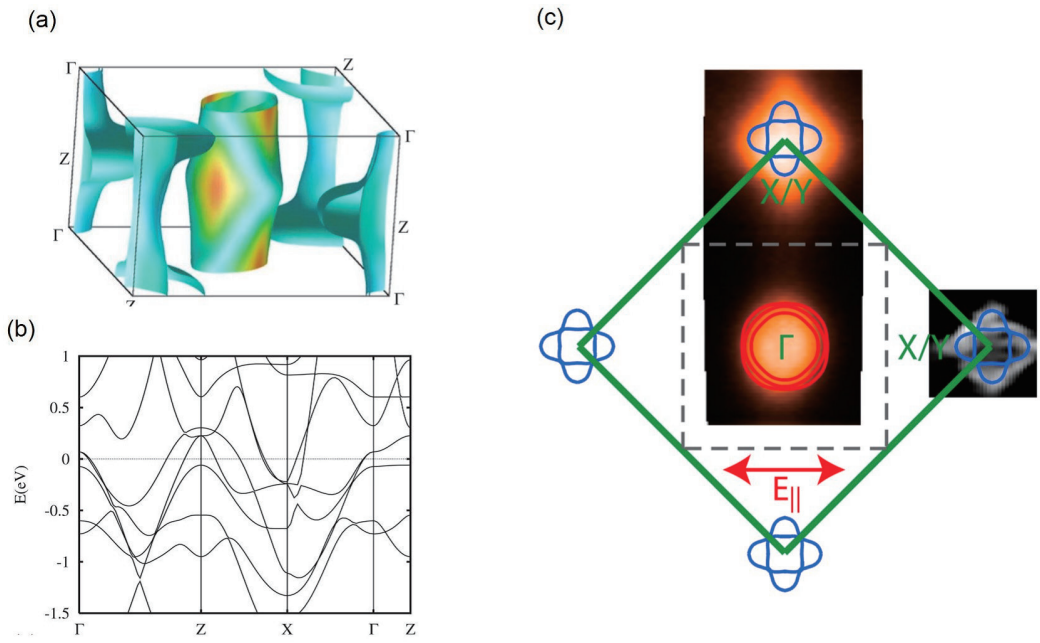

Figure 1.8: Band structure and Fermi surfaces of $BaFe_2As_2$ in the paramagnetic-tetragonal state. (a) The 3D Fermi surface of $BaFe_2As_2$ shaded by band velocity. (b) The band structure $BaFe_2As_2$ near E_F. (c) The Fermi surface of $BaFe_2As_2$ determined experimentally by ARPES. Reprinted from Ref. [27, 28]

1.1.5.1 ”122” family

In the paramagnetic (PM)-tetragonal state, $BaFe_2As_2$ seems to have five sheets of Fermi surface (FS): There are two electron cylinders at the corners of the Brillouin zone (BZ) and three hole sheets at the center of the BZ. Calculated FSs and the band structure are shown in Fig. 1.8 and consistent with experimental results [33]. In the antiferromagnetic-orthorhombic state below T_S, a stripe-type SDW ordering becomes stable and the folded band structure due to the SDW order has been observed by angle-resolved photoemission spectroscopy (ARPES) study [31] as shown in Fig. 1.9.

1.1.5.2 ”11” family

Typical calculated band structure of the ”11” systems is shown in Fig. 1.10 (a). Similar to the paramagnetic-tetragonal state of the ”122” systems, there are three hole bands around the Γ point and two electron bands around the M point. Some of them form Fermi surfaces as shown in Fig. 1.10 (b); hole pockets around Γ and electron pockets around M. In Fig. 1.10 (c), as mentioned above, Se $4p$ or-

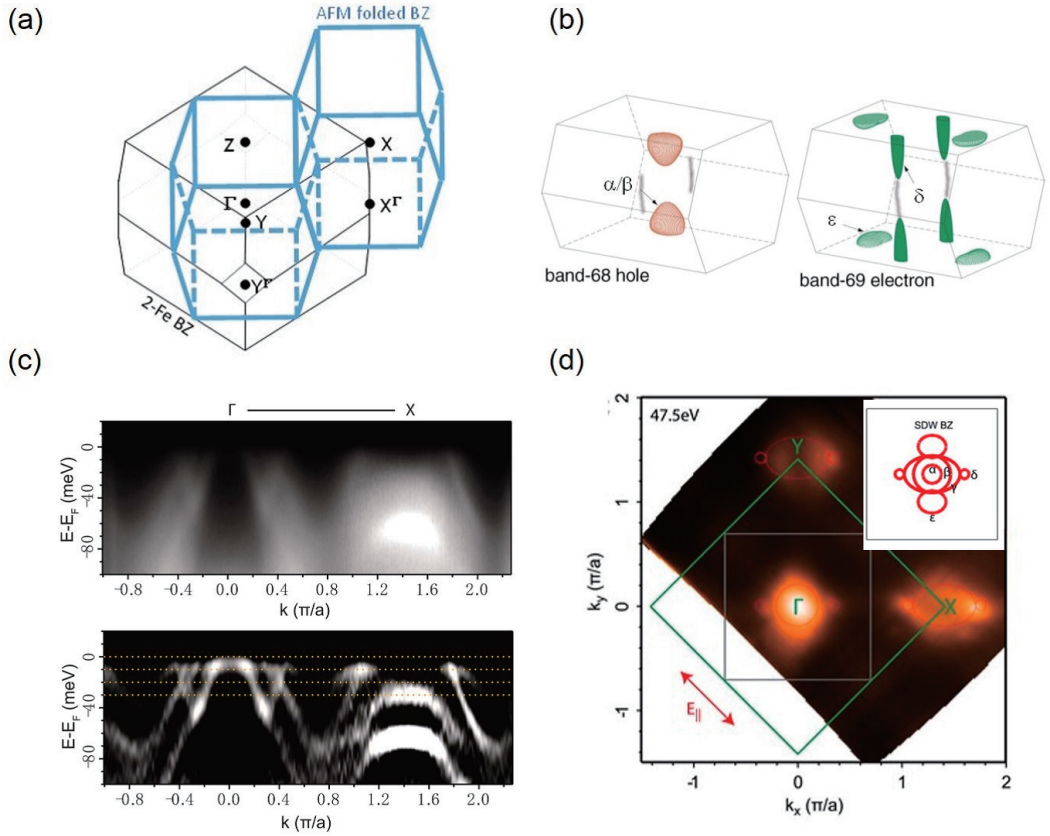

Figure 1.9: Electronic structure of $BaFe_2As_2$ in the antiferromagnetic (AFM)- orthorhombic state. (a) 3D Brillouin zone (BZ) of the bct structure for $BaFe_2As_2$ in the PM state (black lines) and folded BZ in the AFM state (blue lines). Reprinted from Ref. [29] (b) Fermi surfaces (FS) in the AFM phase determined by Shubnikov-de Haas (ShdH) oscillations. There are two hole surfaces α/β and two electron pockets δ, ε. Reprinted from Ref. [30] (c) Band structure of $BaFe_2As_2$ determined experimentally by ARPES. Upper panel shows raw ARPES spectra of $BaFe_2As_2$ and lower panel is the second derivative image of the spectra. Reprinted from Ref. [31] (d) FS mapping with 25 eV photons. Reprinted from Ref. [28]

bitals does not have intensity at E_F, indicating non-contribution of Se $4p$ electrons. In some of the FeSe-derived superconductors [34–36], Fermi surface topology distinct from that of the bulk FeSe have been observed. In most cases, the obvious electron pockets persist around the M point but hole-like band dispersion around Γ are located well below the Fermi level and then the hole Fermi surfaces are missing, suggesting that extra electron carriers are somehow provided into the system.

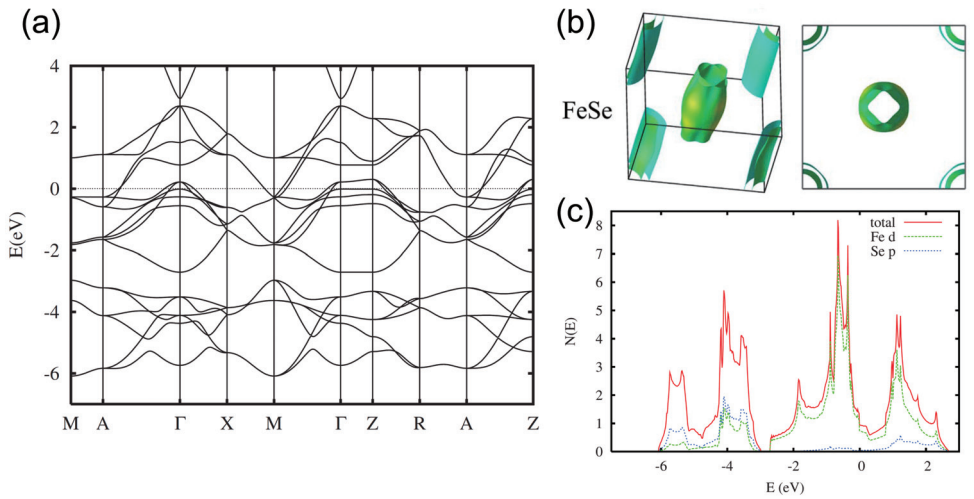

Figure 1.10: The calculated electronic states of the 11-type FeSe in the tetragonal state. (a) Calculated band structure. (b) Fermi surfaces. (c) Density of states. Reprinted from Ref. [32]

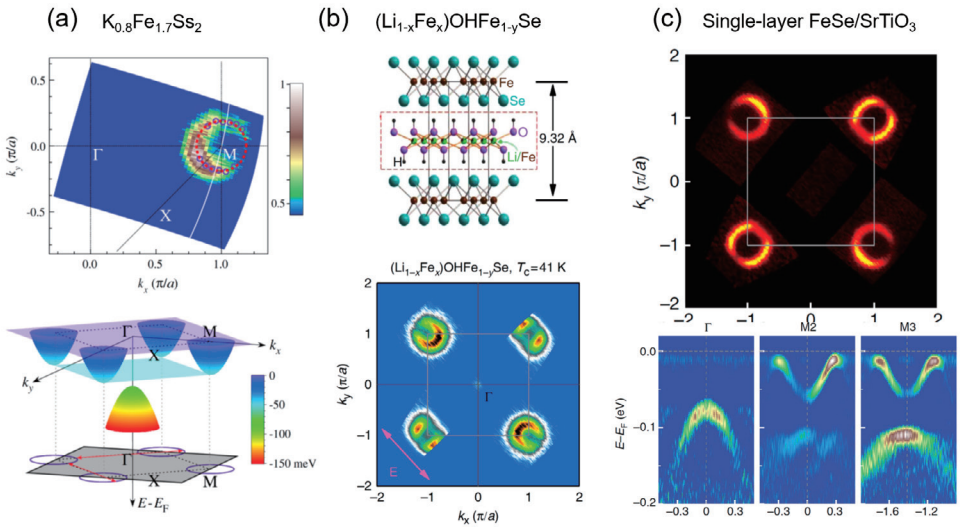

Figure 1.11: Fermi surfaces of the FeSe-derived superconductors. (a) The Fermi surfaces and schematic 3-dimensional band dispersion of $K_{0.8}Fe_{1.7}Se_2$ (b) The crystal structure and the Fermi surfaces of $(Li_{1-x}Fe_x)OHFe_{1-y}Se$. (c) The Fermi surfaces and band dispersions of single-layer $FeSe/SrTiO_3$. Reprinted from Ref. [34–36]

1.1.6 Nematicity

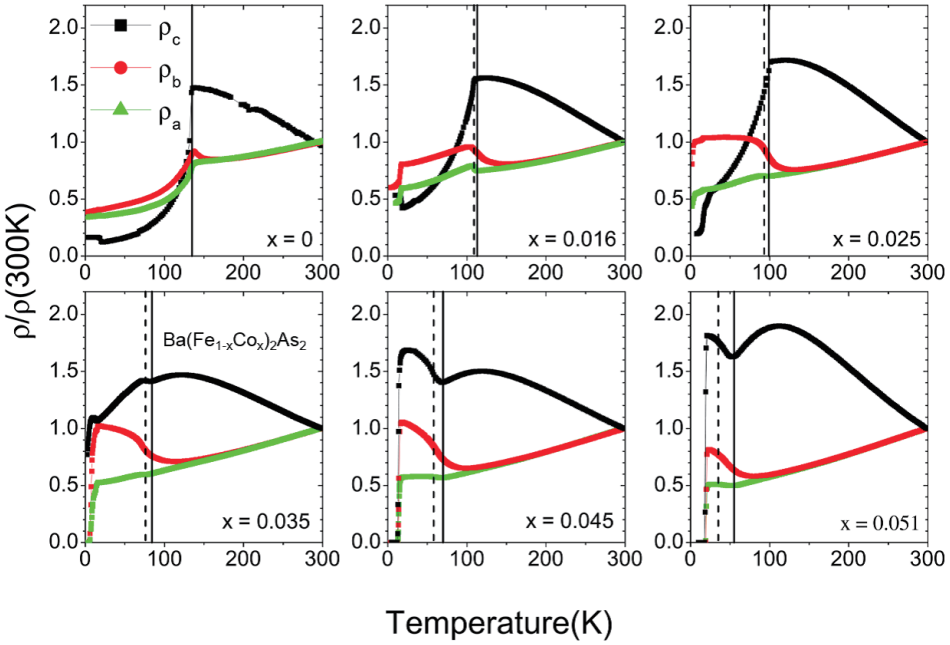

Figure 1.12: Temperature dependence of the in-plane resistivity along the a- and b-axes in $Ba(Fe_{1-x}Co_x)_2As_2$. Reprinted from Ref. [37]

As mentioned above, the FeSCs spontaneously breaks the four-fold rotational symmetry in the Fe-As plane with a change of the rotational point group symmetry of the lattice from tetragonal to orthorhombic at T_S whereas time-reversal symmetry is preserved. Since the T_S approaches the superconducting dome upon increasing the doping concentration, it is believed that understanding the origin of the order in the orthorhombic state is important. By analogy with the nematic phase of liquid crystals, the orthorhombic state is called nematic phase. In the nematic state, in-plane anisotropies have been observed in not only crystal structure but also other electronic properties such as d.c. resistivity and optical conductivity. The in-plane anisotropic resistivity of $Ba(Fe_{1-x}Co_x)_2As_2$ are shown in Fig. 1.12. The most important thing is that the resistivity along the a-axis is smaller than that along the b-axis although the a-axis is longer than the b-axis and the spin direction of Fe is antiferromagnetically arranged along the a-axis. That is , the observed anisotropy is counterintuitive to the expected larger orbitals overlap and weaker spin scattering along the b-axis than the a-axis. Moreover, the orthorhombic distortion defined as the ratio of the in-plane lattice constants $(a-b)/(a+b)$ has the maximum value of 0.36 for x=0 and monotonically decreases upon increasing x, while anisotropy of the in-plane resistivity expressed in terms of the resistivity ratio ρ_b/ρ_a is a non-

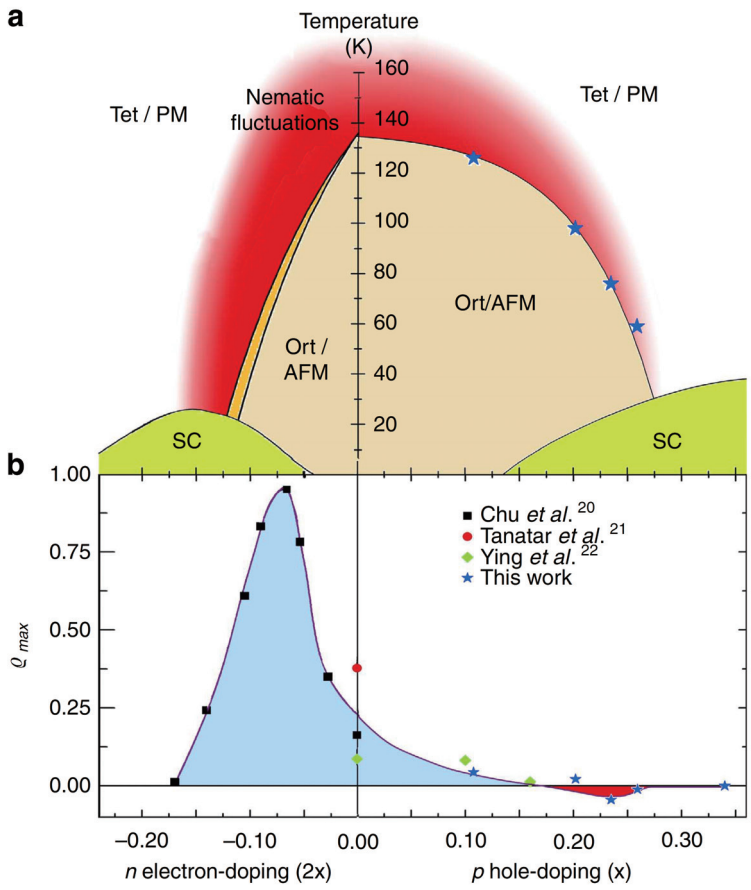

Figure 1.13: Doping phase diagram and resistivity anisotropy. (a) Phase diagram of the electron- and hole-doped Ba122 system. (b) The maximum in-plane resistivity anisotropy in strained samples. Reprinted from Ref. [38]

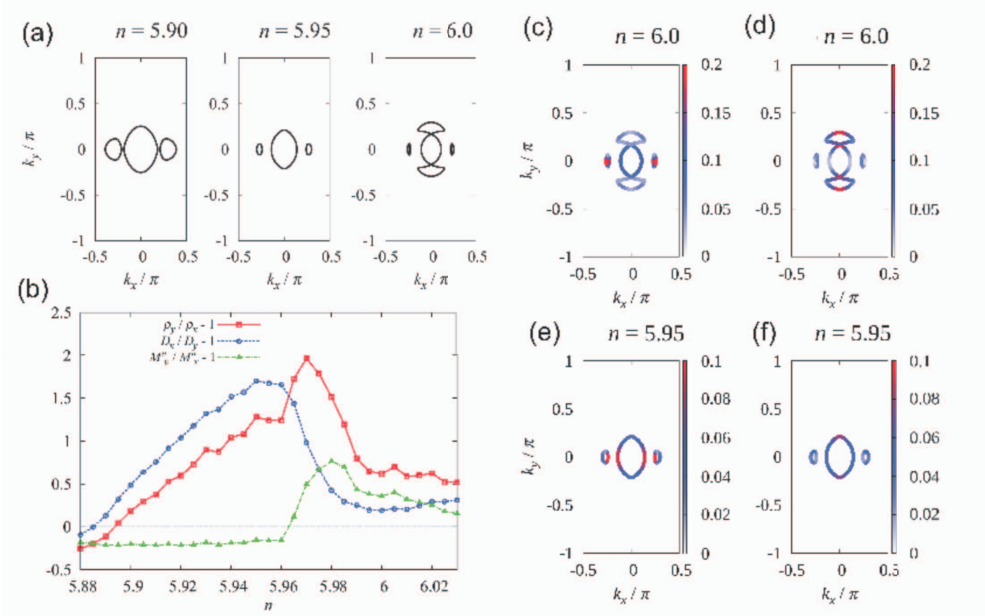

Figure 1.14: Theoretical doping dependence of the in-plane resistivity and the Fermi surface topology. (a) The Fermi surfaces at the electron density n=5.90, 5.95 and 6 in the stripe-type AFM state. The electron density of the parent compound is $n = 6$. (b) The electron density dependence of anisotropy of the resistivity, Drude weight and memory function describing the effect of impurity scattering. (c), (d) The intensity of the memory function on the Fermi surfaces corresponding to the scattering rate along the x- and y-axes with $n = 6$, respectively. (e), (f) The same as (c) and (d), respectively, but $n = 5.95$. Reprinted from Ref. [39]

monotonic function of doping, approaching a maximum near $x = 0.35$. Notably, the resistivity anisotropy persists well above T_S.

Two scenarios have mainly been proposed as the origin of the in-plane resistivity anisotropy. One is the anisotropy of impurity scattering. It has been reported that the post-annealing treatment results in the suppression of the anisotropy of the in-plane resistivity [22] and that the anisotropy decreases with increasing distance from the Fe atom to the substitution site. These results should be explained by the anisotropy of carrier scattering by substituted atoms. On the other hand, the fact that difference of resistivity $\rho_b \quad \rho_a$ in hole doped compound $Ba_{1-x}K_xFe_2As_2$ is smaller than that in electron-doped system $Ba(Fe_{1-x}Co_x)_2As_2$ and takes a negative value upon increasing K content indicate that anisotropic Fermi surface topology may plays an important role in the in-plane resistivity anisotropy [38] (Fig. 1.13). The sign reversal of the in-plane resistivity anisotropy in hole-doped systems have been predicted by theoretical calculations taking into account the Fermi surface

topology [40–42]. The scenario based on the Fermi surface topology, however, is not able to explain the post-annealing effects. In addition, theoretical calculations taking into account impurity scattering and Fermi surfaces topology have been carried out with using multi-orbital Hubbard model in the AFM phase [39]. As shown in Fig 1.14, according to the study, upon hole doping, the elliptical electron pockets along the *b*-axis vanish and the Dirac-cone-like pockets along the *a*-axis expand gradually. They have also attributed the sign change of the in-plane resistivity anisotropy in hole-doped iron-based superconductors to the interplay of impurity scattering and anisotropic electronic states strongly influenced by the topology of the Fermi surface. Scattering rate of the elliptical electron pockets due to impurity scattering dominates the total scattering rate along the *b*-axis, and disappearance of the elliptical electron pockets upon hole doping induces the sign change of the scattering rate anisotropy. However, the resistivity anisotropy is supposed not to change its sign because of opposite sign of the Drude weight anisotropy, which also change its sign at electron density $n \sim 5.88$. However, corresponding evolution of electronic state has not been observed. The question of what is a mainly dominant effect in the anisotropy of the in-plane resistivity observed in the nematic phase still remains under debate.

1.2 Hole-doped 122-type compound $Ba(Fe_{1-x}Cr_x)_2As_2$

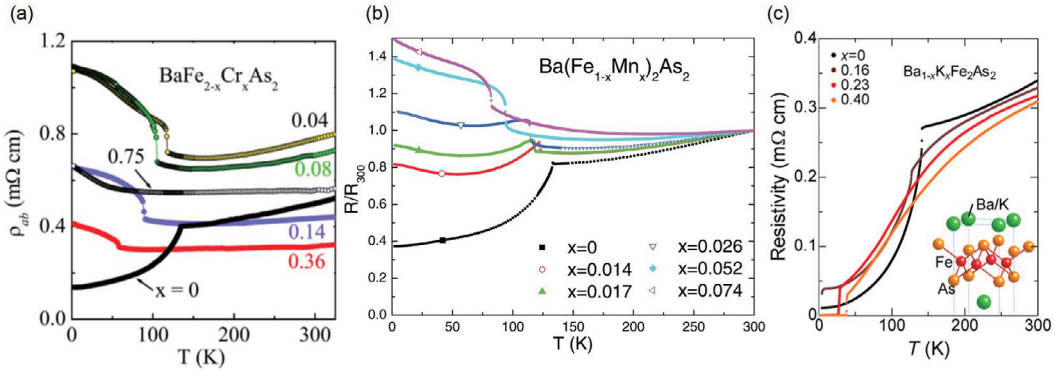

Figure 1.15: Temperature dependence of the resistivity of hole-doped $BaFe_2As_2$. (a) $Ba(Fe_{1-x}Cr_x)_2As_2$. (b) $Ba(Fe_{1-x}Mn_x)_2As_2$. (c) $Ba_{1-x}K_xFe_2As_2$. Reprinted from Ref. [18, 22, 43]

High-temperature superconductivity in the Fe-based superconductors is generally induced by carrier doping with chemical substitution. For $BaFe_2As_2$ (Ba122), electron doping realized by Ni, Co, or Cu substitution for Fe [48, 49] and hole doping realized by K substitution for Ba [50] have been successful in inducing super-

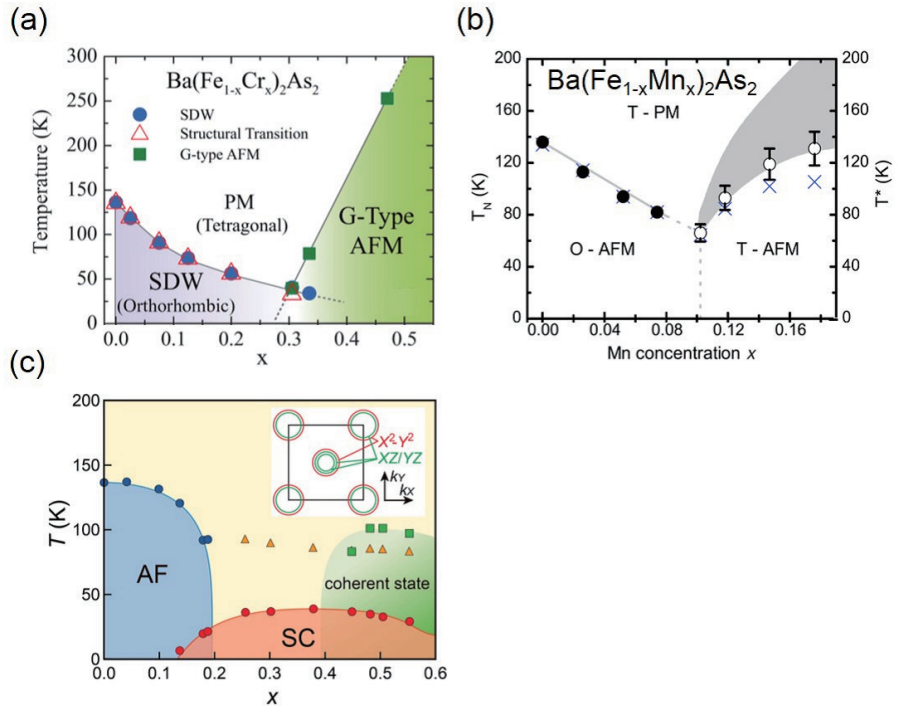

Figure 1.16: Phase diagram of hole-doped $BaFe_2As_2$. (a) $Ba(Fe_{1-x}Cr_x)_2As_2$. (b) $Ba(Fe_{1-x}Mn_x)_2As_2$. (c) $Ba_{1-x}K_xFe_2As_2$. Reprinted from Ref. [44–46]

conductivity. However, hole doping into $BaFe_2As_2$ realized by Cr substitution for Fe dose not induce a transition into the superconducting state and antiferromagnetic (AFM) order emerges in the entire doping range [18]. Such a behavior has also been observed in Mn-doped $BaFe_2As_2$ [43]. Figure 1.15 shows the temperature dependence of the resistivity of the various hole-doped $BaFe_2As_2$, indicating that Cr- and Mn-doped $BaFe_2As_2$ (Cr-Ba122, Mn-Ba122) are non-superconducting compounds in contrast to K-doped $BaFe_2As_2$ (K-Ba122) [18, 22, 43]. For Cr-Ba122, there are anomalies in resistivity around the magnetic transition temperature T_N. Below T_N, the resistivity monotonically increases upon cooling whereas the resistivity of the parent and K-doped compounds decreases. It has been revealed by a neutron diffraction study [44] that the AFM ordering emerging for all the concentrations is not the same, indicating the presence of the checkerboard-type antiferromagnetic ordering called G-type magnetic order for higher Cr concentrations. The phase diagram of Cr-Ba122 are depicted in Fig. 1.16 (a). The stripe-type AFM order observed in the parent compound at low temperature is suppressed by doping and the G-type magnetic order supersedes the stripe-type AFM order near $x = 0.3$ with the disappearance of the tetragonal-orthorhombic structural transition. The phase diagram is very similar to that of Mn-Ba122 but distinct from that of the K-doped compounds.

Recently, the doping dependence of the in-plane resistivity anisotropy of Cr-

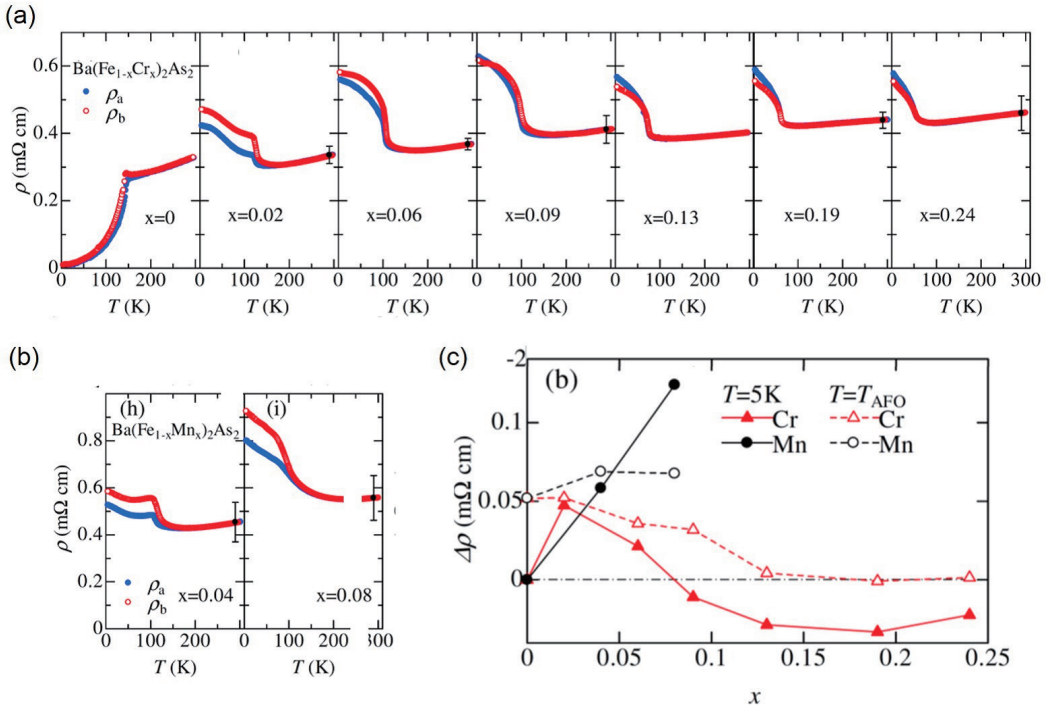

Figure 1.17: Temperature dependence of the in-plane resistivity along the a-axis (ρ_a) and the b-axis (ρ_b) of detwinned $Ba(Fe_{1-x}TM_x)_2As_2$ ($TM = Cr and Mn$). (a) $Ba(Fe_{1-x}Cr_x)_2As_2$. (b) $Ba(Fe_{1-x}Mn_x)_2As_2$. (c) Doping dependence of the resistivity difference. Reprinted from Ref. [47]

Ba122 was reported to be distinct from that of Mn-Ba122 [47]; As shown in Fig. 1.17, although the resistivity along the b-axis ρ_b is larger than that along the a-axis ρ_a for lower concentration, the difference of the resistivity $\rho_b - \rho_a$ changes its sign around $x = 0.08$ and takes the largest negative value at $x = 0.19$. Negative value of the resistivity difference $\rho_b - \rho_a$ has also been reported for K-Ba122. Namely, Cr-Ba122 has characteristic features in common with not only the non-superconducting Mn-Ba122 but also the hole-doped superconductor K-Ba122. Thus an investigation of the electronic states in Cr-Ba122 may give us clue to understand the mechanism of the resistivity anisotropy (nematicity) and superconductivity.

1.3 Te-annealed compound $FeTe_{1-x}Se_x$

As mentioned in Sec. 1.1.2, the parent compound FeTe is an AFM metal similar to the other parent compounds such as $BaFe_2As_2$. As Te in the parent compound is gradually replaced by Se, the AFM order is suppressed and superconductivity is observed. However, it has been reported that the superconductivity is affected by

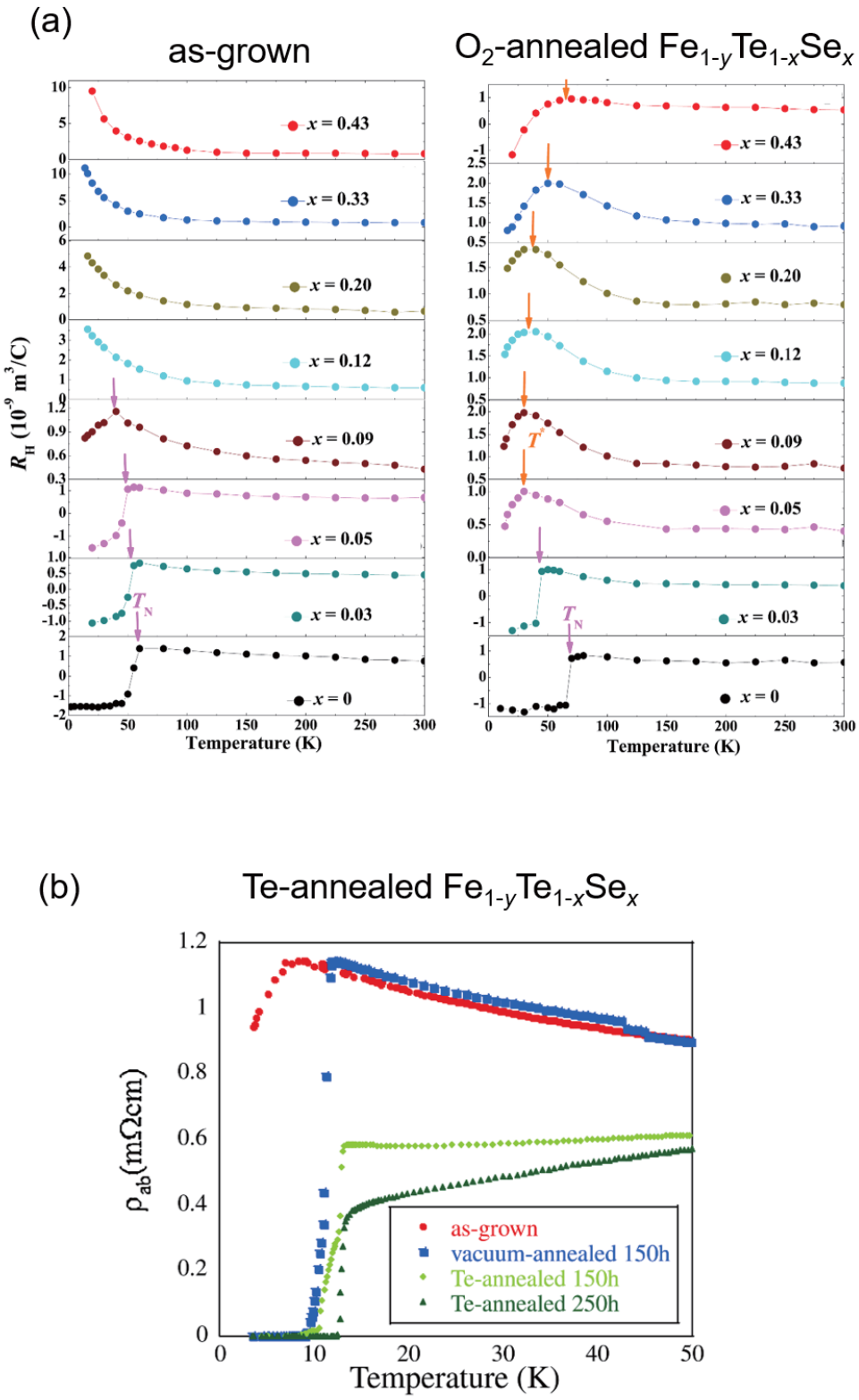

Figure 1.18: Temperature dependence of the in-plane resistivity of $Fe_{1+y}Se_xTe_{1-x}$ (a) As-grown and O_2-annealed $Fe_{1+y}Se_xTe_{1-x}$. (b) Te-annealed $Fe_{1+y}Se_xTe_{1-x}$. Reprinted from Ref. [51, 52].

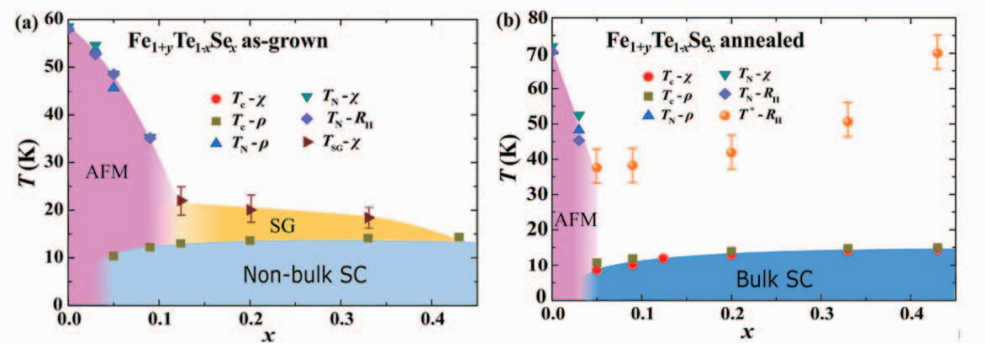

Figure 1.19: The doping-temperature phase diagrams of as-grown (a) and O_2-annealed $Fe_{1+y}Se_xTe_{1-x}$ (b), respectively. Reprinted from Ref. [51].

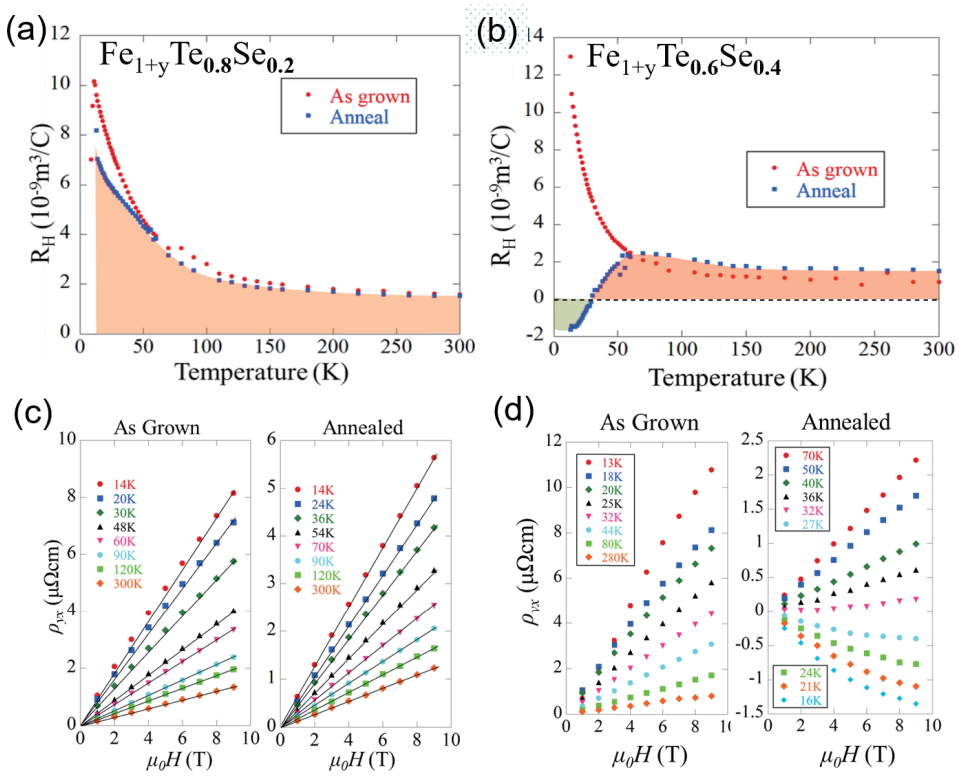

Figure 1.20: Hall effect measurement results of Te-annealed $Fe_{1+y}Se_xTe_{1-x}$ (x=0.2 and 0.4) (a) Temperature dependence of Hall coefficient of x=0.2. (b) The same as (a) for x=0.4. (c) Magnetic field dependence of the Hall resistivity for as-grown and Te-annealed sample with x=0.2. (d) The same as (c) for x=0.4 Reprinted from Ref. [53].

excess Fe atoms located at interstitial sites and very sensitive to its stoichiometry. Figure 1.19 (a) shows the phase diagram of as-grown $FeTe_{1-x}Se_x$. For as-grown samples, a bulk superconductivity is difficult to emerge and the AFM phase is expanded up to x=0.1. So far, it has been well established that the excess Fe atoms can be removed by annealing a specimen and that the superconductivity can be improved after annealing [51, 54–57]. Figure 1.18 (a) shows the transport properties of as-grown and O_2-annealed $Fe_{1-y}Te_{1-x}Se_x$. One can find that the upturn behavior at low temperature observed in the as-grown samples is suppressed after annealing. The phase diagram of O_2-annealed $Fe_{1-y}Te_{1-x}Se_x$ is shown in Fig. 1.19 (b). After annealing in the O_2 atmosphere, the AFM phase shrinks and the bulk superconductivity is realized even for $x \sim 0.05$. Moreover, in order to remove the interstitial Fe atoms completely, Koshika *et al.* have also developed an annealing method under tellurium vaper (Te-annealing) and confirmed its validity. [52] Figure 1.18 (b) shows an annealing evolution of the resistivity. Similar to the O_2-annealing, the upturn was suppressed by the Te-annealing, indicating its validity. They also confirmed that excess Fe atoms were completely removed after annealing for 250 hours. Hereafter, we focus on the Te-annealed samples.

According to Hall effect measurements, there are possibility that charge carrier concentration might change depending on the Se concentration although Se and Te are isovalent. The temperature dependence of the Hall coefficient R_H of x=0.2 and x=0.4 (almost optimal doping) are shown in Fig. 1.20. One can see that although the R_H of annealed $FeTe_{0.6}Se_{0.4}$ is almost independent of temperature above 50 K, it decreases with decreasing temperature below 50 K and eventually changes their sign from positive to negative around 30 K (Fig. 1.20 (a)). Moreover, The magnetic field dependence of the Hall resistivity ρ_{xy} is nonlinear in the low temperature region (Fig. 1.20 (c)). These results indicate the coexistence of hole- and electron-type carriers and the dominance of electrons in the charge carrier at low temperature in optimally-doped samples. On the other hand, R_H of $FeTe_{0.8}Se_{0.2}$ is always positive and shows an obvious upturn at low temperatures similar to the case of as-grown samples although the excess Fe atoms have been completely removed by Te-annealing, indicating the dominance of hole-type charge carriers over a wide temperature range. Assuming that the Fermi surface topology of $FeTe_{1-x}Se_x$ drastically changes depending on Se concentration, it is possible that different x shows the different charge carrier concentrations. However, the electronic structures of Te-annealed $FeTe_{1-x}Se_x$ have not been clarified and it has not been known whether there are differences in electronic states between conventional O_2-annealed and Te-annealed $FeTe_{1-x}Se_x$.

1.4 Purpose of this study

As introduced above, near the superconducting state, non-trivial and non-Fermi liquid-like behavior in transport properties have been observed. In order to clarify the mechanism of the superconductivity, to understand the origin of these phenomena is an important step. In the phase diagram of the 122 system, the metallic AFM phase is contiguous to the superconducting dome. Therefore, the understanding of the metallic AFM state is thought to lead to the clarification of the mechanism of the superconductivity. Especially, clarifying the origin of the non-trivial anisotropic electronic properties observed in the AFM and electronic nematic phases is essential to fully understand the AFM state. In order to clarify the electronic structure, its relationship with the anisotropic resistivity of the AFM phase of Cr-doped Ba122, we have investigated the hole-doped compound of "122"-type FeSCs, $Ba(Fe_{1-x}Cr_x)_2As_2$, by resonant photoemission spectroscopy (RPES) and angel-resolved photoemission spectroscopy (ARPES). For the 11 system, especially $FeTe_{1-x}Se_x$, magneto-transport behavior dramatically changes with varying Se concentration although superconductivity with similar transition temperatures is observed for different Se concentrations. In order to clarify the electronic structure, its relationship with the magneto-transport properties of $FeTe_{1-x}Se_x$, we have performed ARPES measurements on Te-annealed $FeTe_{1-x}Se_x$.

Chapter 2

Experimental methods and their principles

2.1 Photoemission spectroscopy

Photoemission spectroscopy (PES) is a direct experimental method to investigate the electronic structure in solids. In this section, principles of photoemission spectroscopy are introduced briefly.

2.1.1 Basic principles

When samples are irradiated with incident light which has sufficiently high energy $h\nu$, photoelectrons are emitted by absorbing the photon energy. This process is called photoemission. In a solid substance, an electron is excited to a state above the vacuum level (E^{vac}) by absorbing photons. Then it travels to the surface and escape from the sample. From the energy conservation, the kinetic energy of the electron measured from the vacuum level (E^{vac}_{kin}) and the photon energy $h\nu$ is related through the following expression:

$$E^{vac}_{kin} = h\nu - \phi - E_{\mathrm{B}}, \tag{2.1}$$

where ϕ is the work function of the sample and E_{B} is the binding energy measured from the Fermi level E_{F} or chemical potential μ. In real experiment, one can directly detect electrons with the kinetic energy E_{kin} relative to the Fermi level. Thus E_{kin} is more useful rather than E^{vac}_{kin}. The kinetic energy E_{kin} is written as

$$E_{kin} = h\nu - E_{\mathrm{B}}. \tag{2.2}$$

In the mean-field (Hartree-Fock) approximation, each electron occupies a Bloch state $\phi_{\boldsymbol{k}}$ with the energy $\varepsilon(\boldsymbol{k})$ and the wave number k and the ground state Φ_g can be

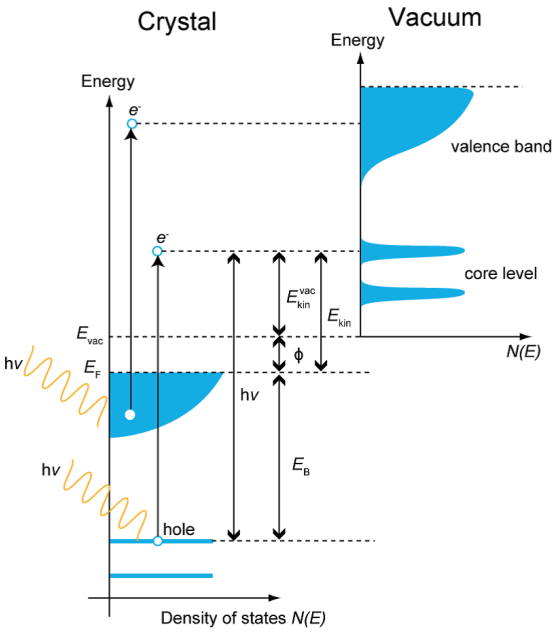

Figure 2.1: Schematic energy diagram of photoemission.

represented by a single Slater determinant. The photoemission process is regarded as the transition of an electron from the initial state $\phi_{\boldsymbol{k}_j}$ to the final state $\phi_{\boldsymbol{k}'_j}$. From the energy conservation, one can obtain

$$E_{kin} = h\nu + \varepsilon(\boldsymbol{k}_j), \tag{2.3}$$

where the energy of the Bloch electron $\varepsilon(\boldsymbol{k})$ is measured from E_{F} and $\varepsilon(\boldsymbol{k}_j)$ is equal to the negative binding energy. Thus, assuming that the cross-section of photoemission and the density of states (DOS) for free electrons are constant, the valence-band photoemission spectrum $I(E_{\mathrm{B}})$is expressed as

$$I(E_{\mathrm{B}}) \propto \sum_j \delta(\varepsilon(\boldsymbol{k}) + E_{\mathrm{B}}) \propto N(-E_{\mathrm{B}}), \tag{2.4}$$

namely, the photoemission spectrum is proportional to the density of the occupied one-electron states $N(E)$. Therefore, we can directly investigate the density of states by measuring the energy distribution of photoelectrons with monochromatic incident light.

2.1.2 Angle-resolved photoemission spectroscopy

Angle-resolved photoemission spectroscopy (ARPES) can probe not only the energies but also the momenta of electrons. In the photoexcitation process by low-

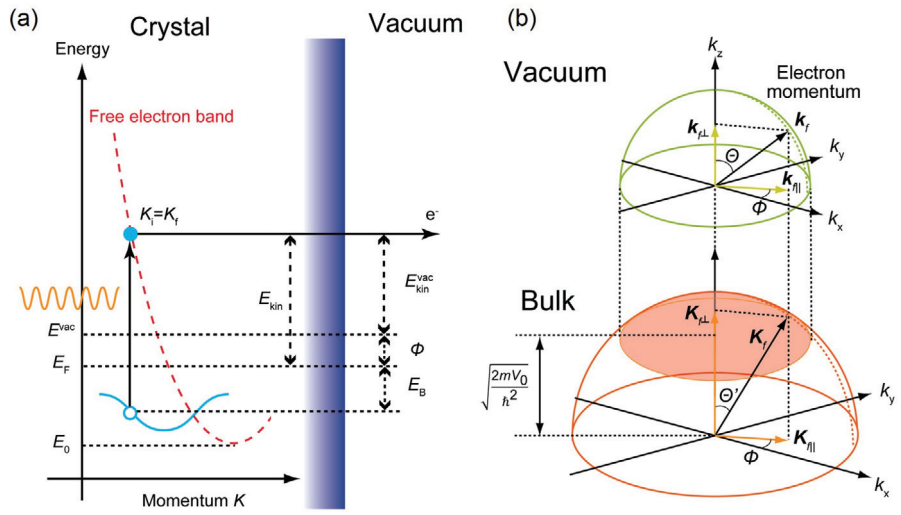

Figure 2.2: Schematic diagram of angle-resolved photoemission spectroscopy. (a) Energy levels of electrons before the photoexcitation and after emission. (b) Preparation of momentum between electrons in bulk and emitted electrons in vacuum.

energy photons of which momentum $h\nu/c$ is small enough to be neglected compared to the Brillouin Zone (BZ), the wave number of the electron is conserved before and after the excitation apart from for a reciprocal lattice vector. Therefore, the following equation is satisfied between the crystal momentum of the initial state $\boldsymbol{K}_\mathrm{i}$ and that of the final state $\boldsymbol{K}_\mathrm{f}$.

$$\boldsymbol{K}_\mathrm{i} + \boldsymbol{G} = \boldsymbol{K}_\mathrm{f}, \tag{2.5}$$

where $\boldsymbol{G} = (2n_x\pi/a, 2n_y\pi/b, 2n_z\pi/c)$ is an arbitrary reciprocal lattice vector and n_x, n_y, and n_z are integers.

When the photoelectron escapes from the sample, the wave vector parallel to the surface $\boldsymbol{K}_{\mathrm{f}\parallel}$ is conserved because of translational symmetry along the surface, whereas the wave vector perpendicular to the surface $\boldsymbol{K}_{f\perp}$ is modified due to the inner potential. Therefore, one can obtain

$$\boldsymbol{k}_{\mathrm{f}\parallel} = \boldsymbol{p}_\parallel/\hbar = \boldsymbol{K}_{\mathrm{f}\parallel} = \boldsymbol{K}_{\mathrm{i}\parallel} + \boldsymbol{G}_\parallel \tag{2.6}$$

where $\boldsymbol{k}_{\mathrm{f}\parallel}, \boldsymbol{p}_\parallel$ are the components parallel to the surface of the wave vector and the momentum, respectively. Assuming that the photoelectron in the vacuum is a free electron with the kinetic energy $E^{\mathrm{vac}}_{\mathrm{kin}}$ and the free electron mass m, the magnitude of the momentum $\boldsymbol{p}$ of the photoelectron is given by $\boldsymbol{p} = \sqrt{2mE^{\mathrm{vac}}_{\mathrm{kin}}}$ and the momentum parallel $\boldsymbol{p}_\parallel = \boldsymbol{p}_\mathrm{x} + \boldsymbol{p}_\mathrm{y}$ and perpendicular $\boldsymbol{p}_\perp = \boldsymbol{p}_\mathrm{z}$) to the surface are obtained by

using the polar emission angle θ and the azimuthal angle ϕ as:

$$p_{\mathrm{x}} = \sqrt{2mE_{\mathrm{kin}}^{\mathrm{vac}}}\sin\theta\cos\phi, \tag{2.7}$$

$$p_{\mathrm{y}} = \sqrt{2mE_{\mathrm{kin}}^{\mathrm{vac}}}\sin\theta\sin\phi, \tag{2.8}$$

$$p_{\mathrm{z}} = \sqrt{2mE_{\mathrm{kin}}^{\mathrm{vac}}}\cos\theta. \tag{2.9}$$

Summarizing Eqs. (2.1), (2.5), (2.6), (2.7), and (2.8), we obtain both the binding energy E_{B} and the parallel component $\boldsymbol{K}_{\mathrm{i}\parallel} = (K_{\mathrm{ix}}, K_{\mathrm{iy}})$ of the momentum of the hole produced in the sample by the photoemission process as

$$K_{\mathrm{ix}} = \frac{\sqrt{2m(h\nu - \phi - E_{\mathrm{B}})}}{\hbar}\sin\theta\cos\phi + \frac{2n_{\mathrm{x}}\pi}{a}, \tag{2.10}$$

$$K_{\mathrm{iy}} = \frac{\sqrt{2m(h\nu - \phi - E_{\mathrm{B}})}}{\hbar}\sin\theta\sin\phi + \frac{2n_{\mathrm{y}}\pi}{b}. \tag{2.11}$$

If the sample is a layered material, the band structure depends on the momentum $\boldsymbol{K}_{\mathrm{i}\parallel}$ parallel to the surface. In the case of a system with three-dimensional character, however, the momentum component $\boldsymbol{K}_{\mathrm{i}\perp}$ perpendicular to the sample surface should be determined. Since the perpendicular component $\boldsymbol{K}_{\mathrm{i}\perp} = \boldsymbol{K}_{\mathrm{iz}}$ is not conserved due to the inner potential, information about the final state is required to determine $\boldsymbol{K}_{\mathrm{i}\perp}$. Generally, the band dispersion of the final state in the photoexcitation process is not known and the nearly-free-electron model is applied to the final Bloch states with high energies. From the energy conversion low, one can obtain

$$E_{\mathrm{f}}(\boldsymbol{p}) = \frac{\boldsymbol{p}^2}{2m} - E_0 = \frac{\hbar^2(\boldsymbol{K}_{\parallel} + \boldsymbol{K}_{\perp})^2}{2m} + E_0, \tag{2.12}$$

where E_0 is the energy of the bottom of the free-electron band. Because $E_{\mathrm{f}} = E_{\mathrm{kin}}^{\mathrm{vac}} + \phi + \mu$, one obtains

$$K_{\mathrm{iz}} = \frac{\sqrt{2m(E_{\mathrm{kin}}^{\mathrm{vac}}\cos^2\theta + V_0)}}{\hbar} + \frac{2n_{\mathrm{z}}\pi}{c}, \tag{2.13}$$

where $V_0 = \Phi + \mu - E_0 = E^{vac} - E_0$ is the inner potential and determined experimentally and μ is the chemical potential. If the inner potential is known, the corresponding value of $K_{\mathrm{i}\perp}$ can be obtained. Based on the above principles, one can directly investigate the band dispersion of electrons in solids using ARPES.

2.1.3 Spectral function and Green's function

In the case of a system in which electrons strongly interact with each other such as the iron-based superconductors, the one-electron approximation is no longer

valid and many-body effects must be taken into account. In the process of photoemission (inverse-photoemission), when an electron is removed from (added to) the ground state $|\Psi_g^N\rangle$ of the N-electron system with the energy E_g^N, the system changes into an excited state $|\Psi_g^{N-1}\rangle$ ($|\Psi_g^{N+1}\rangle$) of the $(N-1)$-electron ($(N+1)$-electron) system with energy E_f^{N-1} (E_f^{N+1}). Thus one can obtain the spectral function corresponding to the intensity of photoemission and inverse photoemission spectra as

$$A_{\mathrm{PES}}(\boldsymbol{k},\omega) = \sum_f |\langle\Psi_f^{N-1}|c_{\boldsymbol{k}}|\Psi_g^N\rangle|^2 \delta(\omega + E_{\mathrm{f}}^{N-1} - E_{\mathrm{g}}^N), \tag{2.14}$$

$$A_{\mathrm{IPES}}(\boldsymbol{k},\omega) = \sum_f |\langle\Psi_f^{N+1}|c_{\boldsymbol{k}}^\dagger|\Psi_g^N\rangle|^2 \delta(\omega - E_{\mathrm{f}}^{N+1} + E_{\mathrm{g}}^N), \tag{2.15}$$

where c_k and $c_{\boldsymbol{k}}^\dagger$ are the annihilation and creation operators of a Bloch electron with momentum $\boldsymbol{k}$, respectively. $\omega \equiv \varepsilon_{\mathrm{kin}} - h\nu$. $\omega < \mu$ and $\omega > \mu$ corresponds to the photoemission and inverse-photoemission processes, respectively. $A_{\mathrm{PES}}(\boldsymbol{k},\omega)$ and $A_{\mathrm{IPES}}(\boldsymbol{k},\omega)$ describe the probability with which an electron can be taken from and added to the system in its ground state. Moreover, one can define the spectral function $A(\boldsymbol{k},\omega)$ as

$$\begin{aligned} A(\boldsymbol{k},\omega) = &\sum_f |\langle\Psi_f^{N-1}|c_k|\Psi_g^N\rangle|^2 \delta(\omega + E_{\mathrm{f}}^{N-1} - E_{\mathrm{g}}^N) \\ &+ \sum_f |\langle\Psi_f^{N+1}|c_k^\dagger|\Psi_g^N\rangle|^2 \delta(\omega - E_{\mathrm{f}}^{N+1} + E_{\mathrm{g}}^N). \end{aligned} \tag{2.16}$$

The spectral function $A(\boldsymbol{k},\omega)$ is related to a fundamental property of the N-electron system. Namely, the functions are rewritten by using one-particle Green's function. Using the field operator $\hat{\psi}^\dagger(\boldsymbol{x}',0)$ ($\hat{\psi}(\boldsymbol{x}',0)$) that creates an electron (hole) in the ground state $|\Psi_{\mathrm{g}}^N\rangle$ of the N-electron system at $\boldsymbol{x}' \equiv (r',s')$ (r' and s' are position and spin coordinate, respectively) at time $t=0$, the Green's function called as retarded Green's function can be expressed as a summation of the probability amplitude $\theta(t)\langle\Psi_{\mathrm{g}}^N|\hat{\psi}(\boldsymbol{x}',t)\hat{\psi}^\dagger(\boldsymbol{x}',0)|\Psi_{\mathrm{g}}^N\rangle$ that an electron will be found at $\boldsymbol{x}'$ at time $t>0$ and $\theta(t)\langle\Psi_{\mathrm{g}}^N|\hat{\psi}^\dagger(\boldsymbol{x}',0)\hat{\psi}(\boldsymbol{x}',t)|\Psi_{\mathrm{g}}^N\rangle$ that a hole will be found:

$$G(\boldsymbol{x},\boldsymbol{x}',t) = -\frac{i}{\hbar}\theta(t)\langle\Psi_{\mathrm{g}}^N|\{\hat{\psi}(\boldsymbol{x}',t),\hat{\psi}^\dagger(\boldsymbol{x}',0)\}|\Psi_{\mathrm{g}}^N\rangle, \tag{2.17}$$

where θ is the Heaviside step function, $\{A,B\} \equiv AB+BA$ is the anticommutator, and $A(t) \equiv e^{iHt}A(0)e^{-iHt} = e^{iHt}Ae^{-iHt}$. Performing the Fourier transformation of Eq. (2.17) and replace the field operators by those of Bloch states $\psi_{\boldsymbol{k}}(\boldsymbol{x})$: $\hat{\psi}(\boldsymbol{x}) \equiv \sum_{\boldsymbol{k}} c_{\boldsymbol{k}}\psi_{\boldsymbol{k}}(\boldsymbol{x})$, $\hat{\psi}^\dagger(\boldsymbol{x}) \equiv \sum_{\boldsymbol{k}} c_{\boldsymbol{k}}^\dagger\psi_{\boldsymbol{k}}^*(\boldsymbol{x})$, the one-particle Green's function is written as the

following equation.

$$
\begin{aligned}
G(\boldsymbol{k},\omega) &= -\frac{i}{\hbar}\int_0^\infty dt e^{\frac{it}{\hbar}(\omega t+i0^+)}\theta(t)\left\langle\Psi_{\rm g}^N\right|\{c_{\boldsymbol{k}}(t),c_{\boldsymbol{k}}^\dagger\}\left|\Psi_{\rm g}^N\right\rangle \\
&= -\frac{i}{\hbar}\int_0^\infty dt e^{\frac{it}{\hbar}(\omega t+i0^+)}\theta(t)\left(\left\langle\Psi_{\rm g}^N\right|e^{iHt}c_{\boldsymbol{k}}e^{-iHt}c_{\boldsymbol{k}}^\dagger\left|\Psi_{\rm g}^N\right\rangle+\left\langle\Psi_{\rm g}^N\right|c_{\boldsymbol{k}}^\dagger e^{iHt}c_{\boldsymbol{k}}e^{-iHt}\left|\Psi_{\rm g}^N\right\rangle\right) \\
&= -\frac{i}{\hbar}\int_0^\infty dt e^{\frac{it}{\hbar}(\omega t+i0^+)}\theta(t)e^{iE_{\rm g}^N t}\left(\left\langle\Psi_{\rm g}^N\right|c_{\boldsymbol{k}}e^{-iHt}c_{\boldsymbol{k}}^\dagger\left|\Psi_{\rm g}^N\right\rangle+e^{-iE_{\rm g}^N t}\left\langle\Psi_{\rm g}^N\right|c_{\boldsymbol{k}}^\dagger e^{iHt}c_{\boldsymbol{k}}\left|\Psi_{\rm g}^N\right\rangle\right) \\
&= \left\langle\Psi_{\rm g}^N\right|c_{\boldsymbol{k}}^\dagger\frac{1}{\omega+i0^++H-E_{\rm g}^N}c_{\boldsymbol{k}}\left|\Psi_{\rm g}^N\right\rangle+\left\langle\Psi_{\rm g}^N\right|c_{\boldsymbol{k}}\frac{1}{\omega+i0^+-H+E_{\rm g}^N}c_{\boldsymbol{k}}^\dagger\left|\Psi_{\rm g}^N\right\rangle \\
&= \sum_{\rm f}\frac{|\left\langle\Psi_{\rm f}^{N-1}\right|c_{\boldsymbol{k}}\left|\Psi_{\rm g}^N\right\rangle|^2}{\omega+i0^++E_{\rm f}^{N-1}-E_{\rm g}^N}+\sum_{\rm f}\frac{|\left\langle\Psi_{\rm f}^{N+1}\right|c_{\boldsymbol{k}}^\dagger\left|\Psi_{\rm g}^N\right\rangle|^2}{\omega+i0^+-E_{\rm f}^{N+1}+E_{\rm g}^N}, \\
&= \sum_{\rm f}|\left\langle\Psi_{\rm f}^{N-1}\right|c_{\boldsymbol{k}}\left|\Psi_{\rm g}^N\right\rangle|^2\left[\frac{\rm P}{\omega+E_{\rm f}^{N-1}-E_{\rm g}^N}-i\pi\delta(\omega+E_{\rm f}^{N-1}-E_{\rm g}^N)\right] \\
&+ \sum_{\rm f}|\left\langle\Psi_{\rm f}^{N+1}\right|c_{\boldsymbol{k}}^\dagger\left|\Psi_{\rm g}^N\right\rangle|^2\left[\frac{\rm P}{\omega-E_{\rm f}^{N+1}+E_{\rm g}^N}-i\pi\delta(\omega-E_{\rm f}^{N+1}+E_{\rm g}^N)\right],
\end{aligned}
\tag{2.18}
$$

where H denotes the Hamiltonian of the solids and P is the principal value of the integral. Here, we used a formula $1/(x+i0^+)={\rm P}/(x-i\pi\delta(x))$ and the completeness relation $\sum_{n,i}|\Psi_{\rm i}^n\rangle\langle\Psi_{\rm i}^n|=\hat{1}$. The real and imaginary parts of the Green's function $G(\boldsymbol{k},\omega)$ satisfy the Kramers-Kronig relation,

$$
{\rm Re}G(\boldsymbol{k},\omega)=\frac{1}{\pi}{\rm P}\int_{-\infty}^{\infty}d\omega'\frac{{\rm Im}G(\boldsymbol{k},\omega')}{\omega-\omega'}, \tag{2.19}
$$

$$
{\rm Im}G(\boldsymbol{k},\omega)=-\frac{1}{\pi}{\rm P}\int_{-\infty}^{\infty}d\omega'\frac{{\rm Re}G(\boldsymbol{k},\omega')}{\omega-\omega'}. \tag{2.20}
$$

${\rm Im}G(\boldsymbol{k},\omega)$ represents the energy dissipation and describes the probability of the electron removal and addition. Thus, the imaginary part of the one-particle Green's function $G(\boldsymbol{k},\omega)$ is equal to the spectral function $A(\boldsymbol{k},\omega)$.

$$
\begin{aligned}
-\frac{1}{\pi}{\rm Im}G(\boldsymbol{k},\omega) &= \sum_{\rm f}|\left\langle\Psi_{\rm f}^{N-1}\right|c_{\boldsymbol{k}}\left|\Psi_{\rm g}^N\right\rangle|^2\delta(\omega+E_{\rm f}^{N-1}-E_{\rm g}^N) \\
&+ \sum_{\rm f}|\left\langle\Psi_{\rm f}^{N+1}\right|c_{\boldsymbol{k}}^\dagger\left|\Psi_{\rm g}^N\right\rangle|^2\delta(\omega-E_{\rm f}^{N+1}+E_{\rm g}^N) \\
&= A(\boldsymbol{k},\omega).
\end{aligned}
\tag{2.21}
$$

2.1.4 Self-energy

In the one-electron approximation, according to Koopmans' theorem, using the energy of one Bloch state $\Phi_{\boldsymbol{k}}$ as $\varepsilon_{\boldsymbol{k}}$,

$$E_{\rm f}^{N+1} - E_{\rm g}^{N} = \varepsilon_{\boldsymbol{k}} \quad (\text{if } \phi_{\boldsymbol{k}} \text{ is unoccupied}), \tag{2.22}$$

$$E_{\rm f}^{N-1} - E_{\rm g}^{N} = -\varepsilon_{\boldsymbol{k}} \quad (\text{if } \phi_{\boldsymbol{k}} \text{ is occupied}). \tag{2.23}$$

Substituting Eqs. (2.22) and (2.23) into Eq. (2.18), the one-particle Green's function $G(\boldsymbol{k},\omega)$ is written as

$$G(\boldsymbol{k},\omega) = \frac{1}{\omega - \varepsilon_{\boldsymbol{k}} + i0^{+}}. \tag{2.24}$$

Thus, the spectral function $A(\boldsymbol{k},\omega)$ should have a peak structure of which the width is infinitely narrow at the energy $\omega = \varepsilon_{\boldsymbol{k}}$:

$$A(\boldsymbol{k},\omega) = \delta(\omega - \varepsilon_{\boldsymbol{k}}). \tag{2.25}$$

In the presence of electron-electron interaction, electrons and holes are regarded as elementary excitations (quasi-particles). The quasi-particle has a finite lifetime and its energy deviates from the original energy $\omega = \varepsilon_{\boldsymbol{k}}$. Introducing the self-energy $\Sigma(\boldsymbol{k},\omega)$, of which the real and imaginary parts signify the energy shift and the lifetime width of the quasi-particle, respectively, $G(\boldsymbol{k},\omega)$ can be modified as:

$$G(\boldsymbol{k},\omega) = \frac{1}{\omega - \varepsilon_{\boldsymbol{k}} - \Sigma(\boldsymbol{k},\omega)}. \tag{2.26}$$

This equation is called Dyson's equation. The modified spectral function is given by

$$A(\boldsymbol{k},\omega) = \frac{1}{\pi} \frac{-{\rm Im}\Sigma(\boldsymbol{k},\omega)}{[\omega - \varepsilon_{\boldsymbol{k}} - {\rm Re}\Sigma(\boldsymbol{k},\omega)]^2 + [{\rm Im}\Sigma(\boldsymbol{k},\omega)]^2}. \tag{2.27}$$

Therefore, the energy of a quasi-particle peak $\omega = \varepsilon_{\boldsymbol{k}}^{*}$ is obtained as a solution of the following equation,

$$\omega = \varepsilon_{\boldsymbol{k}} + {\rm Re}\Sigma(\boldsymbol{k},\omega). \tag{2.28}$$

The momentum dependence of the quasi-particle peak represents the quasi-particle band structure. By performing Taylor expansion on ${\rm Re}\Sigma(\boldsymbol{k},\omega)$ around $\omega = \varepsilon_{\boldsymbol{k}}^{*}$ in Eq. (2.26), one can obtain

$$A(\boldsymbol{k},\omega) \simeq \frac{z_{\boldsymbol{k}}(\varepsilon_{\boldsymbol{k}}^{*})}{\pi} \frac{-z_{\boldsymbol{k}}(\varepsilon_{\boldsymbol{k}}^{*}){\rm Im}\Sigma(\boldsymbol{k},\varepsilon_{\boldsymbol{k}}^{*})}{[\omega - \varepsilon_{\boldsymbol{k}}^{*}]^2 + [z_{\boldsymbol{k}}(\varepsilon_{\boldsymbol{k}}^{*}){\rm Im}\Sigma(\boldsymbol{k},\omega)]^2}, \tag{2.29}$$

where $z_{\boldsymbol{k}}(\varepsilon^*_{\boldsymbol{k}}) \equiv [1 - \frac{\partial \mathrm{Re}\Sigma(\boldsymbol{k},\omega)}{\partial \omega}]^{-1} (< 1)$ is the renormalization factor. Equation (2.29) indicates that the spectral function near the quasi-particle peak can be approximated by a Lorentz function with a spectral weight of $z_{\boldsymbol{k}}(\varepsilon^*_{\boldsymbol{k}})$ and a full width at half maximum (FWHM) of $-2z_{\boldsymbol{k}}(\varepsilon^*_{\boldsymbol{k}})\mathrm{Im}\Sigma(\boldsymbol{k},\omega)$.

As mentioned above, the real and imaginary parts of the Green's function $G(\boldsymbol{k},\omega)$ follow the Kramers-Kronig relation because the function is a linear response function. Thus, $\mathrm{Re}\Sigma(\boldsymbol{k},\omega)$ and $\mathrm{Im}\Sigma(\boldsymbol{k},\omega)$ also follow the Kramers-Kronig relation.

2.1.5 polarization dependence of matrix elements

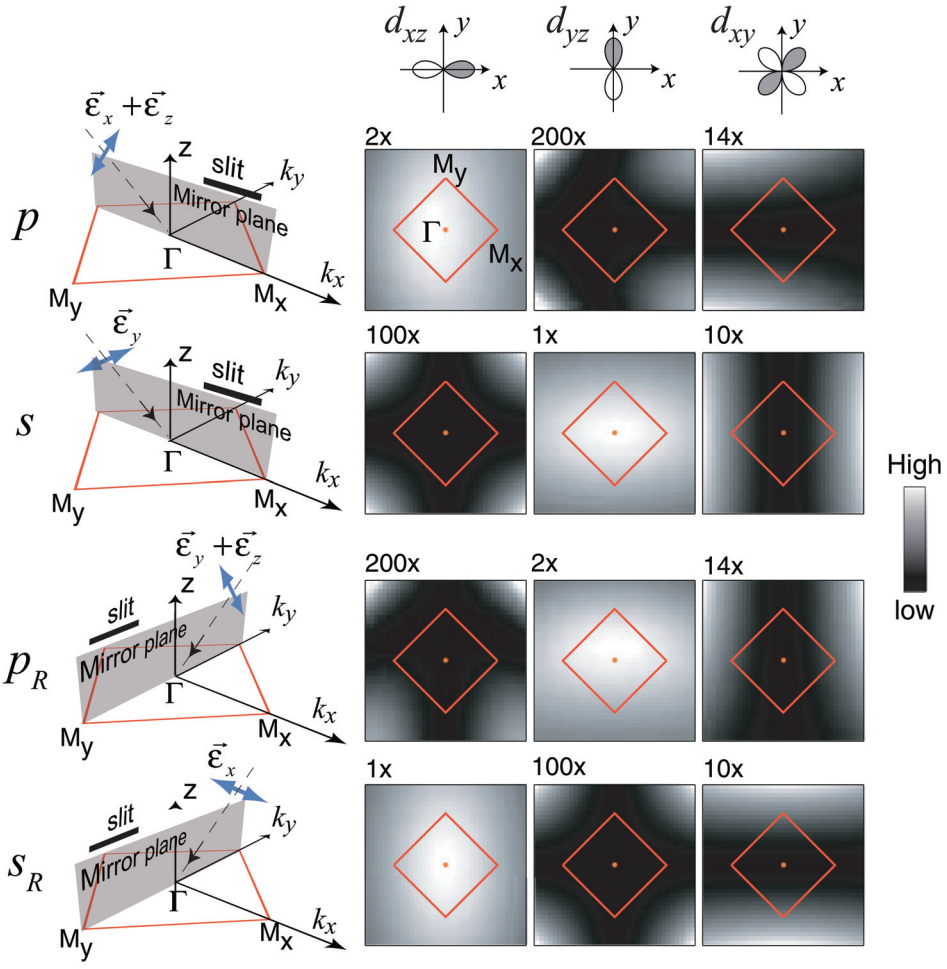

Figure 2.3: The experimental geometry and matrix element calculations for three $3d$ orbitals (d_{xz}, d_{yz}, and d_{xy}). Reprinted from Ref. [58].

The intensity obtained by the photoemission experimentally is proportional to

the matrix element of the photoemission process, which is described by

$$|M^{\boldsymbol{k}}_{f,i}| \propto |\langle \Phi^{\boldsymbol{k}}_f | \hat{\varepsilon} \cdot \boldsymbol{r} | \Phi^{\boldsymbol{k}}_i \rangle|^2, \tag{2.30}$$

where $\hat{\varepsilon}$ is a unit vector of the electric field of the incident light, $\Phi^{\boldsymbol{k}}_f$ and $\Phi^{\boldsymbol{k}}_i$ are the final- and initial-state wave functions. When the kinetic energy of electrons is significantly high, the final state can be approximated by a plane-wave state $e^{i\boldsymbol{k}\cdot\boldsymbol{r}}$, which is always even with respect to the mirror plane. For the s (p) experimental geometry, $\hat{\varepsilon} \cdot \boldsymbol{r}$ is odd (even) because $\hat{\varepsilon}$ is perpendicular (parallel) to the mirror plane. Therefore, the odd (even) initial state has a finite matrix element and the matrix element of the even (odd) initial state becomes zero. Consequently, only the odd (even) initial state can be detected by the photoemission. Figure 2.3 shows the experimental geometry and matrix element calculations for three $3d$ orbitals (d_{xz}, d_{yz}, and d_{xy}). Since the three bands have different matrix elements each other, one can choose the observable bands by tuning the experimental setup.

2.1.6 Resonant photoemission spectroscopy

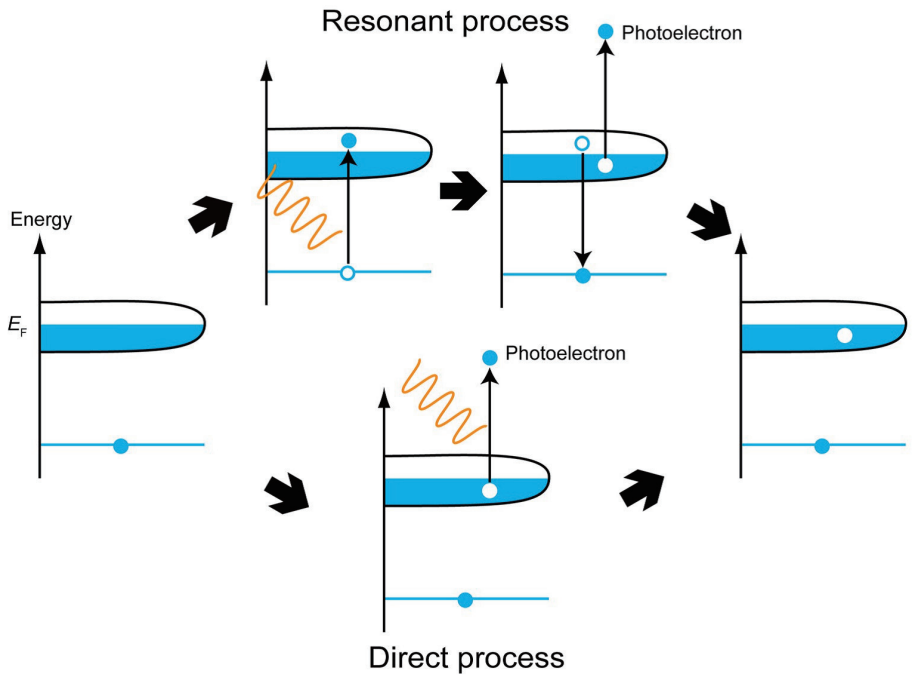

Figure 2.4: Principle of resonant photoemission spectroscopy. The upper path is Coster-Kronig process and the lower path is direct process.

Measurements of photoemission spectra using incident photons with energies close to the binding energy of a core level of a specific atom is called resonant

photoemission spectroscopy. Suppose that the energy of the incident photon is equal to the difference between the energy of the core level (e.g. transition-metal $2p$ level) and that of the valence band (e.g. transition-metal $3d$ band). An electron can be emitted from the valence band to an unoccupied state above the vacuum level (direct photoemission process):

$$p^6 d^N + h\nu \rightarrow p^6 d^{N-1} + e^-. \tag{2.31}$$

Also, a process called Coster-Kronig decay following the core-to-valence absorption occurs. In this process, the electron excited from the core level to a state above the Fermi level decays into the core-hole and an Auger electron is emitted.

$$p^6 d^N + h\nu \rightarrow p^5 d^{N+1} \rightarrow p^6 d^{N-1} + e^-. \tag{2.32}$$

Schematic diagrams of the above two processes are depicted in Fig. 2.4. Since one cannot differentiate between these two final states, the direct photoemission of the valence-band electron interferes quantum-mechanically with the electron emitted by the Coster-Kronig process, and the photoemission intensity of valence band is resonantly enhanced. From the principle of superposition, the photoemission intensity $N(h\nu)$ is obtained as a function of the photon energy $h\nu$ shows the so-called Fano lineshape,

$$\frac{(\varepsilon+q)^2}{\varepsilon^2+1}, \ \ \varepsilon = \frac{h\nu - h\nu_{\mathrm{j}}}{\Delta(h\nu_{\mathrm{j}})/2}, \tag{2.33}$$

where $h\nu_{\mathrm{j}}$ is the binding energy of the core level, q is a parameter for the particular core level, and $\Delta(h\nu_{\mathrm{j}})$ is the width (FWHM) of the core level. The photoemission intensity at a fixed binding energy as a function of photon energy is called constant-initial-state (CIS) spectrum. By using synchrotron radiation, one can perform PES measurements while changing the photon energy continuously and the photon-energy dependence of the photoemission intensity can be revealed. Furthermore, investigating the CIS spectra and analyzing difference between the on-resonance spectrum and the off-resonance spectrum, one can obtain the partial density of state (PDOS) of a particular atomic orbital.

2.2 X-ray absorption spectroscopy

X-ray absorption spectroscopy is measurements of photo-absorption by excitation of a core electron into unoccupied state for photon energies. According to the Fermi golden rule, the intensity $I(h\nu)$ of photo-absorption is written as

$$I(h\nu) = \sum_{\mathrm{f}} |\langle \Psi_{\mathrm{f}}|T|\Psi_{\mathrm{i}}|^2\rangle \, \delta(E_{\mathrm{i}} - E_{\mathrm{f}} - h\nu), \tag{2.34}$$

where T is the dipole transition operator. In the dipole transition process, transitions accompanied by a change of the angular momentum by ± 1 are dominant. Since the binding energy of core levels varies from atom to atom, one can observe the excitation of electrons of a specific atom between particular orbitals by using photons of which energy is equal to the energy difference between the orbitals. For example, in the 3d transition compounds, excitation from p core level into $3d$ orbital allows us to know information on magnetism.

There are three methods to measure XAS spectra: the transmission mode, the total-electron-yield (TEY) mode, and the total-fluorescence-yield (TFY) mode. The transmission mode which measure intensity of transmitted light is the most direct way but can be applied to the case of limited samples such as very thin film. Thus, in the soft X-ray range, TEY mode that measure an electric current corresponding to emission of the photoelectrons and Auger electrons by the photo-absorption is commonly used. Because this mode can detects the photo-absorption of electrons near the sample surface, a clean surface is required for the measurement.

2.3 Experimental setup

2.3.1 Photoemission measurement system

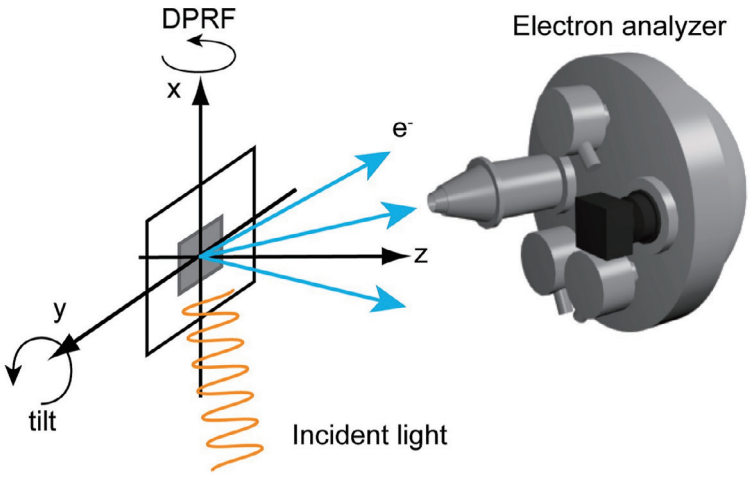

Figure 2.5: Experimental arrangement of sample and electron energy analyzer in ARPES measurement.

Generally, basic equipments for ARPES mainly consists of a monochromatic light source such as X-ray tube, a hemispherical electron analyzer, a manipulator for sample transfer, and ultrahigh vacuum evacuation systems. Samples are introduced

in the bank chamber and transferred to the main chamber through the preparation chamber. To get a clean surface of the sample, it is cleaved under ultrahigh vacuum conditions. The photoelectrons entering the electron lens are focused by electrostatic field and decelerated by a retarding potential V_R. The hemispherical analyzer allows electrons with the particular energy (pass energy E_P) pass through. The pass energy E_P is given by

$$E_P = E_{kin} - eV_R - \phi_A, \tag{2.35}$$

$$= \frac{eV_P}{R_2/R_1 - R_1/R_2}, \tag{2.36}$$

where ϕ_A is the work function of the analyzer, V_R is a potential difference between the inner and outer hemispheres of the analyzer, and R_1 and R_2 are radii of the inner and outer hemispheres, respectively, and these are shown in Fig.2.6. The energy resolution of the hemispherical analyzer depends on the slit width w between the hemispheres:

$$\Delta E = \frac{wE_P}{(R_1 + R_2)}. \tag{2.37}$$

The kinetic energy E_{kin} can be changed continuously by sweeping E_P or V_R. In real experiments, the pass energy E_P kept as a constant, V_R is swept so that ΔE is fixed regardless of E_{kin}. Electrons that pass through the analyzer slit are multiplied by a multi-channel plate (MCP) and collide against the fluorescent screen. Finally bright spots corresponding to the collisions of electrons are detected by a CCD camera.

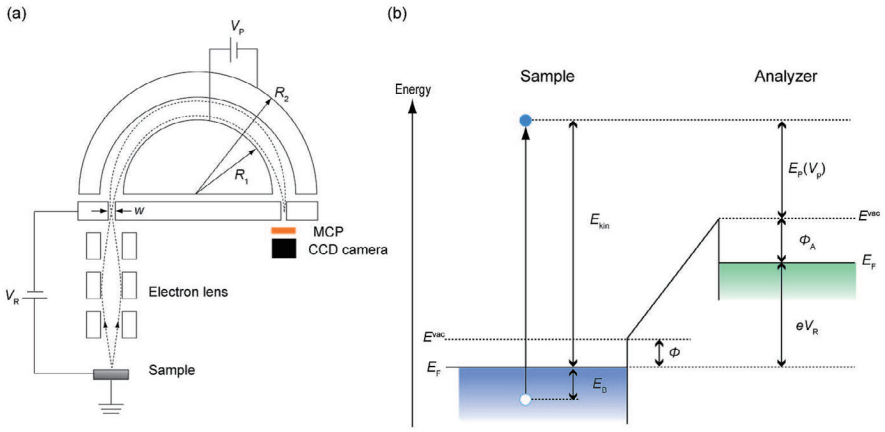

Figure 2.6: Principle of electron energy analyzer. (a) Schematic configuration of hemispherical analyzer. Electrons emitted from sample follow broken lines. (b) Relation between the photoelectron and the retarding potential V_R.

2.3.2 Photon Factory beamline 28A

We describe the beamline 28A of Photon Factory (PF) in High Energy Accelerator Research Organization (KEK) and its end station. In the beamline 28A, the variable polarization undulator is inserted with a Varied Line Spacing Plane Grating Monochromator (VLS-PGM). One can use a range of photon energy from 30 eV to 300 eV corresponding to vacuum ultraviolet and soft X-ray, and both the linearly and circularly polarized light are available. The beam has spot size of 350 μm (horizontal) $\times$ 50 μm (vertical). The endstation of this beamline consists of three chamber: a load lock chamber (bank chamber), a preparation chamber, and a main chamber, and one can exchange samples keeping ultrahigh vacuum in the main chamber. The vacuum level in the main chamber reaches $\sim 10^{-11}$ Torr and the sample is cleaved in the main chamber. In the main chamber a hemispherical analyzer Gammadata Scienta SES-2002 with a two dimensional MCP detector is installed. The analyzer slit is arranged in parallel relative to the ground. Thus Fermi surface mapping are carried out by sweeping the tilt (ϕ) angle. The manipulator has five degrees of freedom: three translational (x, y, z) and two rotational (θ, ϕ). Sample temperature can be varied from 5 K$\sim$300 K and the total energy resolution of 15 meV $\sim$ 25 meV are realized in real ARPES measurement.

2.3.3 Photon Factory beamline 2A

Next, we describe the beamline 2A of PF in KEK. The beamline 2A is established for studies of the surface and interfacial properties using light in a range of energy from vacuum ultraviolet (VUV) to Soft X-ray (SX). Two undulators for VUV (30$\sim$300 eV) and for SX (250$\sim$2000 eV) are arranged in tandem and a variable-including-angle Monk-Gillieson monochromator with varied-line-spacing gratings is installed to supply high flux and high energy resolution beam over a wide range of photon energy from 30 eV to 2000 eV at the same position. Thus this beamline is named Multiple Undulator beamline for Spectroscopic Analysis on Surface and HeteroInterface (MUSASHI). In the VUV range, linear and circular polarization can be used as the beamline 28A. The composition of its endstation is almost the same as that of beamline 28A: a bank chamber, a preparation chamber, a main chamber, a hemispherical analyzer (Scienta SES-2002), and a 5-axis manipulator (i-GONIO). A chamber of laser MBE system is connected to the preparation chamber. The vacuum level in the main chamber reaches $\sim 10^{-11}$ Torr. The energy resolution defined as $E/\Delta E$ is larger than 20,000 in VUV region, and 10,000 in SX region. In this beamline, one can perform not only ARPES measurements but also XAS measurements in TEY mode.

2.3.4 Stanford Synchrotron Radiation Lightsource beamline 5-4

Here we describe beamline 5-4 of Stanford Synchrotron Radiation Lightsource (SSRL). Beamline 5-4 is an undulator beamline and a Normal Incidence Monochromator (NIM) optimized for high-resolution ARPES is used. The energy range is 10 to 30 eV with energy resolution $E/\Delta E$ of $\sim 10^{-4}$. The spot size is 0.5 mm (height) $\times$ 0.6 mm (width). The endstation of beamline 5-4 is composed of a load-lock chamber, a preparation chamber, an upper chamber, and a lower chamber. Samples are cleaved in the upper chamber and measurement is carried out in the lower chamber. The analyzer installed in the lower chamber is Gammadata Scienta R4000. The analyzer slit is arranged in perpendicular to the ground. Therefore, the DPRF (θ) angle should be swept for Fermi surface mapping.

2.3.5 UVSOR beamline 7U

Here we describe beamline 7U of beamline 7U of Ultra Violet Synchrotron Orbital Radiation(UVSOR) Synchrotron Facility, Institute for Molecular Science. Beamline 7U provide a high photon flux with high energy resolution mainly for high-resolution ARPES. The light source is an APPLE-II-type variable -polarization undulator. The energy range is 6 to 40 eV with energy resolution $E/\Delta E$ of more than $\sim 10^{-4}$ with a photon flux of 10^{11}-10^{12} ph/s or higher. As an electron analyzer, a 200 mm-radius hemispherical photoelectron analyzer (MB Scientific AB, A-l analyzer) is installed. Horizontal and Vertical polarized photons are basically available in the wide energy region. At lowest temperature of $\sim$5 K, the total energy resolution of 6 meV are realized in real ARPES measurement.

2.4 Detwinning method

Most of the parent compounds of the iron-based superconductors undergo a magneto-structural transition as temperature becomes lower, accompanied by the rotational symmetry breaking of electronic structure. In the lower temperature phase, materials form structural twins, which makes it difficult to observe intrinsic electronic structure. So far, it has been reported that applying uniaxial stress (either compressive or tensile) along the principal axis prevent samples forming twins. In general, the orthorhombic principle a/b axis (Fe-Fe direction) in iron pnictides is rotated by 45° relative to the tetragonal principle a'/b' axis (Fe-As direction). In order to get the detwinned single crystal, one should apply uniaxial pressure along to the a/b axis. Therefore, we determine the direction of the axis by the back-reflection Laue method and cut the sample along the a/b axis. To apply the uniaxial pressure, detwinning devices shown in Fig. 2.7 were used. Under compressive uni-

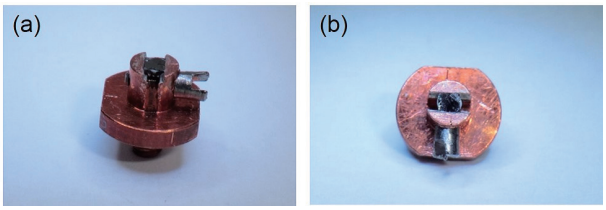

Figure 2.7: The detwinning device for ARPES measurement. (a) bird's-eye view. (b) top view.

axial pressure, shorter axis b is oriented along the direction of pressure and longer axis a is perpendicular to the stress.

2.5 WIEN2k

In order to obtain knowledge of electronic structure, we have carried out first-principle band calculations with WIEN2k package. WIEN2k is a program package for calculation of electronic structure in solids using the density functional theory (DFT). It is based on the (linearized) augmented plane wave + local orbitals method ((L)APW+lo) with no shape approximation called a "full-potential" method. In the DFT calculation, one can use the local spin density approximation (LSDA) and the generalized gradient approximation (GGA). In this study, we adopted GGA. Comparing the electronic structure predicted by the band calculation and experimental results help us to reveal the property of the band structure.

Chapter 3

Resonant photoemission study of $Ba(Fe_{1-x}Cr_x)_2As_2$

3.1 Introduction

As explained in Chap. 1, for $BaFe_2As_2$ (Ba122), hole doping realized by K substitution for Ba [50] have been successful in inducing superconductivity. However, hole doping $BaFe_2As_2$ realized by Cr substitution for the Fe site dose not undergo a transition into the superconducting state and antiferromagnetic (AFM) ordering emerges in the entire doping range [18]. Such a behavior has also been observed in Mn-doped $BaFe_2As_2$ [43]. For Cr-Ba122, there are anomalies in resistivity around the temperature corresponding to the magnetic transition temperature T_N. Below T_N, the resistivity monotonically increases upon cooling whereas the resistivity of the parent and K-doped compounds decreases, indicating that doped Cr atoms are strong scatter. So far, for the Mn-doped Ba122, electronic structure have been investigated [59]. In the Mn-doped Ba122, since Mn2+ has five $3d$ electrons, half of ten orbitals are occupied. In that case, on-site Coulomb interaction U and Hund ' s coupling J induce splitting between the majority and minority spin states. Consequently, Mn $3d$ is localized and its partial density of states is located $\sim$ 5 eV below the Fermi level E_F. Therefore, Mn-doping does not introduce hole carriers into the FeAs plane and it is considered that the localization of $3d$ electrons is attributed to the missing superconductivity. On the other hand, for Cr-doped Ba122, most of the previous reports were related to transport measurements. Although angle-resolved photoemission spectroscopy measurements have been curried out for one of the parent compounds $BaCr_2As_2$ [60, 61], there are no spectroscopic studies to investigate electronic structure of Cr-doped Ba122. In this chapter, we report the electronic structure of Cr in Ba(Fe0:81Cr0:19)2As2 investigated by using the resonant photoemission spectroscopy (RPES) and x-ray absorption spectroscopy (XAS) techniques. XAS results at the Cr L-edge shows a characteristic of metallic Cr 3d

electrons. For RPES, a broad Auger peak and the Fermi edge were observed, exhibiting that the Cr 3d electrons are itinerant. However, although Fe partial density of states (PDOS) is located in the vicinity of EF, Cr 3d PDOS deduced has a main feature at the binding energy of $\sim$1 eV, indicating that the Cr 3d electrons are relatively localized. We consider that the on-site Coulomb repulsion U and Hund ' s coupling J play important roles in the partial localization of the Cr 3d electrons. Then the high spin state is realized at the Cr site due to these interaction. Similar to the Mn-doped compound $Ba(Fe_{1-x}Mn_x)_2As_2$, the high spin state would favor the antiferromagnetism and be detrimental to the superconductivity.

3.2 Experiment

High-quality single crystals of $Ba(Fe_{0.81}Cr_{0.19})_2As_2$ were provided by Prof. Tajima and Dr. Kobayashi of Osaka Univ.. They were grown by the self-flux method and post-annealed [62]. The compositions of the crystals were determined by scanning electron microscopy-energy dispersion x-ray (SEM-EDX) analysis. The samples were provided by Tajima's group.

XAS and RPES measurements at the Fe and Cr $L_{2,3}$ edges were performed at the beamline 2-A of Photon Factory, High-Energy Accelerator Research Organization (KEK). The total electron yield (TEY) method was applied for the XAS measurements. In the RPES measurements, a SCIENTA SES-2002 electron analyzer was used with the energy resolution of $\sim$0.2 eV, respectively. Measurements were carried out in an ultrahigh vacuum of $\sim 8\times10^{-9}$ Pa. The crystals were cleaved *in situ* at a low-temperature of 20 K under the ultrahigh vacuum in order to obtain flesh sample surface. The Fermi Level (E_F) of the samples was calibrated using that of gold.

3.3 Results and discussion

First, in order to clarify the valence of transition metals in Cr-doped Ba122, we carried out XAS measurements. Figure 3.1(a) shows the XAS spectrum at the Fe $L_{2,3}$ absorption edges. The spectrum is very smooth and outstanding multiplet is not found though a tiny shoulder exists on the high energy side of the L_3 absorption peak, which is very similar to the results of Fe metal and Fe in other iron-based superconductors such as $Ca(Fe,Co)_2As_2$. [59, 63, 64] This means that Fe $3d$ electrons are itinerant similar to those in metal, confirming the Fe electronic structure does not change noticeably from that of the parent compound $BaFe_2As_2$ being an itinerant antiferromagnet. The Cr L-edge spectrum is shown in Fig. 3.1(b). The lineshape is smooth as in the case of the Fe or Cr metal [65]. From comparison with

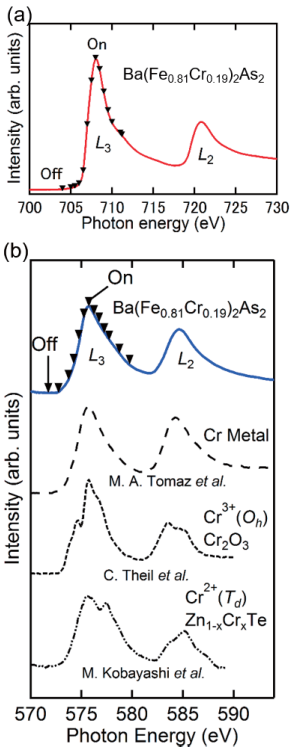

Figure 3.1: X-ray absorption spectra of at the transition-metal $L_{2,3}$ absorption edges of $Ba(Fe_{0.81}Cr_{0.19})_2As_2$. (a) Fe L-edges spectrum. (b) Cr L-edge spectrum in Cr-doped Ba122 compared with those of other compounds.

Cr in Cr_2O_3 [66] and $Zn_{1-x}Cr_xTe$ [67], multiplet seen in these compounds could not be observed in the case of Cr-doped Ba122. These results indicate itinerance of the Cr 3*d* electrons in Cr-doped Ba122. Moreover, the difference from the Cr oxide suggests that sample surfaces were not oxidized and that flesh surface was obtained.

Figure 3.2 shows the photon-energy dependence of the valence-band photoemission spectroscopy (PES) spectra of $Ba(Fe,Cr)_2As_2$. In order to make it easy to see their tendencies, photon energy *vs* electron energy plots and energy distribution curves (EDCs) obtained with using photon energy with the Fe L-edges are displayed in Figs. 3.2 (a) and (d), respectively. Figures. 3.2 (d) and (e) correspond to the Cr L-edges. The spectra in Figs. 3.2(a) and (b) were measured in the photon-energy range of the Fe L_3 absorption edge (708 eV) and subtracted an off-resonance spectrum shown in bottom panel of (b) from the original spectra in order to highlight the enhancement of the intensity. XAS spectrum in the L_3-edge region is also shown in the right panel of (b), where red markers denote photon energies used for the measurements. With varying photon energy, the intensity became higher and a large peak corresponding to normal Auger emission process grew to appear at

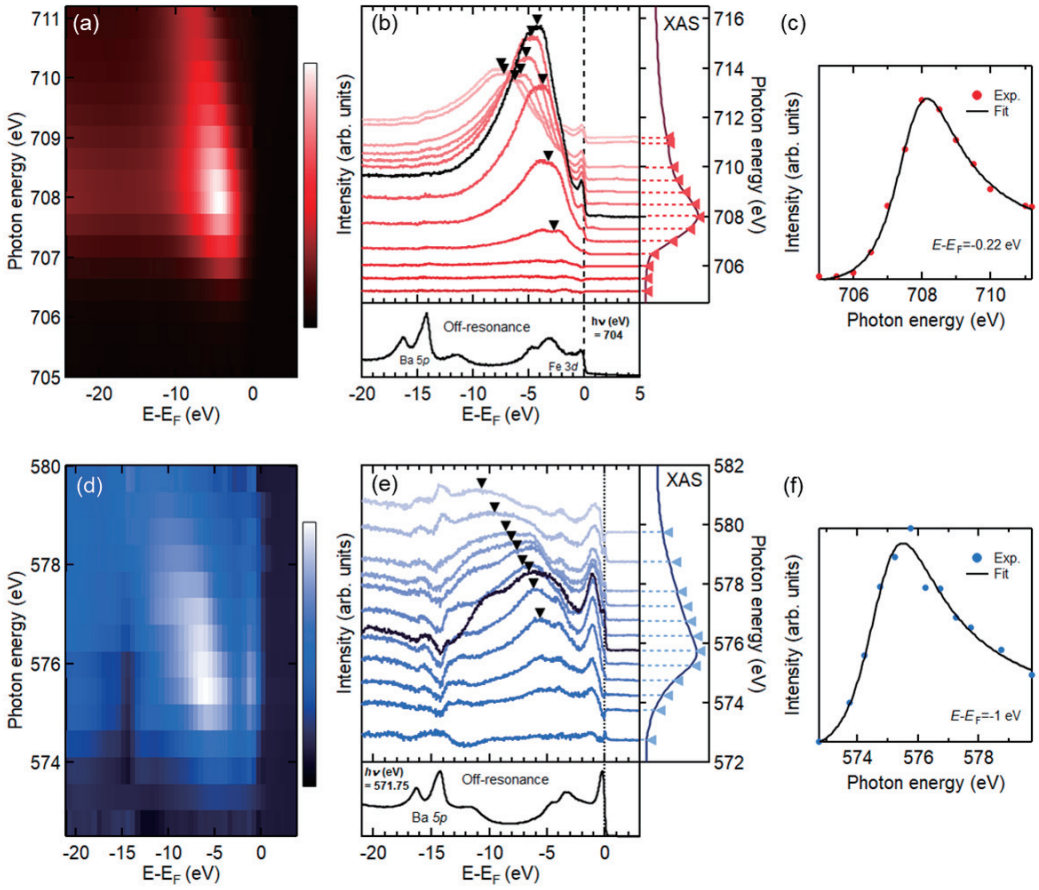

Figure 3.2: Resonant photoemission spectroscopy (RPES) spectra of $Ba(Fe_{0.81}Cr_{0.19})_2As_2$. (a), (b) Evolution of the RPES spectra varying the photon energy in the range of the Fe L_3 absorption edge (Intensity plot and subtracted PES spectra, respectively). Off-resonance PES spectrum shown in the bottom of (b) has been subtracted from the original PES spectra. Intensity plot shown in (a) has been made from the subtracted spectra in (b) with interpolation. XAS spectra around the Fe L_3 absorption edge is shown in the right part of (b). Black curve and inverted-triangle markers indicate the on-resonance PES spectrum and Auger peak positions. (c) Photon-energy dependence of the RPES intensity at a fixed binding energy ($E - E_F \sim -0.2$ eV). The solid line shows a fitting result to Fano line shape. [68] (d), (e), (f) The same as (a), (b), (c) but for the Cr L_3 absorption edge.

$E - E_F \sim -3$ eV. Black markers denote the Auger peak positions. The intensity reaches the maximum around the L_3 absorption edge (708 eV) (the corresponding spectrum is a black line in Fig. 3.2(b)) and diminished gradually, accompanied by a linear peak shift with respect to the photon energy seen as a blight oblique line in Fig. 3.2(a) . Focusing on structures near E_F in detail, one can find enhancement of the small peak near E_F. Moreover, since its position does not depend on the photon energy unlike the normal Auger peak, the structure near E_F can be considered to be specific to Fe 3*d* electron. According to the photon-energy dependence of the RPES intensity at the peak ($E - E_F \sim -3$ eV) (Fig. 3.2(c)), it is obvious that the peak intensity was enhanced near the photon energy of 708 eV and that the line shape can be reproduced by a Fano line shape. [68] The observation of the Auger peak means that photoexcited electrons from core levels are delocalize immediately. In other words, the Fe 3*d* electrons are itinerant. This is consistent with the XAS spectrum. Furthermore, these Fe-related features seen in the spectra are also consistent with previous RPES studies of 122-type Fe-based superconductors. [59, 64] Spectra obtained with varying the photon energy around the Cr L_3 absorption edge (756 eV) are shown in Figs. 3.2(c), (d). General tendency is basically similar to the Fe case. Even in the case of Cr, a bright line which disperse linearly with respects to photon energy was observed as shown in Fig. 3.2(c), indicating appearance of the conventional Auger process. This demonstrates that Cr 3*d* electrons are also itinerant similar to Co in $Ca(Fe,Co)_2As_2$ [64]. However, the Auger peaks in Fig. 3.2(d) are vague and obscured compared to the Fe and Co cases, suggesting that the Cr 3*d* electrons are not so itinerant as that of Fe or Co. Moreover, the Fe Auger peak starts to appear at binding energy of 3.5 eV though the Cr Auger structure is located round 5-6 eV. The difference of ~ 2 eV is considered to arise from the difference between the on-site Coulomb interaction U for Fe and Cr, because the Auger can be thought of as a one-electron-two-hole state. This suggests that the Cr 3*d* electrons are strongly correlated compared to Fe. In the vicinity of E_F, a peak structure at $E - E_F \sim -1$ eV appears and its intensity shows a Fano-like photon energy dependence as shown in Fig. 3.2(f), indicating that the structure derives from the Cr 3*d* state.

Partial density of states (PDOS) deduced from the RPES measurements are shown in Fig.3.3(a). Though the broad Auger peak overlaps with photoemission structures, one can identify peaks near E_F as photoemission peaks for both the Fe and Cr L_3 edges. In both cases, the Fermi edge was observed and the intensity at E_F is finite in contrast to the case of Mn RPES in which the Fermi edge has not been observed. Their metallic characteristics are consistent with the XAS results. Furthermore, they suggest that the transfer of electrons occurs between the Cr and Fe sites, and that Cr substitution introduces holes into the Fe-As plane. Figure 3.3(b) magnifies spectra around E_F. If the Cr 3*d* orbitals are strongly hybridized with Fe

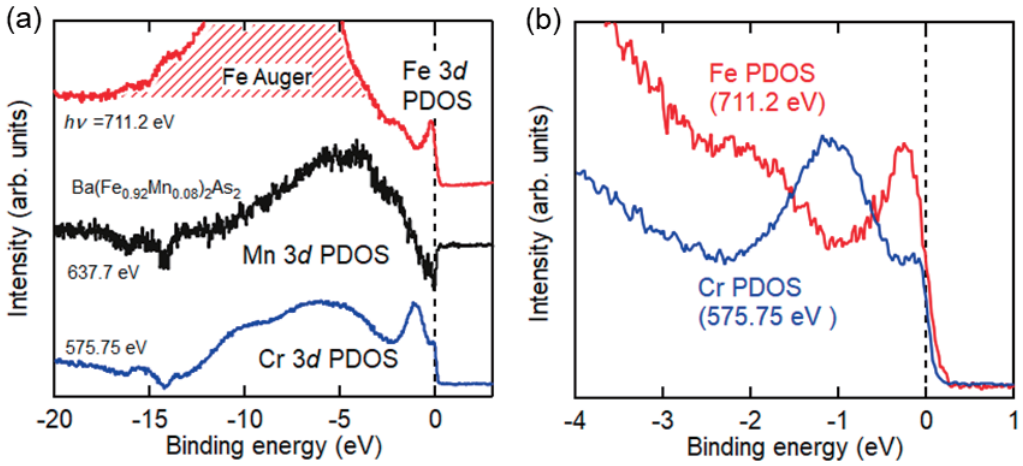

Figure 3.3: Partial density of states in valence band of transition metal atoms. (a) Comparison between 3*d* PDOS of Fe, Mn and Cr. 3*d* PDOS were obtained by subtracting the non-resonant PES spectrum from the on-resonant PES spectrum. Mn PDOS was reprinted from Ref. [69] (b) Expanded 3*d* PDOS near E_F of Fe and Cr. In panel (b), Spectra normalized by their peak height are shown.

3*d* orbitals, the PDOS of Cr and Fe should be similar in lineshape. However, the peak of the Cr PDOS stands at -1 eV below E_F while the main feature is located near E_F similar to Fe in other compounds [59, 70], in the case of Fe. Therefore we consider that the Cr 3*d* orbitals make density of state at E_F but are not strongly mixed with Fe 3*d*. Moreover, the observation of the Cr PDOS deeper than Fe also suggests that Cr 3*d* electrons are more localized than Fe 3*d*, indicating the existence of stronger Coulomb repulsion between the Cr 3*d* electrons. It is considered that this Coulomb repulsion plays an important role in the Hubbard splitting in Mn-doped Ba122. Therefore, we consider effects of the on-site Coulomb repulsion and Hund's coupling as the origin of the shift of Cr PDOS towards the high binding energy side. Assuming that a high spin state is realized for the d^4 configuration of the Cr^{2+} ion, an energy gap between the occupied and unoccupied states is supposed to be $U \quad J$. Taking typical values of $U = 2 \quad 4$ eV and $J = 0.4 \quad 0.8$ eV [71, 72] into account, one can obtain $U \quad J$ of ~ 2 eV, which is comparable to the binding energy of the Cr PDOS. In addition, in the theoretical calculation for $BaCr_2As_2$, the shift of the Cr PDOS towards the high binding energy side with increasing U has been confirmed [12]. Therefore, we concluder that the high spin state ($S = 2$) is realized due to the on-site Coulomb interaction and Hund's exchange in Cr-doped Ba122 similar to Mn-doped Ba122.

For the explanation of the electronic structure of transition-metal elements in the 122 systems, schematic diagrams of the PDOS are shown in Fig. 3.4. The parent

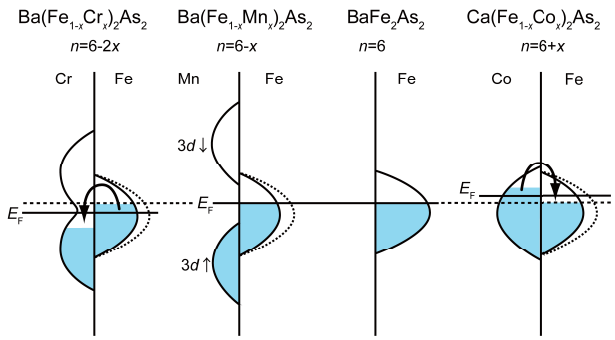

Figure 3.4: Schematic 3*d* PDOS of transition metal in 122-type iron-based superconductors. Horizontal solid lines indicate the Fermi level of each compound. n is the filling of the hybridized Fe/Tm (Tm=Cr, Mn, and Co) 3*d* orbitals.

compound has six 3*d* electrons on at the Fe site. In the case of Co doping, the Fe and Co 3 *d* orbitals compose a band structure near E_F and deliver their charges to each other. Hence the Co substitution introduces electrons into the Fe-As layers significantly and the filling of the hybridized Fe/Co 3*d* band becomes $n = 6 + x$, where x is the Co content in $Ba(Fe_{1-x}Cr_x)_2As_2$. As mentioned in Ref. [59], on the other hand, Mn-doped Ba122 cannot be regarded as a hole-doped system, because 3*d* electrons are localized at the Mn sites and holes are not introduced into the Fe 3*d* band. For d^5 configuration of the Mn^{2+} ion, due to the on-site Coulomb interaction U and exchange interaction J, the up-spin band is fully occupied by five 3*d* electrons and a large magnetic moment of $S = 5/2$ are realized. Therefore, the Mn 3*d* orbitals does not intersect the Fermi level and electrons are not able to transfer between the Fe and Mn sites. Similar to the Mn substitution, the Cr 3*d* electrons form a high spin state due to the strong on-site Coulomb repulsion and Hund's coupling. However, because of the fewer 3*d* electrons than Mn^{2+}, the energy splitting between the minority- and majority-spin states is smaller so that they overlap with each other, and the Cr 3*d* PDOS has spectral weight at E_F. Consequently, Cr can contribute holes to the Fe 3*d* bands. Namely, by the Cr substitution for the Fe atom, holes are injected into Fe orbitals. Thus we considered that the Cr-doped Ba122 is an effectively hole-doped system.

Concerning the missing superconductivity for Cr substitution in spite of the hole doping mentioned above. It is natural that the antiferromagnetic stabilized by the relatively large magnetic moment of Cr is detrimental to the superconductivity. Therefore, the high-spin state induced by the interactions between the Cr 3*d* electrons would give rise to the disappearance of superconductivity in the Cr-doped Ba122.

3.4 Summary

In conclusion, by XAS and RPES, we have studied the electronic structure of Cr and Fe in $Ba(Fe_{0.81}Cr_{0.19})_2As_2$. The Fermi edge has been observed in the Cr 3*d* PDOS and the Cr 3*d* electrons has itinerant features. Therefore, $Ba(Fe_{0.81}Cr_{0.19})_2As_2$ is consider to be an effectively hole-doped system. However, the Cr 3*d* PDOS is mainly located at $\sim$1 eV below E_F indicating the localization of the Cr 3*d* electrons. Then the high-spin state at the Cr site is realized by the on-site Coulomb interaction and Hund's coupling. Similar to the Mn substitution, this high spin state would favor the antiferromagnetism and be detrimental to the superconductivity.

Chapter 4

Angle-resolved photoemission study of hole-doped $Ba(Fe_{1-x}Cr_x)_2As_2$

4.1 Introduction

As introduced in Chapters 1 and 3, Mn or Cr substitutions for Fe cannot induce superconductivity into $BaFe_2As_2$ [18, 43]. In stead of emergence of the superconductivity, checkerboard-type antiferromagnetic (AFM) ordering so called G-type AFM grows after the SDW vanishes, and becomes the ground state of another parent compound $BaCr_2As_2$ [44]. According to electronic transport measurements [18, 43], resistivity for these doped compounds exhibits an anomaly corresponding to phase transition and a gradual upturn basically below magnetic transition temperature T_N in contrast to the parent compound and other superconducting doped compounds [23, 50, 73], indicating Kondo effect [74] or weak-localization effect [59] due to magnetic impurities. So far, nematicity in the iron-based superconductors has been observed as anisotropy of some physical properties [22] and their origin remains controversial. To clarify the origin of the nematicity observed in Fe-based superconductors is one of the main issue that must be resolved in order to understand the relationship between nematicity and superconductivity. The in-plane resistivity anisotropy was discovered in the antiferromagnetic orthorhombic (AFO) phase of Co-doped $BaFe_2As_2$ detwinned under uniaxial pressure because it had been hidden in twinned crystals in the AFO phase [75]. The resistivity along the longer a axis with antiferromagnetic spin alignment (ρ_a) is always smaller than that along the shorter b axis with ferromagnetic spin alignment(ρ_b), which contradicts the double-exchange mechanism. It has been reported that the in-plane resistivity anisotropy is suppressed in single crystals with quality much improved by annealing [22,76]. The report has suggested that the anisotropy in as-grown crystals probably comes from crystal defects present in Fe-As layers. Effects of doping on the AFO phase for the in-plane resistivity have also been investigated systematically by

Ishida *et al* [77]. They have studied the doping evolution and the dopant-site dependence of the in-plane resistivity for $BaFe_2As_2$, and found that the strength of dopant impurity scattering control the suppression of the AFO ordering temperature and the magnitude of the resistivity anisotropy, concluding that the major doping effects are to introduce disorder and that the anisotropy arises from anisotropic impurity state. On the other hand, reversal of the in-plane resistivity anisotropy have been observed in K-doped and Cr-dope $BaFe_2As_2$ [41,47,77,78]. Though ρ_a is smaller than ρ_b in the low concentration region as mentioned above, the anisotropy attenuates with increasing the dopant concentration and eventually changes sign ($\rho_a > \rho_b$) at x=0.09 for Ba($Fe_{1-x}Cr_x$)$_2As_2$. The sign reversal of the in-plane resistivity anisotropy in the hole-doped systems has been predicted by theoretical studies which taking into account the Fermi surface topology [40–42]. The anisotropy of the Drude weight or the scattering rate due to intrinsic electronic structure are considered to give rise to the in-plane resistivity anisotropy. However, for Cr-doped $BaFe_2As_2$, even the Fermi surfaces and the band structure have not been studied experimentally until now. In addition, since the AFM region where negative anisotropy of in-plane resistivity emerges is wide in the phase diagram compered to K-doped $BaFe_2As_2$, we thought Cr-doped $BaFe_2As_2$ is suitable. To clarify the electronic structure and its relationship with the sign reversal of the in-plane resistivity anisotropy, here we provide results of angle-resolved photoemission spectroscopy (ARPES) studies on the Cr-doped $BaFe_2As_2$.

In this study, we report Fermi surfaces and band structure of detwinned Ba($Fe_{1-x}Cr_x$)$_2As_2$ (x=0.06, 0.09 and 0.19) by high-resolutions ARPES. Upon Cr substitution, the Fermi level moves downward reflecting the upward shift of band dispersions without significant changes of dispersion, indicating validity of the rigid-band model and sufficient hole doping with Cr substitution in contrast to Ba($Fe_{1-x}Mn_x$)$_2As_2$, where practically no holes are doped by Mn substitution. Moreover, upon Cr doping, the Fermi surfaces gradually change from that of the parent compound. The elliptical electron pockets, which is considered to dominate the scattering along the b axis, shrink and vanish eventually, consistent with theoretical prediction [42]. Our observation indicates that the changes of the Fermi surface topology play an important role in the sign reversal of the in-plane resistivity anisotropy.

4.2 Experiment

High-quality single crystals of Ba($Fe_{1-x}Cr_x$)$_2As_2$ (x=0.06, 0.09, and 0.19) were provided by Prof. Tajima and Dr. Kobayashi of Osaka Univ.. They were grown by the self-flux method and post-annealed [62]. The compositions of the crystals were determined by scanning electron microscopy-energy dispersion X-ray (SEM-EDX) analysis. ARPES measurements at the Fe and Cr $L_{2,3}$ edges were conducted

at beamline 5-4 of Stanford Synchrotron Radiation Lightsource(SSRL), SLAC National Accelerator Laboratory and beamline 7U of UVSOR, Institute for Molecular Science, using a SCIENTA R4000 electron analyzer and an MB Scientific AB A-1 analyzer, respectively. Linearly polarized light(s, p) and circularly polarized light with energy of ~ 21 eV ($k_z \sim 0$) were used. The crystals were cleaved *in situ* at 15-20 K for low-temperature measurements. Measurements were carried out in an ultrahigh vacuum of $\sim 5.5 \times 10^{-9}$ Pa. In order to eliminate the effects of twinned crystalline, samples are detwinned under uniaxial pressure. The Fermi level (E_F) of the samples was calibrated with that of gold. First principle calculation with density functional theory (DFT) have been done by using a WIEN2k package. The experimental crystal structure in the AFM state of the parent compound $BaFe_2As_2$ in Ref. [3] was used.

4.3 Results and discussion

4.3.1 Angle-resolved photoemission spectroscopy

First, we have investigated electronic structure of $x = 0.19$ samples which is supposed to have the electronic structure sufficiently different from that of the parent compounds, in order to find doping effect upon the electronic structure. Figure 4.1 shows ARPES spectra of $Ba(Fe_{0.81}Cr_{0.19})_2As_2$ in the AFO phase. Since the electronic structure cannot be determined with high precision at high temperature due to temperature broadening, we conducted ARPES measurements at low temperature of 13 K, namely, in the AFM phase. Below the AFM transition at $T_N \sim 60$ K, the Fermi surface is reconstructed by band folding due to the AFM ordering, and then becomes very complicated as reported for the parent compound [28–31]. Even for $Ba(Fe_{0.81}Cr_{0.19})_2As_2$, complicated intensity maps were obtained shown in Figs. 4.1 (a) and (b). At least, it is clear that Fermi surfaces are located around the zone center (Γ) and the zone corner (X/Y) similar to typical iron-based superconductors [80]. However, details of the Fermi surfaces differ from the parent compound in which three hole pockets around Γ and two electron pockets around X/Y exist. For example, in contrast to $BaFe_2As_2$, a tiny bright spot between (Γ) and X, which arises from Dirac point, was broadened and obscured (Fig. 4.1 (a)). For the band structure, Figs. 4.1 (c)-(j) show energy *vs* momentum ($E-k$) plots and their second derivatives along energy axis. They correspond to cuts 1-4 depicted by red arrows in (a), respectively. Around the Γ point (cut 1), the hole-like band is observed although structure was indistinct due to the broad peak width. As it approaches the X point, the hole-like band sinks downward (cut 2 and 3). Around the X point (cut 4), a shallow electron-like band is located just below Fermi level (E_F). For comparison with band dispersion of $BaFe_2As_2$, we have carried out first-principle calculation

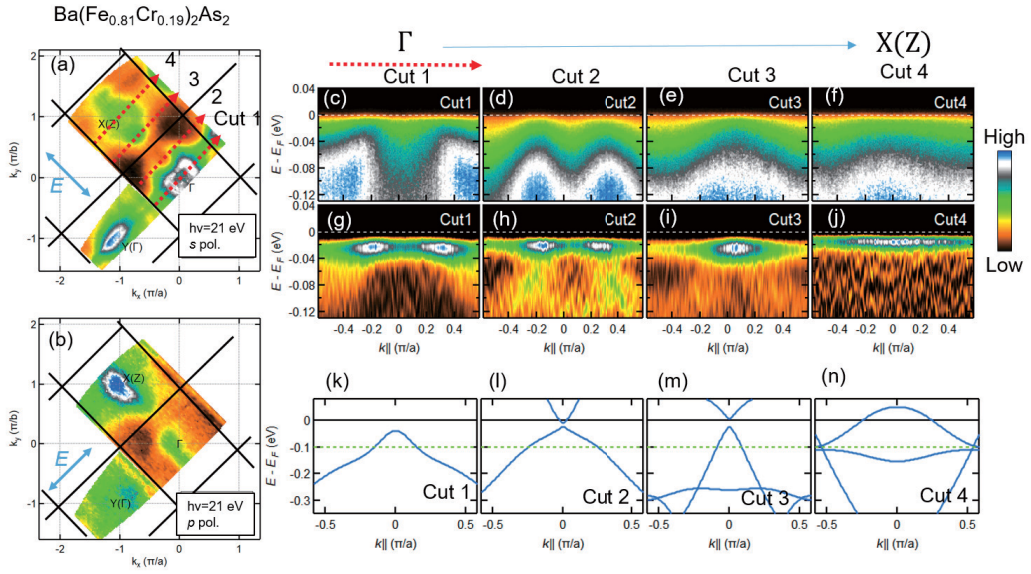

Figure 4.1: ARPES spectra of $Ba(Fe_{0.81}Cr_{0.19})_2As_2$ in the AFO state. (a), (b) ARPES intensity maps at E_F (energy window = $E_F \pm 10$ meV) of $Ba(Fe_{0.81}Cr_{0.19})_2As_2$ using incident light with *s* polarization and *p* polarization, respectively. Black lines indicate the Brillouin zone boundary lines in the AFO state. (c)-(f) ARPES spectra along cuts depicted by red arrows in (a). (g)-(j) Second derivatives of energy distribution curves (EDCs) of (c)-(f), respectively. (k)-(n) Band dispersions of the parent compound $BaFe_2As_2$ in the AFM state predicted by DFT calculation. We used a Wien2k package to calculate them. Each cut corresponds to (c)-(f)), respectively. Green lines corresponds to expected Fermi level of $Ba(Fe_{0.81}Cr_{0.19})_2As_2$.

in density functional theory (DFT) using a Wien2k package the lattice parameters reported in Ref. [3]. Obtained band dispersions are shown in Figs. 4.1 (k)-(n), corresponding to cut 1-4, respectively. Assuming renormalization factor of ∼2-3 due to electron correlation [31], an upward energy shift of 40 meV (0.1 eV for DFT calculation without renormalization) can reproduce the observed band structure. This results suggest that the rigid-band model is valid for $Ba(Fe_{0.81}Cr_{0.19})_2As_2$. In other words, it can be considered that Cr doping does not change the band structure composed of the Fe *3d* orbitals significantly, and that the Cr substitution for the Fe site plays a role of introducing holes into the FeAs layers. Estimating the amount of doped holes by assuming the unchanged density of states of the parent compound, we found that 0.18 holes/f.u. are introduced, which is almost a quarter of expected value of 0.76 holes/f.u. for x=0.19 with divalent Cr. This is consistent with our resonant photoemission results shown in Chap. 3, indicating the Cr 3*d* electrons

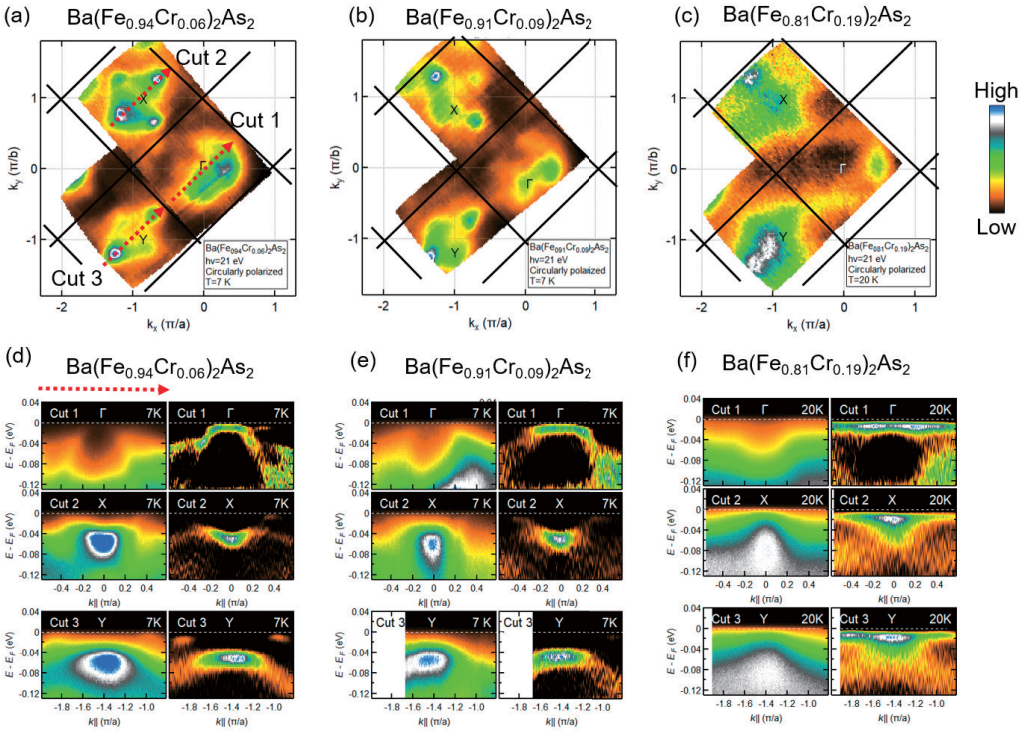

Figure 4.2: Composition evolution of ARPES spectra of $Ba(Fe_{1-x}Cr_x)_2As_2$ (x=0.06, 0.09 and 0.19) in the AFO phase taken using circularly polarized light. (a)-(c) ARPES intensity maps at E_F (energy window = $E_F \pm 10$ meV) of $Ba(Fe_{1-x}Cr_x)_2As_2$ (x=0.06, 0.09 and0.19), respectively. Black lines indicate the Brillouin zone boundary lines in the AFO state. (d) Energy-momentum plots for x=0.06 along cuts depicted by red arrows in (a).(top: Cut1, middle: Cut2, bottom: Cut3) The left column shows raw spectra, and the right column shows the second derivative of the raw spectra. (e), (f) The same as (g) but for x=0.09 and x=0.19, respectively.

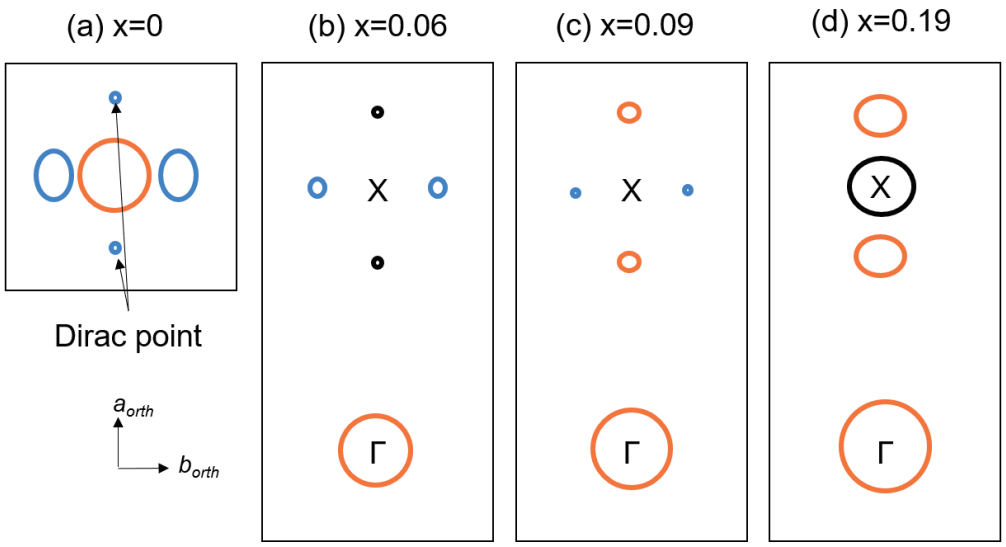

Figure 4.3: Schematic Fermi surfaces for Ba(Fe$_{1-x}$Cr$_x$)$_2$As$_2$ (x=0, 0.06, 0.09 and 0.19) in the AFO phase. (a) Fermi surfaces of the parent BaFe$_2$As$_2$ proposed in Ref. [79]. (b)-(d) Schematic Fermi surfaces of Ba(Fe$_{1-x}$Cr$_x$)$_2$As$_2$ (x=0, 0.06, 0.09 and 0.19, respectively) estimated from the present study. Orange and blue lines indicate hole and electron-like Fermi surfaces, respectively. Black pockets could not be distinguished whether they are hole pockets or electron pockets. The ΓX direction is along the a-axis of the AFO phase.

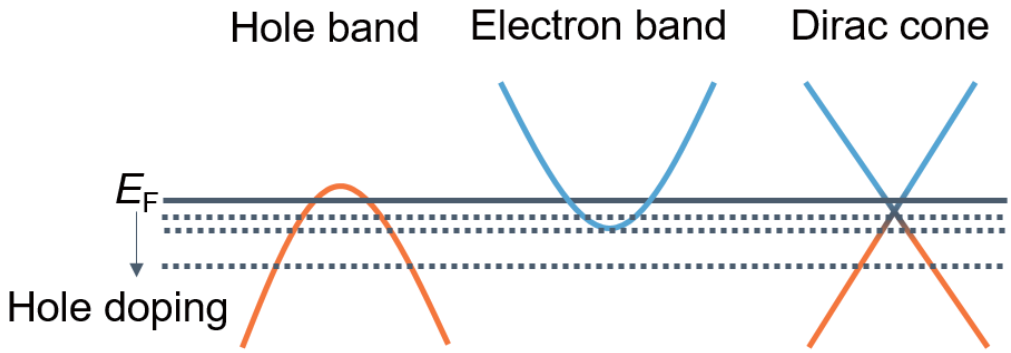

Figure 4.4: Schematic typical band dispersions (hole band, electron band and Dirac cone) with hole doping. For the parent compound, the Dirac point is located near E_F. With hole doping, E_F shifts downward and the Dirac point goes upward. Consequently, the Dirac pocket becomes larger.

partially localized due to on-site Coulomb repulsion and exchange interaction.

We have also conducted ARPES measurements on the $Ba(Fe_{1-x}Cr_x)_2As_2$ having different Cr concentration (x=0.6, 0.9 and 0.19) in order to investigate doping effects on electronic structure of $Ba(Fe_{1-x}Cr_x)_2As_2$. Figure 4.2 shows the doping evolution of the electronic structure. Fermi surface mapping of x=0.6, 0.9 and 0.19 are displayed in Figs. 4.2 (a)-(c), respectively. Although Fermi surfaces are located around Γ and X/Y for all concentrations, the shape of the Fermi surfaces gradually changes with increasing Cr content. For x=0.6, we observed four bright spots around the X point, which are similar to the tiny electron pockets arising from the Dirac-cone like band dispersion in the parent compound. Only two Dirac points along the ΓX direction have been observed around X in $BaFe_2As_2$. [28, 29] The additional two tiny pockets get weaker with increasing x. Moreover, Fermi surfaces around Γ seem to become larger, and intensity at X appears for x=0.19. Schematic Fermi surfaces are summarized in Fig. 4.3. Compared to the parent compound, electron pockets shrink and hole pockets expand gradually with increasing Cr content. These variations are considered to be the consequences of the downward chemical potential shift due to the hole doping as shown in Fig. 4.4. The band structure have also changed systematically. Figures 4.2 (d)-(e) shows $E-k$ plots and their second derivative plots along red arrows in Fig. 4.2 (a) for x=0.06, 0.09 and 0.19, respectively. For x=0.06, in Cut1 crossing the Γ point, hole-like bands appears, and at least one hole band traverses the Fermi level, composing a hole pocket around Γ. Around X and Y, we observed an electron-like band 60 meV below E_F and Dirac-cone-like band dispersions of which crossing points are located near E_F, corresponding to the four tiny Fermi surfaces. As the Cr content increases, most of the band dispersions move upward. Because of this, the distance between two Fermi momenta k_F and $-k_F$ of the hole band around Γ becomes larger, indicating that the hole pocket also becomes larger as seen in the Fermi surface mapping. In addition, it is found that the intensity at X for x=0.19 arises from band bottom of the electron pockets shifted upward. This phenomenon prove that the Fermi level gradually shifts depending on the Cr content.

For more details, we have estimated amount of band shift from peak position of momentum dispersion curves (MDCs). Overlapped peak positions of the hole band around Γ for all compositions are shown in Fig. 4.5 (c). Varying the Fermi level for each Cr concentration, the overlapped bands match each other. Fermi energy shift with respect to E_F for x=0.06 is plotted as a function of Cr content in Fig. 4.5 (d). The Fermi level is lowered linearly with x. According to linear x dependence of the shift, difference in the Fermi level between x=0 and 0.19 is supposed to be 44 meV. This is quantitatively consistent with the value predicted by comparison with the first principle calculation as mentioned above.

Moreover, for confirmation of the Fermi level shift, we have carried out core-

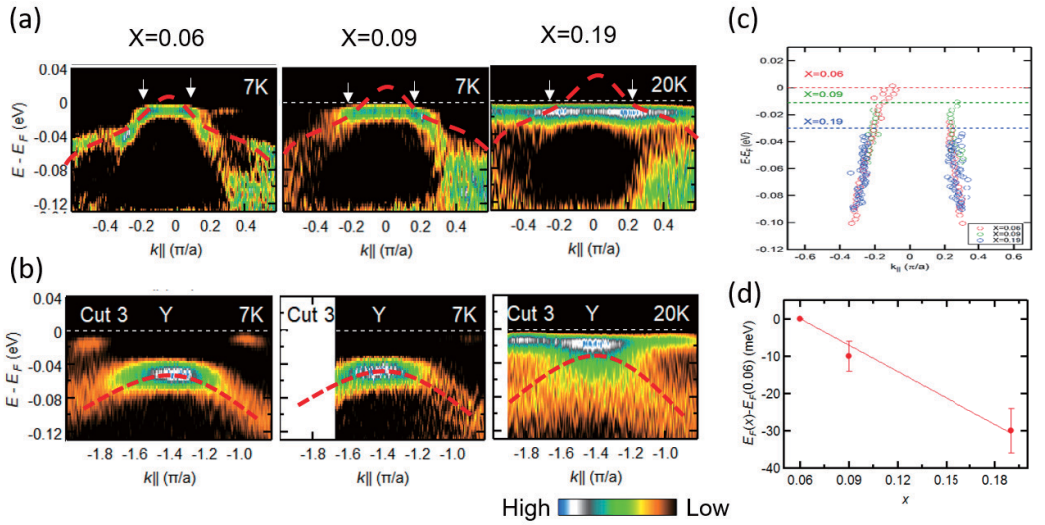

Figure 4.5: Doping dependence of the band dispersions of Ba(Fe$_{1-x}$Cr$_x$)$_2$As$_2$ (x=0.06, 0.09 and 0.19) in the AFO phase. (a), (b) Shift of bands around X and Y, respectively. Hole-like bands gradually move upwards with increasing Cr contents. White arrow indicates Fermi momentum k_F. (c) Doping-dependent dispersion of the hole band at Γ in (a) estimated from the peak positions of momentum dispersion curves (MDCs). The peak positions were obtained by fitting MDC curves by Lorentzian function convoluted with Gaussian. Red, green and blue markers correspond to x=0.06,0.09 and 0.19, respectively. (d) Doping-dependent Fermi-level shift with respect to that of x=0.06.

level x-ray photoemission spectroscopy (XPS). Figures 4.6 (a)-(c) show XPS spectra of the Fe 2p, Ba 3d and As 3d core levels in Ba(Fe$_{1-x}$Cr$_x$)$_2$As$_2$ (x=0, 0.06, 0.09, 0.13 and 0.19), respectively. In Fig. 4.6 (d), edge shifts of each elements are plotted as a function of x. For the As 3d peaks, the edge seems to move to low binding energy with increasing x. However, Fe 2p and Ba 3d edges are shifted to the opposite direction. The change of the binding energy is described by $\delta E_B = \quad \delta\mu + K\delta Q \quad \delta V_M + \delta E_R$, where, μ is the chemical potential, Q is the number of valence electrons, V_M is the Madelung potential and E_R is the extra-atomic relaxation energy of the core-hole. The positive energy shift of Fe 2p is due to the effect of the change in Q because holes are doped into the valence band at Fermi level composed of the Fe 3d orbitals. Moreover, it is reported that Ba peaks exhibit unusual behavior frequently. [81] Thus, the Ba 3d leading edge shift also dose not reflect the chemical potential shift. According to the core-level shift of As 3d edge, chemical potential shift of $\sim$43 eV for x=0.19 was derived, which agree with the value estimated from ARPES measurements.

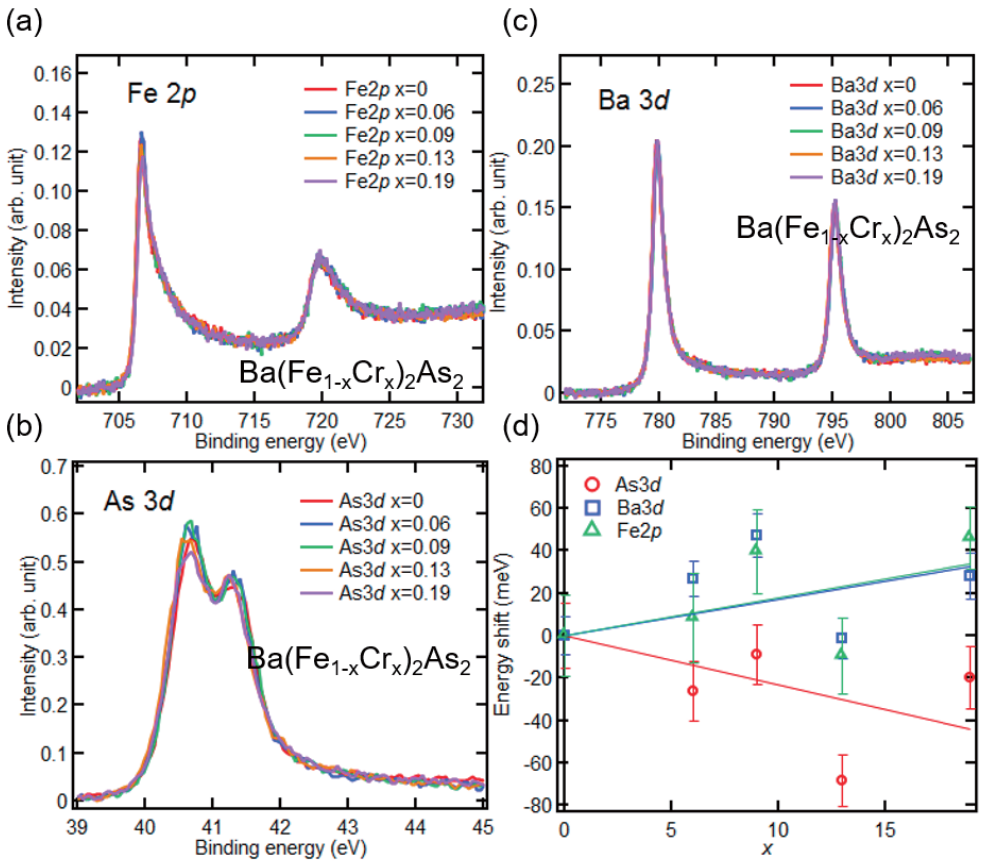

Figure 4.6: Core-level x-ray photoemission spectroscopy (XPS) spectra of $Ba(Fe_{1-x}Cr_x)_2As_2$ (x=0, 0.06, 0.09, 0.13 and 0.19). (a)-(c) Doping evolution of XPS spectra of the Fe 2p, Ba 3d and As 3d core levels, respectively. (d) Doping-dependent edge shifts of Fe 2p, Ba 3d and As 3d. Positive corresponds to shift to higher binding energy.

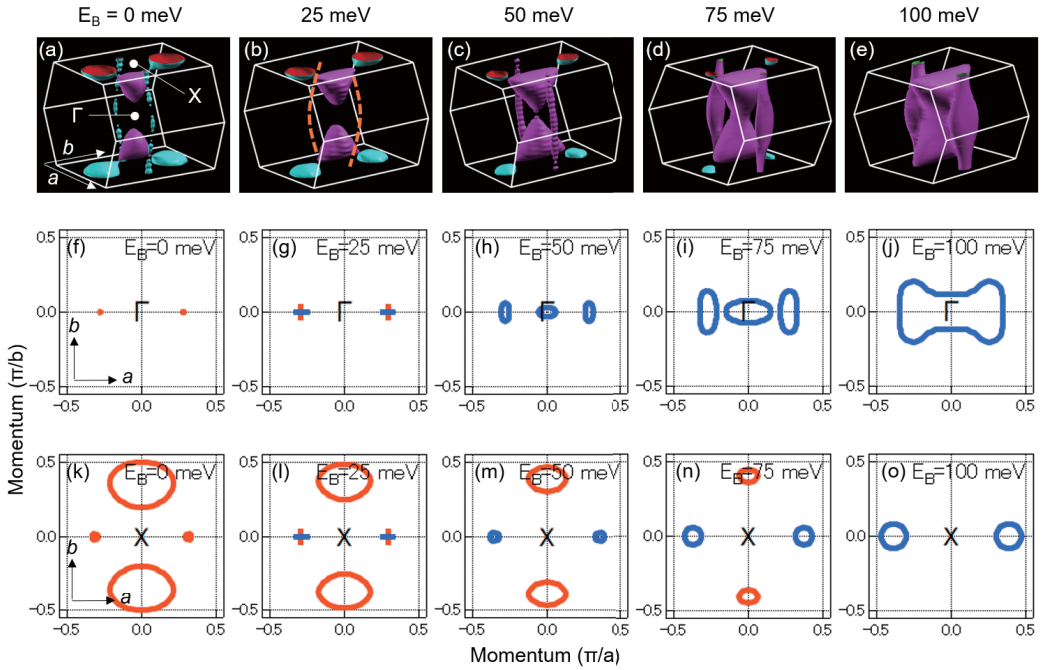

Figure 4.7: DFT calculation results of $BaFe_2As_2$. (a-e) Doping evolution of three dimensional Fermi surfaces with energy shift of 0, 25, 50, 75 and 100 meV, respectively. Taking into account the renormalization factor of 2.5, the energy shift correspond to 0, 10, 20, 30 and 40 meV, respectively. The panel (a) corresponds to the parent compound. (f-j) Doping evolution of in-plane Fermi surfaces at $k_z = 0$ (the Γ point) with energy shift of 0, 25, 50, 75 and 100 meV, respectively. Blue and orange line indicate hole- and electron-type Fermi surfaces, respectively. (k-o) The same as (f-j), but $k_z = 2\pi/c$ (the X point). Block line in (b) and crosses in (g) and (l) indicate the Dirac points, which cannot be depicted due to a small number of momentum points (k-mesh).

In the previous study on the parent compound $BaFe_2As_2$ [29, 82], it have been found that its Fermi surfaces are composed of an hole pocket around the zone center, Dirac-cone-like tiny electron pocket along the $\Gamma - X$ line, and elliptical electron pockets. Upon slight Cr substitution, the elliptical electron pockets around X shrinks and becomes tiny electron pockets similar to the Dirac-cone-like pockets. With increasing Cr content, the tiny pockets becomes weaker for x=0.09 and vanish eventually for x=0.19. As for the Dirac-cone-like tiny electron pockets of the parent compound, upon Cr doping, they expand slowly compared to the change of the elliptical electron pockets, indicating that the Dirac points are located above the Fermi level. Changes of the Fermi surface topology around Γ has been theoretically investigated using the multi-orbital Hubbard model in the AFM phase of 122-type systems [39, 83]. According to the studies, upon hole doping, the elliptical electron pockets along the b axis vanish and the Dirac-cone-like pockets along the a axis expand gradually. Tendency of our results are qualitatively consistent with the theoretical prediction although we could observed clear Fermi surfaces only around the X point. The theoretical study has also attributed the sign change of the in-plane resistivity anisotropy in hole-doped iron-based superconductors to the interplay of impurity scattering and the anisotropic electronic states strongly influenced by the topology of the Fermi surface. Scattering rate of the elliptical electron pockets due to impurity scattering dominates the total scattering rate along the b axis, and the disappearance of the elliptical electron pockets upon hole doping induces the sign change of the scattering rate anisotropy. However, the resistivity anisotropy is not supposed to change its sign because of opposite sign of the Drude weight anisotropy, which also change its sign at electron density $n \sim 5.88$. In reality, the sign change of the in-plane resistivity at the lowest temperature has been observed at x=0.09. Actual electron density n for x=0.09 estimated from comparison between our ARPES results and DFT calculation results is 5.91, which is similar to the theoretical value of $n \sim 5.89$ where the resistivity anisotropy changes sign. However, the observed Fermi surfaces for x=0.06, which consist of two Dirac pockets and two electron pockets, differ from the theory: Theoretical Fermi surface in Ref. [39] has only two Dirac surfaces and a hole pocket. The Γ and X points in the AFM state have been considered to be similar because of two dimensionality of the 122 systems in previous studies [28, 29]. Nevertheless, the Γ and X points are not supposed to be completely the same. Therefore the differences between the experimental Fermi surface around X and theoretical Fermi surface around Γ maybe attributed to k_z dependence of the Fermi surfaces. We have calculated three dimensional Fermi surfaces by assuming a rigid band picture in order to evaluate change of the Fermi surface topology (Fig. 4.7). For the parent compound (Fig. 4.7 (a)), Fermi surfaces are not cylindrical and disperse along k_z. There are hole surfaces between Γ and X (purple), two electron pockets around X (right blue) and two Dirac pockets

(right blue slim cylinders). The slim cylinders composed of Dirac pockets seem to be disconnected along k_z because tiny Fermi surfaces can be overlooked due to a small number of momentum points (k-mesh) for calculation in reality, but they are considered to be connected. Our calculation result is consistent with Fermi surfaces determined by Shubnikov-de Haas (ShdH) oscillations [30]. Varying the Fermi energy downward, the hole pockets expand especially along k_z and become relatively cylindrical. Dirac pockets also expand slightly, maintaining cylindrical structure. On the other hand, the electron pockets around X shrink with hole doping and eventually vanish for the energy shift of 100 meV (40 meV for the renormalization factor of 2.5). Figures 4.7 (f-o) show in-plane Fermi surfaces around Γ and X. One can see expansion of the Dirac pockets and hole pockets around Γ and reduction of electron pockets around X. The calculated Fermi surfaces around X differ from that around Γ and are well consistent with the ARPES results, indicating three dimensionality of electronic structures in the AFM state. However, hole and electron bands around Γ of the parent compound predicted and observed in previous calculation and ARPES studies could not be reproduced by our DFT calculation. Although there are such differences due to the calculation methods, general tendency with hole doping is very similar. Namely, with hole doping, the hole pockets and Dirac pockets become larger, and the electron pockets shrink and eventually vanish, consistent with ARPES result. In the present measurements, we considered that the tendency of Fermi surface topology change with hole doping was observed. Therefore, it is not natural that the changes of the Fermi surface topology upon Cr substitution does not affect the resistivity. Accordingly, we have concluded that the changes of the Fermi surface topology lead to the sign reversal of the in-plane resistivity anisotropy.

4.4 Summary

In conclusion, we have carried out ARPES measurements on Ba(Fe$_{1-x}$Cr$_x$)$_2$As$_2$ (x=0.06, 0.09 and 0.19) in order to investigate the nature of the electronic structure and clarify the mechanism of the sign change of the in-plane resistivity anisotropy. Upon Cr substitution, Fermi level moves downward exhibiting upward band dispersion shift without significant changes of dispersion, indicating sufficient hole doping with the Cr substitution in contrast to the absence of carrier doping in Ba(Fe$_{1-x}$Mn$_x$)$_2$As$_2$. Moreover, the Fermi surface topology changes from that of the parent compound. The elliptical electron pockets considered to dominate the scattering shrink and vanish eventually. The Dirac-cone-like electron pockets becomes hole pockets and expand with Cr contents, consistent with theoretical prediction. We concluded that the changes of the Fermi surface topology play a important role in the sign reversal of the in-plane resistivity anisotropy.

Chapter 5

Fermi surface and band dispersions of Te-annealed 11-type $FeTe_{1-x}Se_x$

5.1 Introduction

11-type iron-based superconductors have the simplest crystal structure in which layers consisting of Fe and chalcogens (e.g. Te, Se) atoms tetrahedrally coordinated each other stack. The parent compound FeTe shows a bi-collinear double-stripe antiferromagnetic (AFM) order with the wave vector of Q=(π /2, π /2), which is distinct from the usual collinear magnetic structure observed in iron pnictide [15, 84]. As tellurium in the parent compound is gradually replaced by selenium, the AFM order is suppressed and superconductivity appears. It has been reported that excess Fe atoms at interstitial sites between the Te/Se layers are harmful to the superconductivity and that the superconductivity is very sensitive to its stoichiometry [85, 86]. Therefore, realizing bulk superconductivity in as-grown samples is very difficult. However, by annealing a specimen in air or in an O_2 atmosphere, the excess Fe atoms are found to be removed, and then bulk superconductivity recover [51, 56, 87, 88]. Moreover, in order to remove the interstitial Fe atoms completely, Koshika *et al.* have also developed an annealing method under tellurium vaper and confirmed its effectiveness [52]. After removing the excess Fe by annealing, superconductivity with the superconducting transition temperature (Tc) of $\sim$10 K is observed in a wide Se-concentration region from x=0.05 up to 0.5 and the maximum Tc of 14.5 K is achieved at $x\sim$ 0.4.

According to a magneto-transport measurements for fully-annealed $FeTe_{1-x}Se_x$ [53, 55], although the Hall coefficient (R_H) of annealed $FeTe_{0.6}Se_{0.4}$ is almost independent of temperature above 50 K, it decreases with decreasing temperature below 50 K and eventually changes their sign from positive to negative around 30 K. Moreover, the magnetic field dependence of the Hall resistivity ρ_{xy} is nonlinear in the low-temperature region below $\sim$ 35 K. Naively thinking, the nonlinear behav-

ior of ρ_{xy} and the sign reversal in R_H are usually attributed to a multiband structure, implying the coexistence of hole- and electron-type carrier and the dominance of electrons in the charge carrier at low temperature in optimally doped samples. The strong temperature dependence with the sign change suggests that band-specific pseudo gaps may exist. On the other hand, for Se-underdoped $FeTe_{0.8}Se_{0.2}$, R_H is always positive and shows an obvious upturn at low temperature similar to the case of the as-grown samples though excess Fe atoms have been removed completely by Te-annealing [53]. Naively, this behavior indicates that contribution to the transport properties dominantly comes from hole carriers in contrast to the optimally doped sample. Therefore, one expects the electronic states to change significantly with varying the Se content perhaps due to effects of chemical pressure from the substituted Se atoms because the Se substitution for Te site should not introduce charge carriers into the system.

In general, 11-type iron-based superconductors such as Fe(Te, Se) are considered to be compensated semimetals. They have hole and electron pockets around the Brillouin zone center (the Γ point) and the corner (the M point), respectively [32, 89]. So far, in some of the FeSe-derived superconductors [34–36], Fermi surface topology distinct from that of the bulk FeSe have been observed. In most cases, the obvious electron pockets persist around the M point but hole-like band dispersion around Γ are located well below the Fermi level and then the hole Fermi surfaces are missing, suggesting that extra electron carriers are somehow provided into the system. Assuming distinct Fermi surfaces even in Te-annealed $FeTe_{1-x}Se_x$, it is not strange that different x's show different charge carrier densities. However, it is not clear whether such simple speculation is valid or not. Therefore, we have performed angle-resolved photoemission spectroscopy (ARPES) measurements on Te-annealed $FeTe_{1-x}Se_x$ (x=0.15, 0.2, 0.3, and 0.4) in order to investigate changes in the electronic structure induced by Se substitution.

5.2 Experiment

High-quality single crystals of $FeTe_{1-x}Se_x$ (x=0.15, 0.2, 0.3, and 0.4) were provided by Prof. Watanabe and Mr. Otsuka of Hirosaki Univ.. They were grown by the Bridgman method [86] and annealed in a tellurium vapor ("Te-anneal") [52] in order to remove excess Fe atoms completely. To check the susceptibility and the Tc, magnetization measurements were carried out by using a Magnetic Property Measurement System-5S (Quantum Design, Co., Ltd.) at Cryogenic Research Center, The University. For the determination of chemical compositions, an electron probe microanalyzer (EPMA) was used. ARPES measurements were performed at the beamline 28A of Photon Factory and the beamline 7U of UVSOR Synchrotron Facility, Institute for Molecular Science, using circularly and linearly polarized light

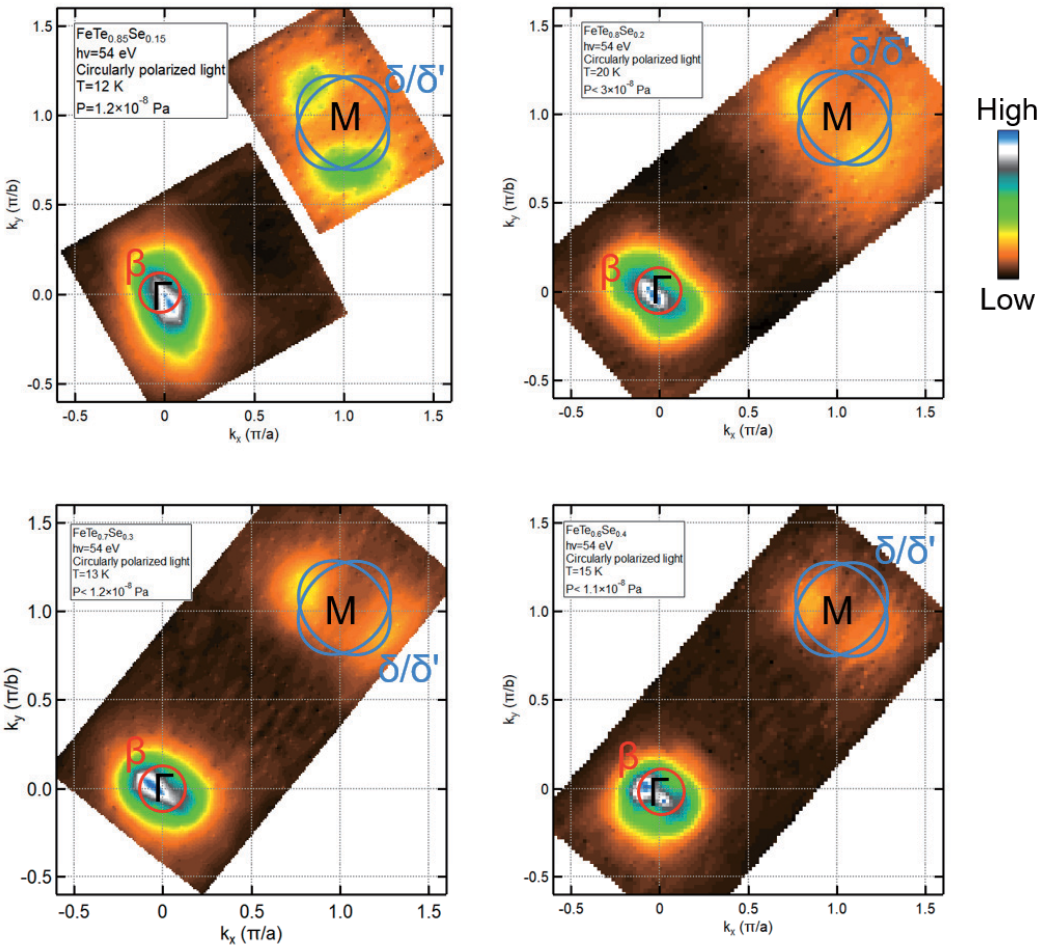

Figure 5.1: Doping evolution of the in-plane Fermi surfaces of Te-annealed $FeTe_{1-x}Se_x$ (x=0.15, 0.2, 0.3 and 0.4). (a)-(d) In-plane intensity mapping at E_F (energy window = $E_F \pm 10$ meV) of x=0.15, 0.2, 0.3 and 0.4, respectively.

with the photon energy of 54 and 22 eV ($k_z \sim 0 and 0.5\pi/c$) with a SCIENTA SES-2002 electron analyzer and an MB Scientific AB A-1 analyzer, respectively. The total energy resolution was $\sim$ 20 and $\sim$ 7 meV, respectively. The crystals were cleaved in situ below a low temperature of 20 K, and the measurements were carried out in an ultrahigh vacuum of $\sim 9 \times 10^{-11}$ Torr. The Fermi level (E_F) of the samples was calibrated using that of gold.

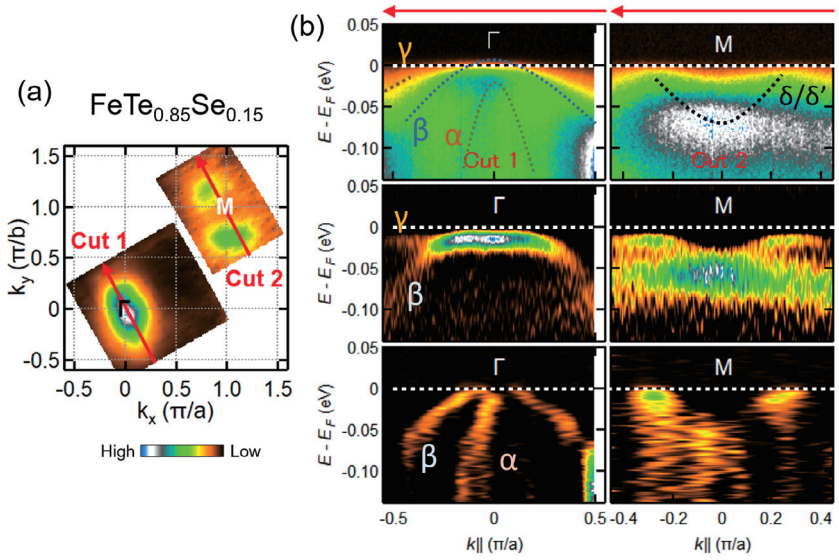

Figure 5.2: ARPES spectra of Te-annealed $FeTe_{0.85}Se_{0.15}$. (a) Fermi surface map reproduced from Fig. 5.1 (a). (b) Energy-Momentum plots and the second derivatives along Cut 1 and Cut 2 depicted by red arrows in (a). Top column: Raw data, Middle: second derivative of EDCs, Bottom: second derivatives of MDCs.

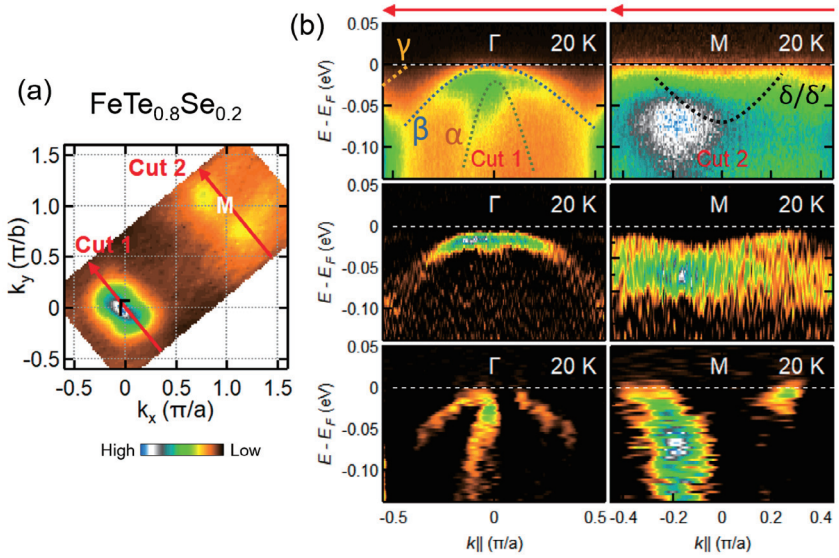

Figure 5.3: ARPES spectra of Te-annealed $FeTe_{0.8}Se_{0.2}$. (a) Fermi surface map reproduced from Fig. 5.1 (a). (b) Energy-Momentum plots and the second derivatives along Cut 1 and Cut 2 depicted by red arrows in (a). Top column: Raw data, Middle: second derivative of EDCs, Bottom: second derivatives of MDCs.

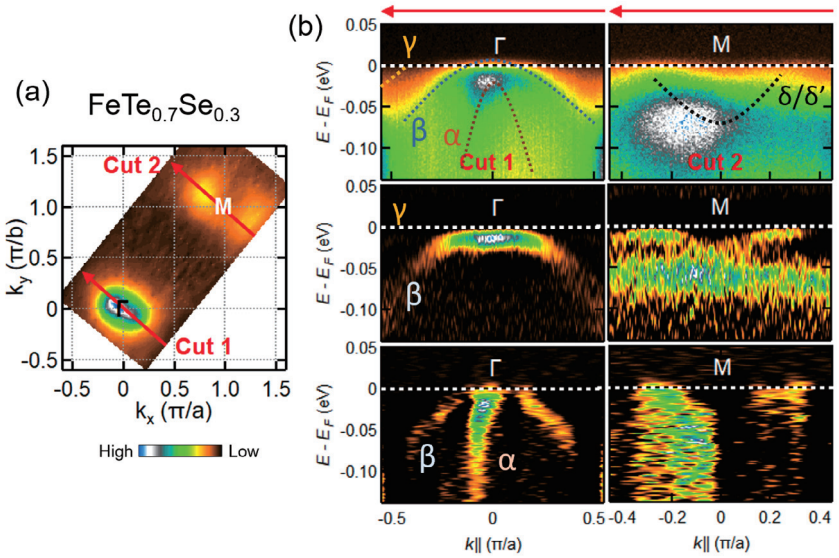

Figure 5.4: ARPES spectra of Te-annealed $FeTe_{0.7}Se_{0.3}$. (a) Fermi surface map reproduced from Fig. 5.1 (a). (b) Energy-Momentum plots and the second derivatives along Cut 1 and Cut 2 depicted by red arrows in (a). Top column: Raw data, Middle: second derivative of EDCs, Bottom: second derivatives of MDCs.

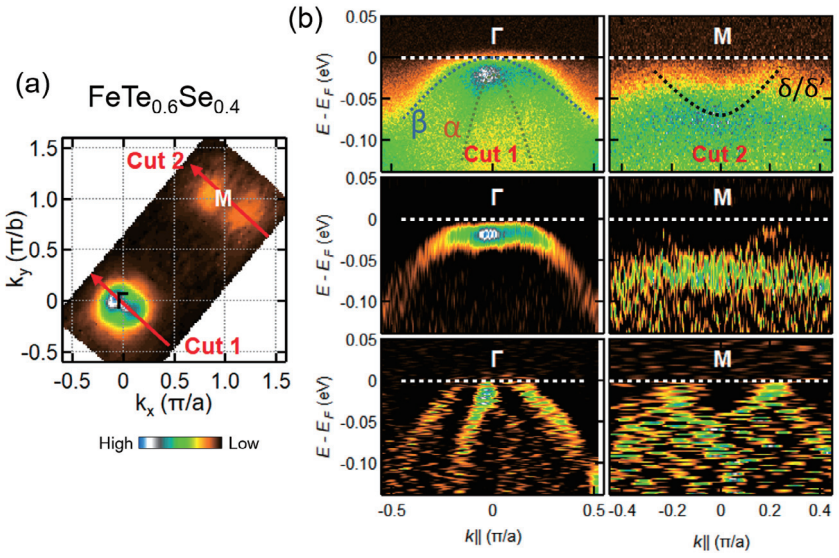

Figure 5.5: ARPES spectra of Te-annealed $FeTe_{0.6}Se_{0.4}$. (a) Fermi surface map reproduced from Fig. 5.1 (a). (b) Energy-Momentum plots and the second derivatives along Cut 1 and Cut 2 depicted by red arrows in (a). Top column: Raw data, Middle: second derivative of EDCs, Bottom: second derivatives of MDCs.

5.3 Results and discussion

5.3.1 Fundamental electronic structure of Te-annealed $FeTe_{1-x}Se_x$

First, in order to investigate doping effect on the Fermi surfaces of Te-annealed $FeTe_{1-x}Se_x$ (x=0.15, 0.2, 0.3 and 0.4), we plotted in-plane intensity map at E_F (energy window = $E_F \pm 10$ meV) of x=0.15, 0.2, 0.3 and 0.4 taken with circularly light polarization in Figs. 5.1 (a)-(d), respectively. In all cases of $0.15 \simeq x \simeq 0.4$, intensities around Γ and M have been observed, and each of them is expected to be assigned to hole pockets and electron pockets, respectively. This is basically similar to the typical Fermi surface of the 11-type iron-based superconductors [32, 89] and previous ARPES results on $FeTe_{1-x}Se_x$ excess Fe atoms are not completely removed [90]. Obvious dramatic changes such as missing of all electron pockets do not seem to occur contrary to that expected from the dramatic changes in the magneto-transport properties.

For comparison of the band structures, we have shown energy-momentum ($E - k$) intensity plots taken along Cut 1 and Cut 2, and their second derivatives along energy or momentum for x=0.15, 0.2, 0.3, and 0.4 in Figs. 5.2 - 5.5, respectively. For x=0.15 (Fig. 5.2), hole bands in Cut 1 around Γ and an electron band in Cut 2 around M were observed, indicating the existence of hole pockets around the zone center and electron pockets around the zone corner as expected. Although three hole bands should be located around Γ according to calculation [32, 91], only two bands (α and β) can be clearly recognized and the third heavy band (γ) considered to be composed of d_{xy} orbital is difficult to detect. Taking second derivatives of the energy distribution curves (EDCs) allows us to recognize the presence of the γ band. That is because the d_{xy} orbital usually has smaller matrix elements compared to d_{yz} and d_{xz} [58]. In addition, we have observed only one electron band (δ) around the M point within the energy and momentum resolution of our measurements, consistent with other previous ARPES measurement of as-grown $FeTe_{1-x}Se_x$ [90]. As the Se content increases, spectral weight distribution does not change significantly. In all cases, the α hole-, β hole-, and δ electron-bands were clearly observed. The heavy γ band can also be recognized in the second derivative as mentioned above. We could not identify differences between the different x's at a glance. In order to compare the band dispersions in more detail, we have plotted peak positions of momentum distribution curves (MDCs) for all the compositions obtained by fitting in Fig. 5.6. Figures 5.6 (a) and (b) correspond to Cut 1 and Cut 2 in Figs. 5.2 - 5.5, respectively. Around the Γ point, the α and β could be defined clearly by MDC peaks. The γ hole band cannot be recognized because it is hard to detect less dispersive heavy bands in MDC in addition to weak intensity of the d_{xy} band. Compared to the band structure for x=0.15, one cannot identify any significant differences induced by the varied Se content. On the other hand, around the M point, one might point

out that the Fermi momentum k_F of the electron band seems to show a weak but systematic change that the electron pocket shrink with increasing x. This suggests that the electron-type carrier density decreases with increasing Se in contrast to the Hall resistivity measurements, indicating an opposite trend. Therefore, we cannot attribute the change of the dominant charge carrier to this slight shift of the electron pocket.

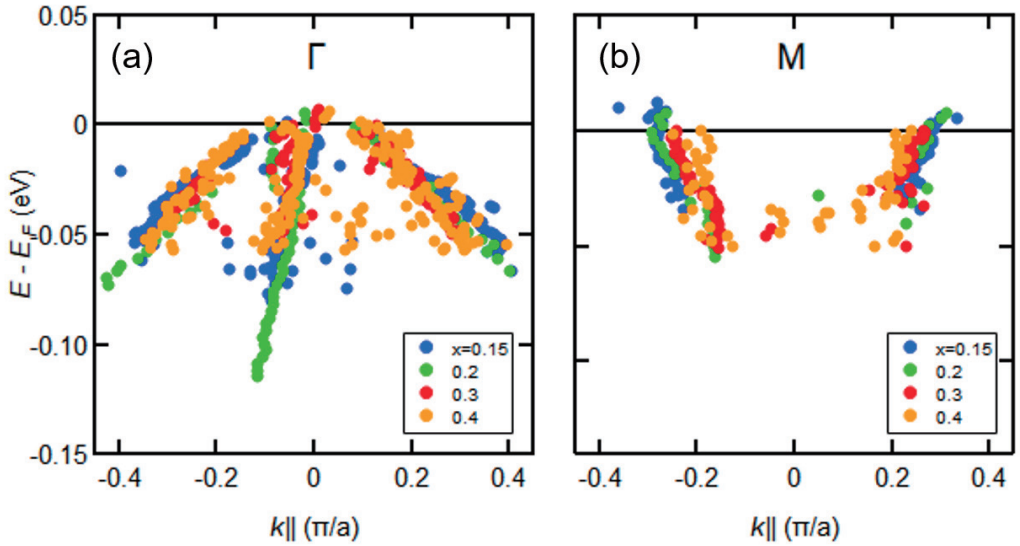

Figure 5.6: Se-doping evolution of the band dispersion of Te-annealed $FeTe_{1-x}Se_x$ obtained by fitting MDCs. (a) Hole-like band dispersions around the Γ point. (α and β) can be defined well. Blue, green, red and orange markers indicate x=0.15, 0.2, 0.3, and 0.4, respectively. (b) Electron band around M.

5.3.2 Polarization dependence of ARPES of $FeTe_{1-x}Se_x$

There is still a possibility that the d_{xy} orbital, which was difficult to detect due to the small matrix element compared to the d_{xz} or d_{yz} orbitals with respect to circularly polarized light, changes with Se doping. One can detect band dispersions having specific orbital character by using linearly polarized light because of polarization sensitivity of matrix elements. Therefore, we have also conducted polarization dependent ARPES measurements to investigate the band dispersions separately. Figure 5.7 shows the in-plane intensity plots at E_F and energy-momentum plots of x=0.2 taken by using $s-$polarized and $p-$polarized photons. One can recognize that the observed bands are different at a glance. In the case of s polarization, two hole-like bands (β and γ) around Γ and an electron band (δ) around M can be observed. On the other hand, for p polarization, one rapid hole-like band (α) around

Γ and similar electron band (defined as δ') around M are observed. As expected, one can identify the γ band unlike the case of circularly polarization. For our experimental geometry in which the analyzer slit is along the $\Gamma - M$ (Fe-Fe) direction, the initial state being odd (even) could be only observed for s (p) polarization basically. Namely, the d_{xy} and d_{yz} orbitals and the d_{xz}, $d_{x^2-y^2}$ and d_{z^2} orbitals could be detected in the s and p geometries, respectively. Taking that into account, we assign α, β and γ to the d_{xz}, d_{yz} and d_{xy} bands, resistivity, which is consistent with previous band calculation [79, 91]. For electron bands around M, according to DFT calculation, they are considered to consists of d_{yz} and d_{xy}. At the zone corner, the matrix element of the d_{xy} band is finite even in the p geometry [58]. That is why the electron pockets were observed for both geometries. Consequently, we have considered that the δ band mainly arises from d_{yz} and that the δ' band has the d_{xy} orbital character. Since both bands are similar to each other, we could not distinguish them in the case of circularly polarization. For comparison with optimally doped x=0.4, Fig. 5.8 shows in-plane intensity plots at E_F and $E - k$ plots of x=0.4. As one can see, they exhibit polarization dependence of band structure similar to that of x=0.2. Therefore, the assigned orbital characters are considered to be the same. One difference from x=0.2 is the position of the γ band. In the case of low Se concentration, the γ band crosses the Fermi level as shown in Fig. 5.7 (b). However, in the case of the optimally-doped sample, the γ band is located $\sim$ 10 meV below E_F, and then it does not form hole fermi surface. In addition, δ/δ' electron bands also seem to change their effective mass. The electron band in the Se-underdoped compound is shallow as shown in second derivative of EDC in Fig. 5.7 (b). Compared to that, for the optimally doped compound, the δ/δ' bands seem to be deeper and have lighter mass. This might correspond to the slight shift of the electron bands observed with circularly polarization as mentioned above. The heavier effective mass of the electron band of x=0.2 suggests less contribution of electron carriers in x=0.2 to electronic transport, which is consistent with results of magneto-transport measurement.

We have plotted the Fermi surfaces determined from the present ARPES measurements in the in-plane intensity plots (Figs 5.7 (a) and 5.8 (a)). The electron pockets are depicted by one ellipse because the electron pockets from δ and δ' were too similar to distinguish them. In addition, since it was difficult to distinguish whether the top of the α band reach the Fermi level or not, a possible tiny hole pocket of α is ignored. The Fermi surfaces was obtained by fitting k_F positions with assuming four-fold rotational symmetry. For x=0.4, a hole Fermi surface β and two electron pockets δ/δ' are define. For low Se concentration, in addition to these Fermi surfaces, a large hole pocket γ is depicted, corresponding to the shift of the γ band with respect to the Se concentration. Now we discuss the charge carrier concentration of these compound which is estimated from the area enclosed by

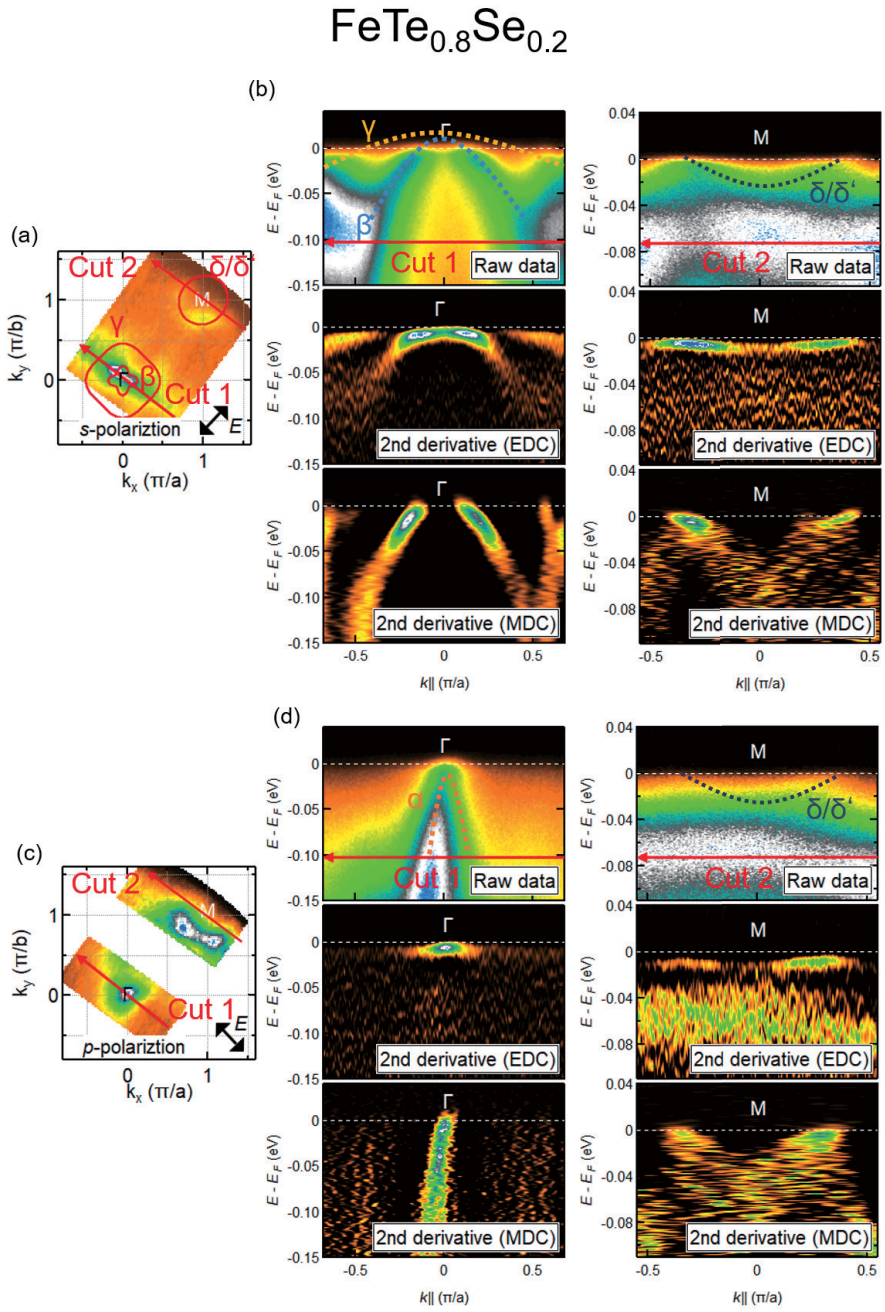

Figure 5.7: Polarization evolution of the band dispersions of Te-annealed $FeTe_{0.8}Se_{0.2}$ (a) In-plain intensity plot at E_F (energy window = $E_F \pm 10$ meV) taken with *s* polarized photon (b) ARPES spectra taken with *s* polarized photon. Top, middle and bottom panels of left column in (b) correspond to an intensity plot around the Γ point and the second derivatives along EDCs or MDCs, respectively. Top, middle and bottom panels of right column in (b) correspond to an intensity plot around the *M* point and second derivative along EDC or MDC, respectively. (c) The same as (a) but for *p* polarization. (d) The same as (a) but for *p* polarization.

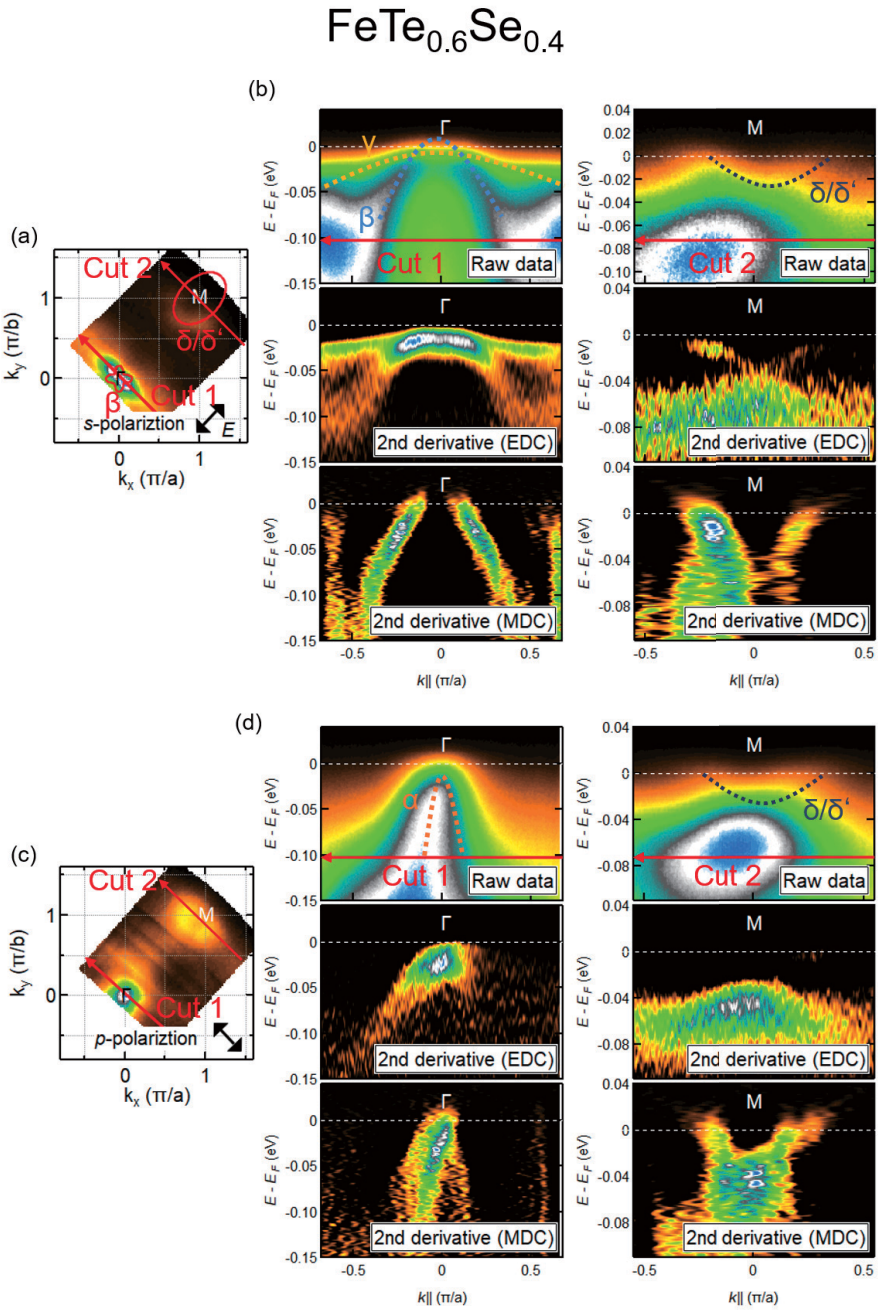

Figure 5.8: Polarization evolution of the band dispersions of Te-annealed $FeTe_{0.6}Se_{0.4}$ (a) In-plain intensity plot at E_F (energy window = $E_F \pm 10$ meV) taken with *s* polarized photon (b) ARPES spectra taken with *s* polarized photon. Top, middle and bottom panels of left column in (b) correspond to an intensity plot around the Γ point and the second derivatives along EDCs or MDCs, respectively. Top, middle and bottom panels of right column in (b) correspond to an intensity plot around the *M* point and second derivative along EDC or MDC, respectively. (c) The same as (a) but for *p* polarization. (d) The same as (a) but for *p* polarization.

the Fermi surfaces assuming Luttinger's theorem [92]. Assuming cylindrical Fermi surfaces of two-dimensional systems, for the optimally-doped sample, charge carrier concentration estimated from the β hole pocket and δ/δ' electron pockets are 0.03 holes/unit cell and 0.15 electrons/unit cell, respectively. By summing up the carrier concentrations with opposite signs, the total carrier concentration was estimated to be 0.27 electrons/unit cell. In the case of the Se-underdoped sample, β, γ and δ/δ' exhibit 0.04 holes/unit cell, 0.3 holes/unit cell and 0.15 electrons/unit cell, indicating the total carrier concentration of 0.04 holes/unit cell. This suggests that the electron-like charge carriers exist dominantly in the optimally doped compound although the hole-type carrier concentration is comparable or predominant in the Se-underdoped compound, which is quantitatively consistent with the sign reversal of the Hall coefficient.

Table 5.1: Electron density estimated from Fermi surface area

	x=0.2	x=0.4
α FS (d_{xz}&d_{yz})	-	-
β FS (d_{xz}&d_{yz})	0.04 hole/u. c.	0.03 hole/u. c.
γ FS (d_{xy})	0.3 hole/u. c.	-
δ/δ' FSs (d_{xz}&d_{yz}/d_{xy})	0.15 electron/u.c.	0.15 electron/u.c.
total area	0.04 hole/u. c.	0.27 electron/u. c.

For more qualitative discussion, we have estimated Hall coefficients for each compound by using parameters obtained from the present ARPES spectra. In order to obtain an expression of R_H in multi-band systems, we have adopted a classical model in which an isotropic Fermi sphere is assumed, because a mathematical expression of R_H in two dimensional systems is unknown. So far, analyses with the classical two-band model (electron- and hole-type bands) have been applied for two dimensional systems such as iron-based superconductors [46, 93, 94]. The Hall coefficient with the two-band model is given by

$$R_H = \frac{1}{e}\frac{(\mu_h^2 n_h - \mu_e^2 n_e) + (\mu_h\mu_e)^2 B^2(\mu_h - \mu_e)}{(\mu_h n_h - \mu_e n_e)^2 + (\mu_h\mu_e)^2 B^2(\mu_h - \mu_e)^2}, \tag{5.1}$$

where n_h (n_e) is hole (electron) density, μ_h (μ_e) is hole (electron) mobility, B is a magnetic flux density, and e is the elementary electric charge. Similar to the two-band model, assuming that the external magnetic field is quite small, R_H in multi-band model is given by

$$R_H = \frac{1}{e}\frac{(\sum_i \mu_{hi}^2 n_{hi} - \sum_j \mu_{ej}^2 n_{ej})}{(\sum_i \mu_{hi} n_{hi} - \sum_j \mu_{ej} n_{ej})^2}, \tag{5.2}$$

where i and j are labels of hole- and electron-type bands, respectively. Moreover, $\mu_{hi} = e\tau_{hi}/m^*_{hi} = el_{hi}/m^*_{hi}v_{hi}$, where τ is a relaxation time, m^* is an effective mass of

quasiparticles, l is a mean-free path, and v is a group velocity. Especially, m^* and v can be obtained from band dispersions observed by ARPES, and l corresponds to a reciprocal of a MDC peak width. To simplify the issue, we took only electrons and holes at Fermi level into consideration and we used experimental values obtained by fitting. Substituting experimental values, we obtained R_H of $1.7 \times 10^{-9} m^3/C$ for x=0.2 and $-1.3 \times 10^{-9} m^3/C$, consistent with the sign reversal of R_H observed in the magneto-transport measurements.

However, the fact that only the γ hole pocket disappears for x=0.4 although other pockets do not drastically change indicates deviation from compensated semimetals. Se substitution into the Te site is not supposed to introduce any carriers because it is considered to be an isovalent substitution. One of possible reasons why electron density seems to change with Se doping is because three dimensionality of Fermi surfaces. Recent band calculation for $FeTe_{0.5}Se_{0.5}$ and ARPES results have suggested that two bands around Γ composed of the Fe d_{xz} orbital and the Te/Se p_z orbital disperse largely along the k_z direction, forming a tiny Fermi surface centered at Γ [95]. If Fermi surfaces disperse along k_z so that total electron density in Brillouin zone is constant with Se concentration, differences in the effective mass and Fermi velocity due to slight changes of band structure might be attributed to the sign reversal of the Hall coefficient. According to comparison between DFT calculations for two parent compounds TeSe and FeTe [32], FeTe has large hole and electron Fermi surfaces depending on k_z strongly compered to FeSe. Therefore, it is natural that in-plane Fermi surface for x=0.2 differs from that of x=0.4. However, we have to note that the d_{xy} orbital usually has strong two dimensionality compared to other bands and that observed band dispersions of each compound for different $k_z(\sim 0 and 0.5\pi/c)$ seem to be similar, which is not consistent with strong k_z dependence keeping the system a compensated semimetal. Other possibility is that electrons are doped with Se doping in reality for some reasons. The conceivable reasons is because real composition ratio deviates from an ideal value. The excess Fe with near Fe^+ will provide electron doping into Fe-chalcogen layers. However, since the excess Fe should be removed by Te annealing, it might be difficult to interpret the large electron doping of 0.27 electrons/unit cell as effects of slight excess Fe. Even if the composition ratio is not the ideal value, it would be natural to think that the change of Fermi surface topology is related to the sign reversal of R_H. Although $FeTe_{1-x}Se_x$ has been claimed to be a compensated semimetal, even in previous ARPES measurements for $Fe_{1+y}Te_{1-x}Se_x$ [79, 89, 90, 96], the γ hole pocket appears and disappears, which depends on the reports. The number of electron surfaces (one or two) around M also depends on the reports. However, somehow they have claimed that the system is the compensated semimetal. These results have made situation more complicated and there are not good explanations of shift of the d_{xy} orbital until now. This problem is still highly controversial.

5.4 Summary

In conclusion, in order to investigate the nature of the electronic structure of $FeTe_{1-x}Se_x$ excess Fe ions are completely removed compound and clarify the Se-concentration evolution of the band structure, we have carried out ARPES measurements of Te-annealed $FeTe_{1-x}Se_x$ (x=0.15, 0.2, 0.3 and 0.4). Upon increasing Se content, the γ band shifts downward and induces disappearance of the outer large hole pockets around the Γ point. In addition, the shallow electron band becomes to deeper, indicating the weakening of the band renormalization factor. These change in Fermi surface topology and band dispersion can explain the sign reversal of the Hall coefficient between Se-underdoped and optimally-doped compounds. The results indicate that the changes of the Fermi topology and mass renormalization may play a important role in the sign reversal of the Hall coefficient.

Chapter 6

Temperature evolution of the electronic states of Te-annealed 11-type $FeTe_{1-x}Se_x$

6.1 Introduction

As introduced in Chap. 5, the 11-type iron-based superconductor $FeTe_{1-x}Se_x$ has been studied to investigate the unconventional superconductivity in recent few years. So far, as-grown or O_2-annealed compounds, in which harmful excess Fe atoms at interstitial sites] might not be completely removed, have been studied. In order to remove the interstitial Fe atoms completely, a new annealing method under tellurium vaper (Te-anneal) has been developed and its validity has been confirmed by Koshika *et al.* [52]. In the preceding chapter, we have presented angle-resolved photoemission spectroscopy (ARPES) measurements results on the Te-annealed 11-type iron-based superconductor $FeTe_{1-x}Se_x$ at low temperature comparable to superconducting transition temperature Tc. We found that the energy band consisting of the d_{xy} orbital shifts upward with Se concentration, leading to the disappearance of the large hole band between x=0.2 and 0.4. The present results are qualitatively consistent with the results of magneto-transport measurements, which suggests that electron charge carriers are dominant in the optimally doped compound (x=0.4) though the hole carriers exist dominantly in Se-underdoped compound (x=0.2). Interestingly, they exhibit different temperatures of Hall coefficient R_H from each other. In optimally-doped sample, a negative R_H at low temperature approaches zero with heating and change its sign from negative to positive around 30 K, exhibiting a peak at 50 K. In the temperature region from 100 K up to 300 K, R_H is almost independent of temperature. On the other hand, for Se-underdoped compound, a positive R_H at low temperature decreases monotonically with increasing temperature up to 100 K. Above 100 K, R_H does not show obvious temperature dependence

similar to optimally-doped compound. Similar behaviors were observed even in O_2-annealed compound. However, mechanism of these non-trivial phenomena is still unknown. For some iron chalcogenides, temperature dependent ARPES measurements have been performed by M.Yi *et al.* [96]. They showed the temperature evolution of a hole band around the Γ point of as-grown optimally doped $FeTe_{1-x}Se_x$, indicating the disappearance of the d_{xy} band with increasing temperature. They proposed an universal orbital-selective strong electron correlations that are insensitive to the Fermi surface topology in iron chalcogenides. In the Te-annealed optimally-doped compound, the d_{xy} orbital does not make Fermi surface as shown in Chap. 5 and might not change the Fermi surface topology even if it disappears with heating. Therefore, the temperature dependent hole Fermi surfaces cannot explain the non-trivial temperature dependence of R_H. Moreover, the temperature dependence of the electron bands of $FeTe_{1-x}Se_x$ have not been studied until now. Therefore, in order to clarify temperature evolution of the electronic state mainly at the zone corner in Te-annealed $FeTe_{1-x}Se_x$, we have conducted ARPES measurements on optimally doped and low Se-doped compounds (x=0.4 and 0.2) varying temperature from temperature around Tc to $\sim 200K$.

6.2 Experiment

High-quality single crystals of $FeTe_{1-x}Se_x$ (x=0.2 and 0.4) were provided by Prof. Watanabe and Mr. Otsuka of Hirosaki Univ.. They were grown by the Bridgman method [86] and annealed in a tellurium vapor (" Te-anneal ") [52] in order to remove excess Fe atoms completely. To check the susceptibility and the Tc, magnetization measurements were carried out by using a Magnetic Property Measurement System-5S (Quantum Design, Co., Ltd.) at Cryogenic Research Center, The University. For the determination of chemical composition, an electron probe microanalyzer (EPMA) was used. ARPES measurements were performed at beamline 28A of Photon Factory, using circularly polarized light with the photon energy of 54 eV with a SCIENTA SES-2002 electron analyzer. The total energy resolution was $\sim$ 16 meV, respectively. The crystals were cleaved in situ below T = 10 K, and the measurements were carried out in an ultrahigh vacuum of $\sim 9 \times 10^{-11}$ Torr. The Fermi Level (E_F) of the samples was calibrated using that of gold.

6.3 Results and discussion

Figure 6.1 shows temperature evolution of the electron band around the zone corner of Te-annealed $FeTe_{1-x}Se_x$ (x=0.2 and 0.4) from $\sim$ 10 K up to $\sim$ 200 K. The cuts are along the red arrow in Figs. 6.1 (a) and (d). Intensity plots are shown in

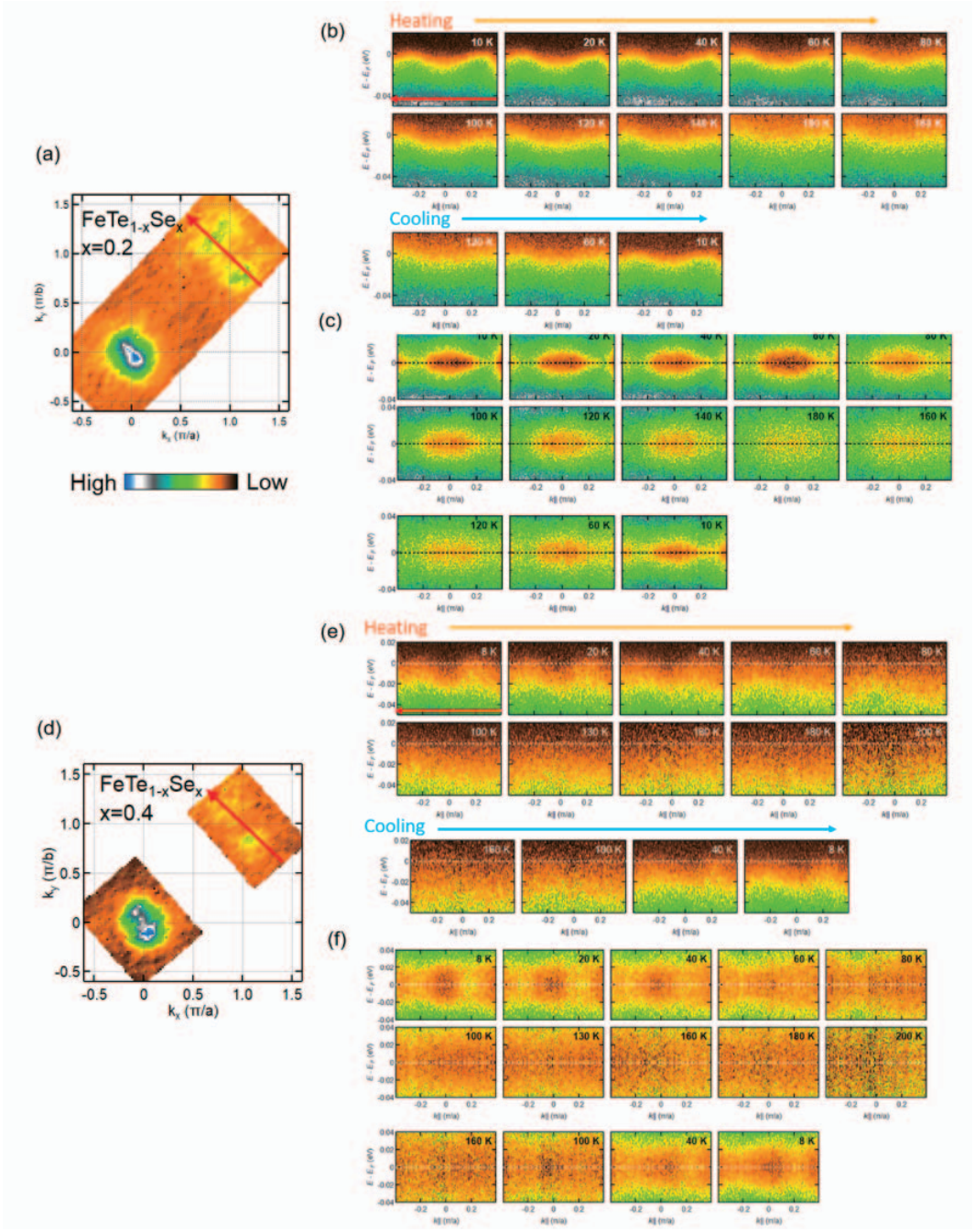

Figure 6.1: Temperature evolution of the electron band around the zone corner of Te-annealed $FeTe_{1-x}Se_x$ (x=0.2 and 0.4). (a) In-plane Fermi surface of x=0.2. (b), (c) Temperature evolution of the energy-momentum plots around M and those symmetrized with respects to Fermi level to highlight Fermi momentum positions, respectively. (d), (e), (f) The same as (a), (b) and (c) for x=0.4, respectively. Cuts are along red arrows in (a) and (d).

Figs. 6.1 (b) and (e). One can see that the electron band is broadened and indistinct with increasing temperature due to the temperature broadening. Assuming a symmetric single-particle spectral function with respects to E_F in the small energy region around E_F ($A(k,\omega) = A(k,-\omega)$), the effect of Fermi-Dirac distribution can be eliminated by symmetrizing the energy distribution curves (EDCs) as follows:

$$\begin{aligned} I(k,\omega)+I(k,-\omega) &= I_0A(k,\omega)f(\omega)+I_0A(k,-\omega)f(-\omega) \\ &= I_0A(k,\omega)[f(\omega)+f(-\omega)] \\ &= I_0A(k,\omega)[\frac{1}{e^{\omega/k_BT}+1}+\frac{1}{e^{-\omega/k_BT}+1}] \\ &= I_0A(k,\omega), \end{aligned} \tag{6.1}$$

where $I(k,\omega)$ is the ARPES intensity, I_0 is a constant factor, $A(k,\omega)$ is the spectral function, and $f(\omega)$ is the Fermi-Dirac function. To highlight k_F positions, the ARPES spectra symmetrized along the energy direction with respects to E_F are shown in Figs. 6.1 (c) and (f). Interestingly, in the case of x=0.2, distance between the different k_F's seems to expand with increasing temperature, suggesting the expansion of the electron pocket. For x=0.4, as temperature increases, spectral wight is weakened and eventually disappears. One may consider the possibility of electron doping or impurity scattering on the sample surface due to contamination of the sample surface. However, in our measurements, we have also measured ARPES spectra with cooling from the highest temperature (180 K for x=0,2 and 200 K for x=0.4) to the lowest temperature (10 K for x=0.2 and 8 K for x=0.4) after heating, and similar spectra were obtained at the lowest temperature. This reproducibility would prove that the temperature evolution of the observed spectra is intrinsic.

For more detailed analysis, we have plotted the momentum distribution curve (MDCs) and EDCs at different temperatures in Figs. 6.2 and 6.3. As has been pointed out above, for x=0.2, an MDC-peak shift with temperature can be recognized (Fig. 6.2 (b)). In Fig. 6.2 (c), a small shoulder structure around -10 meV arising from the electron band near E_F was observed at 10 K, and it is attenuated at high temperatures due to the temperature broadening. For x=0.4, though MDC and EDC peaks can be recognized in the low temperature region, both intensities were too weak to discuss about the peak positions above 100 K. Their trends are similar to each other. Namely, as temperature increases, the peak structure is attenuated. EDCs that have been symmetrized in order to eliminate the temperature broadening are also shown in Figs. 6.2 (d) and 6.3 (d). For quantitative comparison of the density of states (DOS) near E_F, we have plotted intensity near E_F obtained by integrating symmetrized EDC within the energy range of $E_F \pm 10$ meV as a function of temperature in Figs. 6.2 (f) and 6.3 (f). They have been normalized to the intensity at the lowest temperature (10 K for x=0.2 and 8 K for x=0.4). In the case of the Se-underdoped sample, the intensity near the Fermi level is nearly

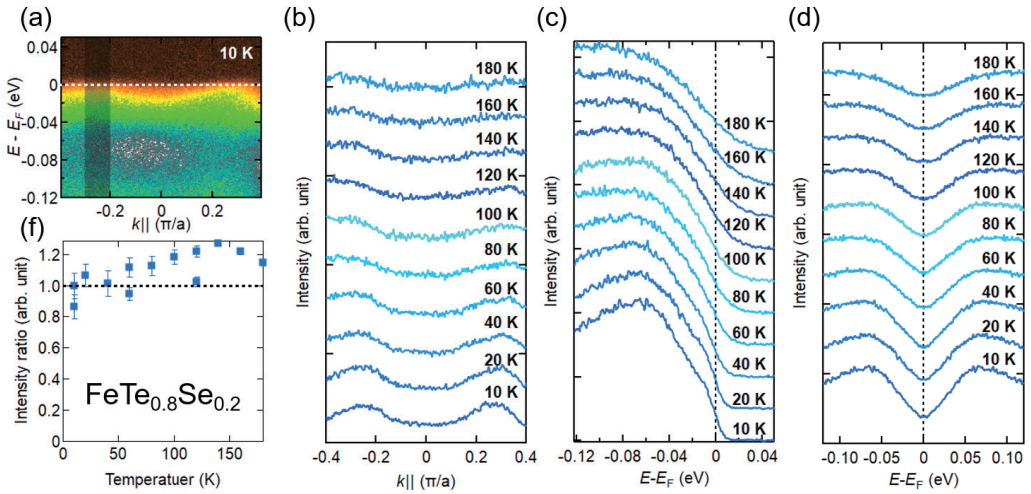

Figure 6.2: Temperature evolution of the spectra of the electron band in Te-annealed $FeTe_{0.8}Se_{0.2}$. (a) ARPES spectra at 10 K. (b) Temperature evolution of the momentum distribution curve (MDC) integrated within $E_F \pm 10$ meV from 10 K up to 180 K. (c) Temperature evolution of the energy distribution curve (EDC) obtained by integrating MDCs within momentum region of $k_F \pm 0.05\pi/a$ indicated by shaded section in (a). (d) Symmetrized EDCs shown in (c) with respects to E_F. (f) Temperature dependence of spectral weight around E_F. The intensity has been obtained by integrating the symmetrized EDCs within the energy range of $E_F \pm 10$ meV, and normalized to that at the lowest temperature (10 K).

constant or grows slightly with heating, indicating the insensitivity of the DOS near E_F to temperature. On the other hand, the intensity near E_F of the optimally-doped x=0.4 sample depends on temperature in a characteristic way (Fig. 6.3 (f)). The intensity decreases with increasing temperature in the temperature region below 100 K although it is independent of temperature above l30 K, which suggests that the DOS of the electron band around the zone corner decreases with increasing temperature, indicating the suppression of the coherent peak of the electron band and the disappearance of the electron pocket, in contrast to Se-underdoped compound. Therefore, we consider that spectral wight is transferred from the coherent states to an incoherent states with increasing temperature, similar to the case of the d_{xy} band around Γ [96]. According to the magneto-transport measurements, Hall coefficient of the optimally-doped compound also depends on temperature only blow $\sim$150 K and increases with heating within the temperature region below $\sim$ 75 K, similar to the temperature dependence of the coherent peak of the electron band in the optimally doped compound.

For the explanation of the relationship between the Hall coefficient and the

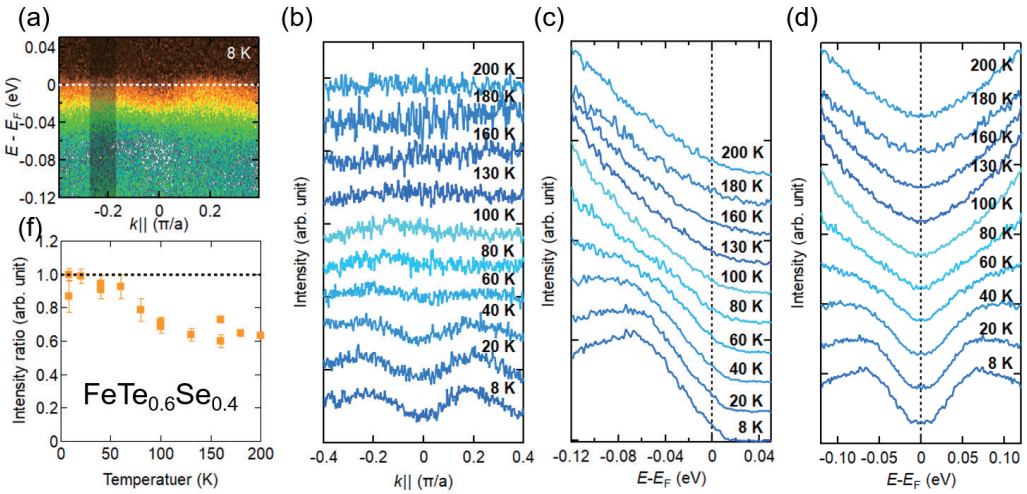

Figure 6.3: Temperature evolution of the spectra of the electron band in Te-annealed optimally doped $FeTe_{0.6}Se_{0.4}$. (a) ARPES spectra at 8 K. (b) Temperature evolution of the momentum distribution curve (MDC) integrated within $E_F \pm 10$ meV from 8 K up to 200 K. (c) Temperature evolution of the energy distribution curve (EDC) obtained by integrating MDCs within momentum region of $k_F \pm 0.05\pi/a$ indicated by shaded section in (a). (d) Symmetrized EDCs shown in (c) with respects to E_F. (f) Temperature dependence of spectral weight around E_F. The intensity ratio has been obtained by integrating the symmetrized EDCs within the energy range of $E_F \pm 10$ meV, and normalized to that at the lowest temperature (8 K).

electronic states, we have depicted a schematic picture for the Fermi surfaces predicted by present results in Fig. 6.4. In the low Se-doped compound, the electron band does not exhibit drastic changes within the temperature range below 200 K except the slight k_F shift. If the hole surfaces also do not change, the Fermi surfaces should not change. In that case, one cannot attribute the temperature dependence of the Hall coefficient to the evolution of the Fermi surface. One possibility is that antiferromagnetic fluctuation corresponding to the antiferromagnetic order observed in the parent compound FeTe affects charge carriers in compounds close to the parent compound. In the case of cuprates [97], it has been suggested theoretically that antiferromagnetic fluctuation can give rise non-trivial temperature dependence of the Hall coefficient, which differs from the prediction from the Fermi surface topology. On the other hand, for the optimally-doped compound, we could not observed the electron band at high temperatures, indicating the disappearance of the electron pocket. Assuming that the hole bands in the Te-annealed sample exhibit the temperature dependence similar to as-grown samples [96], the optimally doped compound would have only a small hole pocket centered at Γ. Taking into account the charge

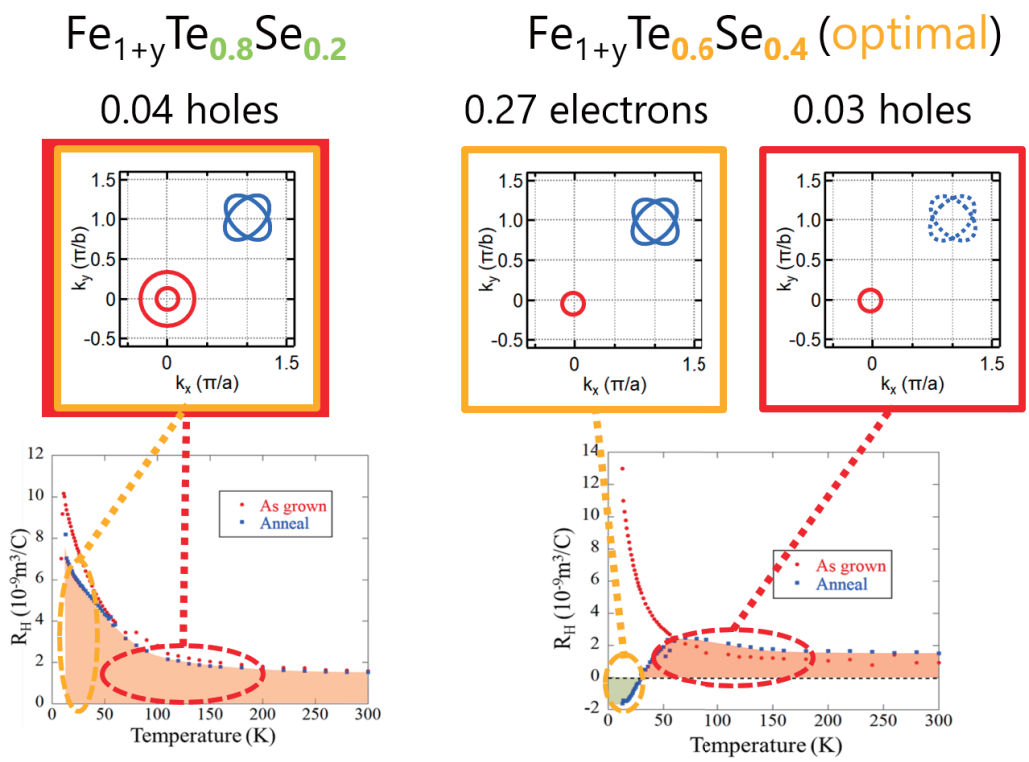

Figure 6.4: Schematic picture of the temperature evolution of the Fermi surface in Te-annealed $FeTe_{1-x}Se_x$.

carrier concentration estimated from the enclosed area of the Fermi surface at low temperature, the charge carrier concentration is 0.03 holes/unit cell in x=0.4 in high temperature region, which is comparable to that of x=0.2. The similar carrier concentrations may cause similar magnitudes of Hall coefficient between them at high temperature. In order to completely clarify the temperature evolution of the electronic states of Te-annealed $FeTe_{1-x}Se_x$, the hole bands at high temperatures remain to be studied systematically.

6.4 Summary

In conclusion, in order to clarify the temperature evolution of the band structure and the relation ship between the Hall coefficient and the electronic structure, in $FeTe_{1-x}Se_x$ in which the excess Fe-atoms are completely removed, we have carried out ARPES measurements of Te-annealed $FeTe_{1-x}Se_x$ (x=0.2 and 0.4). Upon increasing temperature, the coherent peak of the electron band around the zone corner weakens and disappears above 100 K in the optimally-doped compound in contrast

to the temperature independent behavior of it for Se-underdoped compound, indicating the disappearance of the electron pockets. Moreover, the possible changes of the Fermi surface topology predicted from present results can explain the temperature dependence of the Hall coefficient. However, since we have clarified only the temperature dependence of the electron band and the hole bands at high temperature is still uncertain, further work is necessary in order to completely clarify the temperature evolution of the electronic states in Te-annealed $FeTe_{1-x}Se_x$.

Chapter 7

Summary and conclusion

The "122"- and "11"-type iron-based superconductors (FeSCs) are one of the most extensively studied unconventional superconductors. Commonly, non-trivial phenomena have been observed in both cases although their details are different form each other. Investigation of the origin of the non-trivial phenomena have been considered to be a key to understand the mechanism of the unconventional superconductivity in the iron pnictides and iron chalcogenides. We have performed photoemission spectroscopy measurements and investigated the electronic structure of the "122"-type Cr-doped BaaFe$_2$As$_2$ and the Te-annealed "11"-type superconductor FeTe$_{1-x}$S$_x$.

In chapter 3, We have performed resonant photoemission spectroscopy (RPES) and x-ray absorption spectroscopy (XAS) measurements of Ba(Fe$_{0.81}$Cr$_{0.19}$)$_2$As$_2$ in order to study the electronic structure of Cr and Fe in Ba(Fe$_{0.81}$Cr$_{0.19}$)$_2$As$_2$.In both the cases, very smooth XAS spectra have been observed, indicating that the Fe and Cr 3*d* electrons are itinerant. For RPES measurements, the Fermi edge has been observed in the Cr 3*d* PDOS and the Cr 3*d* electrons has itinerant features. Therefore, Ba(Fe$_{0.81}$Cr$_{0.19}$)$_2$As$_2$ is consider to be an effectively hole-doped system in contrast to the case of Mn RPES in which the Fermi edge has not been observed. However, the Cr 3*d* PDOS is mainly located at $\sim$1 eV below E_F indicating the localization of the Cr 3*d* electrons. Then the high-spin state at the Cr site is realized by the on-site Coulomb interaction and Hund's coupling. Similar to the Mn substitution, this high spin state would favor the G-type antiferromagnetism and be detrimental to the superconductivity.

In chapter 4, we have conducted angle-resolved photoemission spectroscopy (ARPES) measurements of Ba(Fe$_{1-x}$Cr$_x$)$_2$As$_2$ with the valid Cr concentration (x= 0.06, 0.09, and x=0.19) in order to investigate the nature of the electronic structure and clarify the mechanism of the sign change of the in-plane resistivity anisotropy. Upon Cr substitution, Fermi level moves downward exhibiting upward band dispersion shift without significant changes of dispersion, indicating sufficient hole

doping with the Cr substitution in contrast to the absence of carrier doping in $Ba(Fe_{1-x}Mn_x)_2As_2$. Moreover, the Fermi surface topology changes from that of the parent compound. The elliptical electron pockets considered to dominate the scattering shrink and vanish eventually. The Dirac-cone-like electron pockets becomes hole pockets and expand with Cr contents, consistent with theoretical prediction. We concluded that the changes of the Fermi surface topology play a important role in the sign reversal of the in-plane resistivity anisotropy.

In chapter 5, we have carried out ARPES measurements of Te-annealed $FeTe_{1-x}Se_x$ (x=0.15, 0.2, 0.3 and 0.4) in order to investigate the nature of the electronic structure of $FeTe_{1-x}Se_x$ excess Fe ions are completely removed compound and clarify the Se-concentration evolution of the band structure. Upon increasing Se content, the γ band shifts downward and induces disappearance of the outer large hole pockets around the Γ point. In addition, the shallow electron band becomes to deeper, indicating the weakening of the band renormalization factor. These change in Fermi surface topology and band dispersion can explain the sign reversal of the Hall coefficient between Se-underdoped and optimally-doped compounds. Therefore, we concluded that the changes of the Fermi topology and mass renormalization play a important role in the sign reversal of the Hall coefficient.

In chapter 6, we have performed temperature dependent ARPES measurements of Te-annealed $FeTe_{1-x}Se_x$ (x=0.2 and 0.4) in order to clarify the temperature evolution of the band structure and the relation ship between the Hall coefficient and the electronic structure, in $FeTe_{1-x}Se_x$ in which the excess Fe-atoms are completely removed. Upon increasing temperature, the coherent peak of the electron band around the zone corner weakens and disappears above 100 K in the optimally-doped compound in contrast to the temperature independent behavior of it for Se-underdoped compound, indicating the disappearance of the electron pockets. Moreover, the possible changes of the Fermi surface topology predicted from present results can explain the temperature dependence of the Hall coefficient. However, since we have clarified only the temperature dependence of the electron band and the hole bands at high temperature is still uncertain, further work is necessary in order to completely clarify the temperature evolution of the electronic states in Te-annealed $FeTe_{1-x}Se_x$.

Acknowledgments

It is my great pleasure to show my greatest appreciation to the following people.

First of all, I would like to express my deepest gratitude to my supervisor Prof. Atsushi Fujimori, who has guided me to the exciting and fruitful research project. I greatly appreciate his kind guidance, valuable advice, fruitful discussions, and continuous encouragement throughout this study.

I would also like to express my deep gratitude to Dr. Goro Shibata, who has taught me with great patience, from the principles to the experimental setup of angle-photoemission photoemission spectroscopy experiments.

Thanks are due to Prof. Setsuko Tajima, Assoc. prof. Shigeki Miyasaka and Dr. Tatsuya Kobayashi for supplying me with the high-quality single crystals of $Ba(Fe_{1-x}Cr_x)_2As_2$ and for useful advice and discussion. I would also like to express my great thanks to Prof. Takao Watanabe and Mr. Takumi Ootsuka for supplying me with the high-quality single crystals of $FeTe_{1-x}Se_x$.

I would also like to thank collaborators at UVSOR: Prof. Kiyohisa Tanaka and Dr. Shinichiro Ideta for their experimental support at Beamline 7U at UVSOR. I would like to acknowledge Prof. Kanta Ono, Prof. Hiroshi Kumigashira, Dr. Nobuhito Inami, Prof. Koji Horiba, Prof. Masaki Kobayashi, and Dr. Makoto Minohara for their experimental support at BL-28A and BL-2A of Photon Factory. I would also like to thank Prof. Z. X. Shen, Dr. Makoto Hashimoto, and Dr. Donhui Lu for their experimental support at BL 5-4 of SSRL.

I would also like to thank all the members of Fujimori group: Mr. Yosuke Nonaka, Mr. Masahiro Suzuki, Mr. Wan Yuxuan and Mr Takahito Takeda. I would also like to thank previous member, Dr. Shoya Sakamoto, Mr. Keisuke Ikeda, Mr. Chi Zandong, Mr. Lin Chun, Mr. Suguru Nakata and Mr Kenta Hagiwara. I would like to express my special gratitude to Dr. Hakuto Suzuki, Dr. Jian Xu, and Dr. Masafumi Horio for teaching me the principles of photoemission spectroscopy and how to analyze the ARPES spectra. I would like to thank Ms. Yuko Shimazaki, Ms. Ami Ito and Ms. Mayuko Niwata for dealing with a lot of business stuff and giving me encouragement.

Finally, I would like to thank my parents and relatives for supporting my stu-

dent life and research activities.

December 2018
Keisuke Koshiishi

References

[1] Y. Kamihara, T. Watanabe, M. Hirano, and H. Hosono, J. Am. Chem. Soc. **130**, 3296 (2008).

[2] J. Paglione and R. Greene, Nat. Phys. **6**, 645 (2010).

[3] M. Rotter, M. Tegel, and D. Johrendt, Phys. Rev. B **78**, 020503 (2008).

[4] A. Rahman and A. Hossen, Am. Sci. Res. J. Eng. Technol. Sci. **11**, 104 (2015).

[5] X. Zhu, F. Han, G. Mu, P. Cheng, B. Shen, B. Zeng, and H.-H. Wen, Phys. Rev. B **79**, 220512 (2009).

[6] F.-C. Hsu, J.-Y. Luo, K.-W. Yeh, T.-K. Chen, T.-W. Huang, P. M. Wu, Y.-C. Lee, Y.-L. Huang, Y.-Y. Chu, D.-C. Yan, and M.-K. Wu, Proc. Natl. Acad. Sci. U. S. A. **105**, 14262 (2008).

[7] F. Ye, S. Chi, W. Bao, X. F. Wang, J. J. Ying, X. H. Chen, H. D. Wang, C. H. Dong, and M. Fang, Phys. Rev. Lett. **107**, 137003 (2011).

[8] H. Ghosh and S. Sen, arXiv 1408.3244 (2014).

[9] F. Steglich, J. Aarts, C. D. Bredl, W. Lieke, D. Meschede, W. Franz, and H. Schäfer, Phys. Rev. Lett. **437**, 1892 (1979).

[10] P. Shirage, K. Miyazawa, M. Ishikado, K. Kihou, C. Lee, N. Takeshita, H. Matsuhata, R. Kumai, Y. Tomioka, T. Ito, H. Kito, H. Eisaki, S. Shamoto, and a. Iyo, Phys. C Supercond. **469**, 355 (2009).

[11] Q. Huang, Y. Qiu, W. Bao, M. a. Green, J. W. Lynn, Y. C. Gasparovic, T. Wu, G. Wu, and X. H. Chen, Phys. Rev. Lett. **101**, 257003 (2008).

[12] K. A. Filsinger, W. Schnelle, P. Adler, G. H. Fecher, M. Reehuis, A. Hoser, J.-U. Hoffmann, P. Werner, M. Greenblatt, and C. Felser, Phys. Rev. B **95**, 184414 (2017).

[13] A. E. Bohmer, F. Hardy, F. Eilers, D. Ernst, P. Adelmann, P. Schweiss, T. Wolf, and C. Meingast, Phys. Rev. B - Condens. Matter Mater. Phys. **87**, 1 (2013).

[14] W. Bao, Y. Qiu, Q. Huang, M. A. Green, P. Zajdel, M. R. Fitzsimmons, M. Zhernenkov, S. Chang, M. Fang, B. Qian, E. K. Vehstedt, J. Yang, H. M. Pham, L. Spinu, and Z. Q. Mao, Phys. Rev. Lett. **102**, 247001 (2009).

[15] S. Li, C. de la Cruz, Q. Huang, Y. Chen, J. W. Lynn, J. Hu, Y.-l. Huang, F.-c. Hsu, K.-w. Yeh, M.-k. Wu, and P. Dai, Phys. Rev. B **79**, 054503 (2009).

[16] A. Jesche, N. Caroca-Canales, H. Rosner, H. Borrmann, A. Ormeci, D. Kasinathan, H. H. Klauss, H. Luetkens, R. Khasanov, A. Amato, A. Hoser, K. Kaneko, C. Krellner, and C. Geibel, Phys. Rev. B **78**, 180504 (2008).

[17] a. Martinelli, a. Palenzona, M. Tropeano, C. Ferdeghini, M. Putti, M. R. Cimberle, T. D. Nguyen, M. Affronte, and C. Ritter, Phys. Rev. B **81**, 1 (2010).

[18] A. S. Sefat, D. Singh, and L. VanBebber, Phys. Rev. B **79**, 224524 (2009).

[19] H. Luetkens, H.-H. Klauss, M. Kraken, F. J. Litterst, T. Dellmann, R. Klingeler, C. Hess, R. Khasanov, A. Amato, C. Baines, M. Kosmala, O. J. Schumann, M. Braden, J. Hamann-Borrero, N. Leps, A. Kondrat, G. Behr, J. Werner, and B. Büchner, Nat. Mater. **8**, 305 (2009).

[20] C. R. Rotundu, D. T. Keane, B. Freelon, S. D. Wilson, A. Kim, P. N. Valdivia, E. Bourret-Courchesne, and R. J. Birgeneau, Phys. Rev. B **80**, 144517 (2009).

[21] J. Zhao, Q. Huang, C. de la Cruz, S. Li, J. W. Lynn, Y. Chen, M. A. Green, G. F. Chen, G. Li, Z. Li, J. L. Luo, N. L. Wang, and P. Dai, Nat. Mater. **7**, 953 (2008).

[22] S. Ishida, M. Nakajima, T. Liang, K. Kihou, C. H. Lee, a. Iyo, H. Eisaki, T. Kakeshita, Y. Tomioka, T. Ito, and S. Uchida, Phys. Rev. Lett. **110**, 207001 (2013).

[23] F. Rullier-Albenque, D. Colson, a. Forget, P. Thuéry, and S. Poissonnet, Phys. Rev. B **81**, 224503 (2010).

[24] S. Nandi, M. Kim, A. Kreyssig, and R. Fernandes, Phys. Rev. Lett. **104**, 057006 (2010).

[25] N. Katayama, S. Ji, D. Louca, S. Lee, M. Fujita, T. J. Sato, J. Wen, Z. Xu, G. Gu, G. Xu, Z. Lin, M. Enoki, S. Chang, K. Yamada, and J. M. Tranquada, J. Phys. Soc. Jpn. **79**, 1 (2010).

[26] A. N. Lavrov, H. J. Kang, Y. Kurita, T. Suzuki, S. Komiya, J. W. Lynn, S.-H. Lee, P. Dai, and Y. Ando, Phys. Rev. Lett. **92**, 227003 (2004).

[27] D. J. Singh, Phys. Rev. B **78**, 094511 (2008).

[28] M. Yi, D. Lu, and J. Chu, Proc. Natl. Acad. Sci. U. S. A. **108**, 6878 (2011).

[29] L. Liu, T. Mikami, S. Ishida, K. Koshiishi, K. Okazaki, T. Yoshida, H. Suzuki, M. Horio, L. C. C. Ambolode, J. Xu, H. Kumigashira, K. Ono, M. Nakajima, K. Kihou, C. H. Lee, A. Iyo, H. Eisaki, T. Kakeshita, S. Uchida, and A. Fujimori, Phys. Rev. B **92**, 094503 (2015).

[30] T. Terashima, N. Kurita, M. Tomita, K. Kihou, C.-H. Lee, Y. Tomioka, T. Ito, A. Iyo, H. Eisaki, T. Liang, M. Nakajima, S. Ishida, S.-i. Uchida, H. Harima, and S. Uji, Phys. Rev. Lett. **107**, 176402 (2011).

[31] M. Yi, D. Lu, J. Analytis, J.-H. Chu, and S.-K. Mo, Phys. Rev. B **80**, 174510 (2009).

[32] A. Subedi, L. Zhang, D. J. Singh, and M. H. Du, Phys. Rev. B **78**, 134514 (2008).

[33] D. C. Johnston, Adv. Phys. **59**, 803 (2010).

[34] T. Qian, X.-P. Wang, W.-C. Jin, P. Zhang, P. Richard, G. Xu, X. Dai, Z. Fang, J.-G. Guo, X.-L. Chen, and H. Ding, Phys. Rev. Lett. **106**, 187001 (2011).

[35] X. Liu *et al.*, Nat. Commun. **5**, 5047 (2014).

[36] L. Zhao *et al.*, Nat. Commun. **7**, 10608 (2016).

[37] J. Chu, J. Analytis, K. D. Greve, and P. McMahon, Science (80-.). **329**, 824 (2010).

[38] E. C. Blomberg, M. a. Tanatar, R. M. Fernandes, I. I. Mazin, B. Shen, H.-H. Wen, M. D. Johannes, J. Schmalian, and R. Prozorov, Nat. Commun. **4**, 1914 (2013).

[39] K. Sugimoto, P. Prelovsek, E. Kaneshita, and T. Tohyama, Phys. Rev. B **90**, 3 (2014).

[40] B. Valenzuela, E. Bascones, and M. J. Calderón, Phys. Rev. Lett. **105**, 207202 (2010).

[41] E. C. Blomberg, M. A. Tanatar, R. M. Fernandes, I. I. Mazin, B. Shen, H.-h. Wen, M. D. Johannes, J. Schmalian, and R. Prozorov, Nat. Commun. **4**, 1914 (2013).

[42] K. Sugimoto, E. Kaneshita, and T. Tohyama, Phys. C Supercond. **471**, 666 (2011).

[43] A. Thaler, H. Hodovanets, M. S. Torikachvili, S. Ran, A. Kracher, W. Straszheim, J. Q. Yan, E. Mun, and P. C. Canfield, Phys. Rev. B **84**, 144528 (2011).

[44] K. Marty, A. D. Christianson, C. H. Wang, M. Matsuda, H. Cao, L. H. VanBebber, J. L. Zarestky, D. J. Singh, A. S. Sefat, and M. D. Lumsden, Phys. Rev. B **83**, 060509 (2011).

[45] M. G. Kim, A. Kreyssig, A. Thaler, D. K. Pratt, W. Tian, J. L. Zarestky, M. A. Green, S. L. Bud'ko, P. C. Canfield, R. J. McQueeney, and A. I. Goldman, Phys. Rev. B **82**, 220503 (2010).

[46] K. Ohgushi and Y. Kiuchi, Phys. Rev. B **85**, 064522 (2012).

[47] T. Kobayashi, K. Tanaka, S. Miyasaka, and S. Tajima, J. Phys. Soc. Jpn. **84**, 094707 (2015).

[48] A. S. Sefat, R. Jin, M. A. McGuire, B. C. Sales, D. J. Singh, and D. Mandrus, Phys. Rev. Lett. **101**, 117004 (2008).

[49] N. Ni, A. Thaler, J. Yan, and A. Kracher, Phys. Rev. B **82**, 024519 (2010).

[50] M. Rotter, M. Tegel, and D. Johrendt, Phys. Rev. Lett. **101**, 107006 (2008).

[51] Y. Sun, T. Yamada, S. Pyon, and T. Tamegai, Sci. Rep. **6**, 32290 (2016).

[52] Y. Koshika, T. Usui, S. Adachi, T. Watanabe, K. Sakano, S. Simayi, and M. Yoshizawa, J. Phys. Soc. Jpn. **82**, 023703 (2013).

[53] T. Otsuka, S. Hagisawa, S. Adachi, T. Usui, T. Watanabe, Y. Nakanishi, M. Yoshizawa, and S. Kimura, , JPS autumn meeting, (2016).

[54] M. Imaizumi, T. Noji, T. Adachi, and Y. Koike, **471**, 614 (2011).

[55] Y. Sun, T. Taen, T. Yamada, S. Pyon, T. Nishizaki, Z. Shi, and T. Tamegai, Phys. Rev. B **89**, 144512 (2014).

[56] Y. Sun, Y. Tsuchiya, T. Taen, T. Yamada, S. Pyon, A. Sugimoto, T. Ekino, Z. Shi, and T. Tamegai, Sci. Rep. **4**, 4585 (2015).

[57] Y. Sun, T. Taen, T. Yamada, Y. Tsuchiya, S. Pyon, and T. Tamegai, Supercond. Sci. Technol. **28**, 044002 (2015).

[58] Y. Zhang, C. He, Z. R. Ye, J. Jiang, F. Chen, M. Xu, Q. Q. Ge, B. P. Xie, J. Wei, M. Aeschlimann, X. Y. Cui, M. Shi, J. P. Hu, and D. L. Feng, Phys. Rev. B **85**, 085121 (2012).

[59] H. Suzuki, T. Yoshida, S. Ideta, G. Shibata, K. Ishigami, T. Kadono, a. Fujimori, M. Hashimoto, D. H. Lu, Z.-X. Shen, K. Ono, E. Sakai, H. Kumigashira, M. Matsuo, and T. Sasagawa, Phys. Rev. B **88**, 100501 (2013).

[60] P. Richard, A. van Roekeghem, B. Q. Lv, T. Qian, T. K. Kim, M. Hoesch, J.-P. Hu, A. S. Sefat, S. Biermann, and H. Ding, Phys. Rev. B **95**, 184516 (2017).

[61] J. Nayak, K. Filsinger, G. H. Fecher, S. Chadov, J. Minár, E. D. L. Rienks, B. Büchner, S. P. Parkin, J. Fink, and C. Felser, Proc. Natl. Acad. Sci. **114**, 201702234 (2017).

[62] M. Nakajima, S. Ishida, K. Kihou, Y. Tomioka, T. Ito, Y. Yoshida, C. H. Lee, H. Kito, A. Iyo, H. Eisaki, K. M. Kojima, and S. Uchida, Phys. Rev. B **81**, 104528 (2010).

[63] K. D. Kwon, K. Refson, S. Bone, R. Qiao, W.-l. Yang, Z. Liu, and G. Sposito, Phys. Rev. B **83**, 064402 (2011).

[64] G. Levy, R. Sutarto, D. Chevrier, T. Regier, R. Blyth, J. Geck, S. Wurmehl, L. Harnagea, H. Wadati, T. Mizokawa, I. S. Elfimov, A. Damascelli, and G. a. Sawatzky, Phys. Rev. Lett. **109**, 077001 (2012).

[65] M. A. Tomaz, W. J. Antel, W. L. O'Brien, and G. R. Harp, Phys. Rev. B **55**, 3716 (1997).

[66] C. Theil, J. van Elp, and F. Folkmann, Phys. Rev. B **59**, 7931 (1999).

[67] M. Kobayashi, Y. Ishida, J. I. Hwang, G. S. Song, A. Fujimori, C. S. Yang, L. Lee, H.-J. Lin, D. J. Huang, C. T. Chen, Y. Takeda, K. Terai, S.-I. Fujimori, T. Okane, Y. Saitoh, H. Yamagami, K. Kobayashi, A. Tanaka, H. Saito, and K. Ando, New J. Phys. **10**, 055011 (2008).

[68] U. Fano, Phys. Rev. **124**, 1866 (1961).

[69] H. Suzuki, T. Yoshida, S. Ideta, G. Shibata, and K. Ishigami, 1 (2013).

[70] W. Malaeb, T. Yoshida, T. Kataoka, A. Fujimori, M. Kubota, K. Ono, H. Usui, K. Kuroki, R. Arita, H. Aoki, Y. Kamihara, M. Hirano, and H. Hosono, J. Phys. Soc. Jpn. **77**, 093714 (2008).

[71] V. I. Anisimov, D. M. Korotin, M. A. Korotin, A. V. Kozhevnikov, J. Kuneš, A. O. Shorikov, S. L. Skornyakov, and S. V. Streltsov, J. Phys. Condens. Matter **21**, 075602 (2009).

[72] T. Miyake, K. Nakamura, R. Arita, and M. Imada, J. Phys. Soc. Jpn. **79**, 044705 (2010).

[73] S. Kasahara, T. Shibauchi, K. Hashimoto, K. Ikada, S. Tonegawa, R. Okazaki, H. Shishido, H. Ikeda, H. Takeya, K. Hirata, T. Terashima, and Y. Matsuda, Phys. Rev. B **81**, 184519 (2010).

[74] T. Urata, Y. Tanabe, K. K. Huynh, H. Oguro, K. Watanabe, S. Heguri, and K. Tanigaki, **024503**, 1 (2013).

[75] I. R. Fisher, L. Degiorgi, and Z. X. Shen, Reports Prog. Phys. **74**, 124506 (2011).

[76] S. Ishida, T. Liang, M. Nakajima, K. Kihou, and C. Lee, Phys. Rev. B **84**, 184514 (2011).

[77] S. Ishida, M. Nakajima, T. Liang, K. Kihou, C.-H. Lee, A. Iyo, H. Eisaki, T. Kakeshita, Y. Tomioka, T. Ito, and S.-i. Uchida, J. Am. Chem. Soc. **135**, 3158 (2013).

[78] J. J. Ying, X. F. Wang, T. Wu, Z. J. Xiang, R. H. Liu, Y. J. Yan, a. F. Wang, M. Zhang, G. J. Ye, P. Cheng, J. P. Hu, and X. H. Chen, Phys. Rev. Lett. **107**, 1 (2011).

[79] Z. K. Liu, M. Yi, Y. Zhang, J. Hu, R. Yu, J.-X. Zhu, R.-H. He, Y. L. Chen, M. Hashimoto, R. G. Moore, S.-K. Mo, Z. Hussain, Q. Si, Z. Q. Mao, D. H. Lu, and Z.-X. Shen, Phys. Rev. B **92**, 235138 (2015).

[80] T. Yoshida, I. Nishi, S. Ideta, a. Fujimori, M. Kubota, K. Ono, S. Kasahara, T. Shibauchi, T. Terashima, Y. Matsuda, H. Ikeda, and R. Arita, Phys. Rev. Lett. **106**, 117001 (2011).

[81] R. P. Vasquez, J. Electron Spectros. Relat. Phenomena **56**, 217 (1991).

[82] T. Terashima, N. Kurita, M. Kimata, M. Tomita, S. Tsuchiya, M. Imai, A. Sato, K. Kihou, C.-H. Lee, H. Kito, H. Eisaki, A. Iyo, T. Saito, H. Fukazawa, Y. Kohori, H. Harima, and S. Uji, Phys. Rev. B **87**, 224512 (2013).

[83] T. Morinari, E. Kaneshita, and T. Tohyama, Phys. Rev. Lett. **105**, 1 (2010).

[84] S. Li, C. de la Cruz, Q. Huang, G. F. Chen, T.-L. Xia, J. L. Luo, N. L. Wang, and P. Dai, Phys. Rev. B **80**, 020504 (2009).

[85] M. H. Fang, H. M. Pham, B. Qian, T. J. Liu, E. K. Vehstedt, Y. Liu, L. Spinu, and Z. Q. Mao, Phys. Rev. B **78**, 224503 (2008).

[86] B. C. Sales, A. S. Sefat, M. A. Mcguire, R. Y. Jin, D. Mandrus, and Y. Mozharivskyj, 1 (2009).

[87] C. Dong, H. Wang, Z. Li, J. Chen, H. Q. Yuan, and M. Fang, Phys. Rev. B **84**, 224506 (2011).

[88] Y. Sun, T. Taen, Y. Tsuchiya, Z. X. Shi, and T. Tamegai, Supercond. Sci. Technol. **26**, 015015 (2013).

[89] F. Chen, B. Zhou, Y. Zhang, J. Wei, H.-w. Ou, J.-f. Zhao, C. He, Q.-q. Ge, M. Arita, K. Shimada, H. Namatame, M. Taniguchi, Z.-y. Lu, J. Hu, X.-y. Cui, and D. L. Feng, Phys. Rev. B **81**, 014526 (2010).

[90] E. Ieki, K. Nakayama, Y. Miyata, T. Sato, H. Miao, N. Xu, X.-P. Wang, P. Zhang, T. Qian, P. Richard, Z.-J. Xu, J. S. Wen, G. D. Gu, H. Q. Luo, H.-H. Wen, H. Ding, and T. Takahashi, Phys. Rev. B **89**, 140506 (2014).

[91] L. C. C. Ambolode, K. Okazaki, M. Horio, H. Suzuki, L. Liu, S. Ideta, T. Yoshida, T. Mikami, T. Kakeshita, S. Uchida, K. Ono, H. Kumigashira, M. Hashimoto, D.-H. Lu, Z.-X. Shen, and A. Fujimori, Phys. Rev. B **92**, 035104 (2015).

[92] J. M. Luttinger, Phys. Rev. **119**, 1153 (1960).

[93] I. Tsukada, M. Hanawa, S. Komiya, T. Akiike, R. Tanaka, Y. Imai, and A. Maeda, 3 (2010).

[94] H. Lin, Y. Li, Q. Deng, J. Xing, J. Liu, X. Zhu, H. Yang, and H.-h. Wen, Phys. Rev. B **93**, 144505 (2016).

[95] P. Zhang, K. Yaji, T. Hashimoto, Y. Ota, T. Kondo, K. Okazaki, Z. Wang, J. Wen, G. D. Gu, H. Ding, and S. Shin, Science (80-.). **360**, 182 (2018).

[96] M. Yi *et al.*, Nat. Commun. **6**, 7777 (2015).

[97] H. Kontani, Reports Prog. Phys. **71**, 026501 (2008).